Faculty of Engineering (Electronic)

Faculty of Applied Engineering

Sub-sampled Exponential Analysis in Antenna Applications

Dissertation presented for the degrees of
Doctor of Philosophy (PhD) in Electronic Engineering at Stellenbosch University
and Doctor of Applied Engineering (PhD) at the University of Antwerp
to be defended by

Rina-Mari Weideman

Supervisors
Prof. dr. Dirk de Villiers
Prof. dr. Annie Cuyt
Prof. dr. Stijn Derammelaere

January, 2024

Acknowledgments

I would like to express my gratitude and thanks to the following people and organisations, who all helped to make my doctoral journey more achievable:

- The National Research Foundation (NRF) for funding my studies at Stellenbosch University, and the EXPOWER project for funding my visits to the University of Antwerp.
- My supervisors, Dirk de Villiers and Annie Cuyt, for their invaluable guidance and support throughout this project. I am grateful for the privilege of having two competent leaders whose commitment to research and passion for their work have been a continuous inspiration. I am also especially appreciative of the opportunity to pursue a joint PhD.
- My colleague and friend, Ridalise Raal, for accompanying me throughout this journey from beginning to end. Thank you for your academic guidance, emotional support, and for navigating the logistics of a joint PhD ahead of me, which greatly eased my path.
- My colleagues and co-authors, Ferre Knaepkens, Wen-Shin Lee, and Stefan Wijnholds, for their productive and positive collaboration that significantly contributed to my research.
- My family and friends, with special thanks to my parents, André and Mari, and brothers, Hendrik and Nicolaas, for their unwavering support. Each prayer, word of encouragement, and practical advice has significantly driven me closer to this achievement.

January 2024

Contents

Summary

The use of sub-sampled exponential analysis in antenna applications is appealing for multiple reasons. The computational time of simulations using sparse as opposed to dense sampling is significantly lower, and in the case of spatial sampling, sparse samples lead to an increased resolution. In this dissertation, we investigate the use of a sub-sampled exponential analysis method called VEXPA in three different antenna applications.

The first application is the use of one-bit data in the sparse direction-of-estimation (DOA) estimation problem. Sparse arrays are desirable for the fact that they have less mutual coupling and an increased resolution compared to a dense array with the same number of antenna elements. The quantisation step of converting the incoming analogue signals to their digital equivalents introduces another layer of complexity to the traditional problem. In Part 1 of this dissertation, we show how VEXPA can be applied to the one-bit DOA estimation problem, adding the feature of estimating the number of incoming signals.

Part 2 discusses the application of antenna position estimation using VEXPA, which is essentially the inverse of the DOA estimation problem. In sparse irregular arrays, it is helpful to have the ability to obtain the precise element positions after the installation phase, since this requires less accuracy when placing the elements. By accurately estimating the antenna positions, the accidental case of an antenna cable connected to the wrong receiver can also be detected and flagged. The method makes use of harmonically related signals transmitted from an unmanned aerial vehicle (UAV) at a known position in the sky.

Finally, the application of the characterisation of frequency ripple in reflector systems is discussed in Part 3. In small reflector systems, a ripple across frequency appears in the radiation pattern due to the interference of sub reflector diffracted fields and main reflector reflected fields. This ripple translates to figures of merit such as the sensitivity, antenna noise temperature and aperture efficiency and it is therefore important to be characterised. It is both shown how the electric fields can be sub-sampled and subsequently reconstructed, as well as how the frequency components can be identified from a densely-sampled antenna noise temperature function.

Opsomming

Die gebruik van yl-gemonsterde eksponensiële analise in antennatoepassings is aantreklik vir verskeie redes. Die berekeningstyd van simulasies wat yl in teenstelling met digte monsterneming gebruik, is aansienlik laer, en in die geval van ruimtelike monsterneming, lei yl monsters tot 'n verhoogde resolusie. In hierdie proefskrif ondersoek ons die gebruik van 'n yl-gemonsterde eksponensiële analise metode genaamd VEXPA in drie verskillende antenna toepassings.

Die eerste toepassing is die gebruik van een-bis data in die yl rigting-afskatting probleem. Yl antennaskikkings is voordelig vir die feit dat hulle minder onderlinge koppeling en 'n verhoogde resolusie het in vergelyking met 'n digte skikking met dieselfde aantal antenna-elemente. Die kwantiseringstap, wat die inkomende analoogseine omskakel na hul digitale ekwivalente, stel nog 'n laag van kompleksiteit aan die tradisionele probleem bekend. In Deel 1 van hierdie proefskrif wys ons hoe VEXPA toegepas kan word op die een-bis rigting-afskatting probleem, en voeg die vermoë by om die aantal inkomende seine af te skat.

Deel 2 bespreek die toepassing van antenna posisie afskatting deur gebruik te maak van VEXPA, wat in wese die omgekeerde van die rigting-afskatting probleem is. In yl onreëlmatige skikkings is dit nuttig om die vermoë te hê om die presiese elementposisies nà die installasiefase te verkry, aangesien dit minder akkuraatheid vereis tydens die plasing van die elemente. Deur die antennaposisies akkuraat af te skat, kan die toevallige geval van 'n antennakabel wat aan die verkeerde ontvanger gekoppel is, ook opgespoor en gemerk word. Die metode maak gebruik van harmonies-verwante seine wat vanaf 'n onbemande lugvoertuig op 'n bekende posisie in die lug uitgesaai word.

Laastens word die toepassing van die karakterisering van frekwensie-rimpeling in reflektorstelsels in Deel 3 bespreek. In klein reflektorstelsels verskyn 'n rimpeling oor frekwensie in die stralingspatroon, as gevolg van die interferensie van diffraksie velde van die subreflektor en weerkaatsvelde van die hoofreflektor. Hierdie rimpeling vertaal na verdienstesyfers soos die sensitiwiteit, antenna ruistemperatuur en stralingsvlak benuttingsgraad, en dus is dit belangrik om gekarakteriseer te word. Dit word beide getoon hoe die elektriese velde yl-gemonster en daarna gerekonstrueer kan word, sowel as hoe die frekwensiekomponente geïdentifiseer kan word vanaf 'n dig-gemonsterde antenna ruistemperatuurfunksie.

Samenvatting

Het gebruik van onder-sampled exponentiële analyse in antennetoepassingen is om meerdere redenen aantrekkelijk. De rekentijd van simulaties die gebruik maken van ijle in tegenstelling tot dichte sampling is aanzienlijk lager, en in het geval van ruimtelijke sampling leiden ijle samples tot een hogere resolutie. In dit proefschrift onderzoeken we het gebruik van een onder-sampled exponentiële analysemethode genaamd VEXPA in drie verschillende antennetoepassingen.

De eerste toepassing is het gebruik van één-bits gegevens in het ijle schattingsprobleem van de richting van de schatting (DOA). Ijle arrays zijn wenselijk omdat ze minder onderlinge koppeling en een hogere resolutie hebben in vergelijking met een dichte array met hetzelfde aantal antenne-elementen. De kwantiseringsstap van het omzetten van de inkomende analoge signalen naar hun digitale equivalenten introduceert nog een extra complexiteit in het traditionele probleem. In deel 1 van dit proefschrift laten we zien hoe VEXPA kan worden toegepast op het één-bits DOA-schattingsprobleem, waaraan het schatten van het aantal inkomende signalen wordt toegevoegd.

Deel 2 bespreekt de toepassing van antennepositieschatting met VEXPA, wat in wezen de inverse is van het DOA-schattingsprobleem. In ijle onregelmatige arrays is het handig om de precieze elementposities te kunnen bepalen na de installatiefase, omdat dit minder nauwkeurigheid vereist dan bij het plaatsen van de elementen. Door de antennepositie nauwkeurig te schatten, kan ook het geval van een antennekabel die op de verkeerde ontvanger is aangesloten, worden gedetecteerd en gemarkeerd. De methode maakt gebruik van harmonisch gerelateerde signalen die worden uitgezonden door een onbemande drone (UAV) op een bekende positie in de lucht.

Tot slot wordt in deel 3 de toepassing van de karakterisering van frequentierimpeling in reflectorsystemen besproken. In kleine reflectorsystemen verschijnt een rimpel over de frequentie in het stralingspatroon door de interferentie van diffractievelden van de subreflector en gereflecteerde velden van de hoofdreflector. Deze rimpel vertaalt zich in kengetallen zoals de gevoeligheid, de antenneruistemperatuur en het diafragmarendement en is daarom belangrijk om gekarakteriseerd te worden. Er wordt zowel getoond hoe de elektrische velden kunnen worden gesubsampled en vervolgens gereconstrueerd, als hoe de frequentiecomponenten kunnen worden geïdentificeerd uit een dicht bemonsterde antenneruistemperatuurfunctie.

Introduction

Background and Motivation

Complex exponential signals make ample appearances in the field of antennas. In order to extract meaningful information from these signals, they are sampled at a specific sampling rate. Different reasons exist why a larger sampling step is preferred at which these signals are sampled. Sub-sampled exponential analysis refers to the process of acquiring information from data that have been sampled at a rate below the Nyquist sampling limit.

In this dissertation, we investigate different applications in antennas that use and benefit from sub-sampled exponential analysis. Specifically, the problems that are addressed are direction-of-arrival estimation (with a focus on quantised data), antenna position estimation and the characterisation of the ripple in the electric field functions of reflector antennas.

Radio Astronomy and the Square Kilometre Array

The applications presented in this dissertation all contribute to the field of radio astronomy. Radio telescopes are used to detect astronomical phenomena in the radio frequency range of the electromagnetic spectrum [1]. This can aid us in gaining knowledge on the early cosmos and the formation of stars and planets, as well as understanding the spread of hydrogen in the universe, which is the most abundant element.

In order to observe fine detail in the sky, a high angular resolution is required. By combining a number of antenna elements, referred to as an antenna array, a much larger aperture (and in turn increased resolution) than that of a single antenna can be achieved. Having a large number of antennas with a smaller diameter can provide a similar collecting area as a small number of antennas with a larger diameter. This big-N-small-D strategy is used in existing radio astronomy projects, such as the Square Kilometre Array (SKA).

The SKA is an international project that aims to build the world's largest radio telescope [2]. Its science goals include [3]:

- Studying the cosmic dawn and epoch of reionisation, the time period when stars, galaxies and black holes first formed and hydrogen's emissions changed from neutral to ionised. This is done through the observation of neutral hydrogen's weak radiation and therefore requires a telescope with a large collecting area.
- Testing Einstein's general theory of relativity in extreme conditions, such as the strong field environments around black holes. This is done by measuring changes to pulsars, the collapsed spinning cores of dead stars.
- Finding a better understanding of dark energy, which is the term given to the unknown force thought to cause the acceleration of the expansion of the universe.

The name of the SKA project refers to the fact that the total effective collecting area will be one square kilometre. This number was chosen by considering which collecting area would be independently required for each of the science goals. Currently, construction on the the first phase of the project, named SKA-1, is underway. The collecting area of the first stage will be a fraction of the total envisaged number. The project will consist of two sub-arrays operating at different frequency bands. Located in Western Australia, the SKA-Low will cover the frequency range 50 MHz - 350 MHz and comprise of 131,072 log-periodic antennas. At a higher frequency range of 350 MHz - 15.4 GHz, the 197 parabolic reflector antennas of the SKA-Mid will be located in the Karoo region in South Africa. A precursor of the SKA-Mid is the existing MeerKAT telescope with a total of 64 dishes.

Sub-sampled Exponential Analysis

Much of the theory of exponential analysis methods is based on the work done in 1795 by de Prony [4]. Originally it was designed for real-valued functions, but has since then been adapted for complex functions. When considering the function

$$f(x) = \sum_{i=1}^{n} \alpha_i \exp(\nu_i x), \tag{1}$$

Prony's method aims to determine the $2n$ complex parameters, linear parameters α_i and non-linear parameters ν_i [5]. The function is sampled at M uniformly spaced points

$$f_m = f(m\Delta) = \sum_{i=1}^{n} \alpha_i \exp(\nu_i m\Delta), \qquad m = 0, 1, ..., M-1, \tag{2}$$

where $M \geq 2n$. The sampling step is denoted by Δ.

Once the terms $\exp(\nu_i \Delta)$ are computed, the frequency contents $\Im(\nu_i)$ must be recovered from it. Here, $\Im(\cdot)$ denotes the imaginary part. Due to the periodicity of complex exponential signals, a one-to-one mapping between the former and the latter is not guaranteed, meaning the solution for $\Im(\nu_i)$ may not be unique. The possible solutions that are not true are known as aliases. To avoid this, we need to ensure that the argument $|\Im(\nu_i)|\Delta$ is small enough that only a single solution exists. Specifically, this requires that

$$\begin{aligned} |\Im(\nu_i)|\Delta &< \pi \\ \frac{2\pi|B|}{f_s} &< \pi \\ f_s &> 2|B|, \end{aligned} \tag{3}$$

where B is the highest frequency in the signal and f_s is the sampling frequency, the inverse of the sampling rate. The inequality in (3) is known as the Nyquist criterion. According to this criterion, the sampling frequency has to be larger than twice the frequency of the signal being sampled. If the signal is a sum of exponential terms, the sampling frequency has to be larger than twice the largest frequency present in the signal.

In some cases, having to sample at or above the Nyquist rate is not optimal. It signifies a restriction in terms of the useable samples, and a requirement for a large number of

samples if a specific range needs to be sampled. In direction-of-arrival (DOA) estimation, the DOA is a parameter that appears in the phase shift of signals arriving at neighbouring antenna elements. If the spacing between elements is too large (referred to as the spatial Nyquist limit), multiple solutions for the DOA exist for a certain phase shift. On the other hand, larger inter-element spacings are often preferred due to an increased angular resolution. For this reason, methods that allow sampling below the Nyquist rate are highly attractive.

Validated EXPonential Analysis (VEXPA)

Validated Exponential Analysis (VEXPA) was first introduced in [6] as a valuable add-on to existing exponential analysis methods. Its main appeal is that it makes use of a co-prime sampling configuration in order to recover from aliasing [7], meaning that sub-Nyquist sampled data can be used. Other features include the automatic estimation of the number of exponential terms, validation of the output, and robustness against outliers. VEXPA is the method that is used throughout this dissertation, where each application introduces some adjustments suited for its specific needs. In this section, an overview of the basic method is given. For simplicity, the one-dimensional case is described, although the method can easily be extended to two or more dimensions.

Scale-and-shift coprime sampling configuration

At the heart of it, the goal of VEXPA is to solve, as Prony did, for the coefficients and exponents of the function

$$f(x) = \sum_{i=1}^{n} \alpha_i \exp(\nu_i x), \tag{4}$$

while using sub-sampled data. Here, α_i and ν_i are complex values. In some cases, one is only interested in the exponents ν_i, in some cases one wants both the exponents and the coefficients α_i, and in some cases one wants to go further and use these exponents and coefficients to reconstruct a signal that was sparsely sampled.

For any of these cases, first consider a densely sampled signal with a sample rate Δ:

$$f_m = f(m\Delta) = \sum_{i=1}^{n} \alpha_i \exp(\nu_i m\Delta), \qquad m = 0, 1, ..., M-1. \tag{5}$$

Because it is densely sampled, the exponents ν_i can unambiguously be recovered from $\exp(\nu_i\Delta)$, due to the fact that $|\nu_i\Delta| < \pi$. It is important to note again that the samples are regularly spaced, as this is a requirement of Prony's method.

Now, introduce a scale parameter σ that will allow sampling at a sub-Nyquist rate. The new sampling rate ($\sigma\Delta$) is then equal to a scaled version of the original rate Δ:

$$f_{m\sigma} = f(m\sigma\Delta) = \sum_{i=1}^{n} \alpha_i \exp(\nu_i m\sigma\Delta), \qquad m = 0, 1, ..., M_\sigma - 1. \tag{6}$$

It should be noted that the new sampling rate may no longer adhere to the Nyquist criterion. From here on, we refer to the dense sampling rate Δ as the virtual sampling rate, and the samples in (6) as the scaled subset of samples.

Another parameter is introduced: ρ, known as the shift parameter. For reasons that will be clarified at a later stage, the scale and shift parameters σ and ρ should be co-prime, meaning that their greatest common divisor (GCD) should be 1. The shifted subset of samples is sampled at points shifted with a value $\rho\Delta$ from the scaled samples:

$$f_{m\sigma+\rho} = f\left((m\sigma+\rho)\,\Delta\right) = \sum_{i=1}^{n} \alpha_i \exp\left(\nu_i\,(m\sigma+\rho)\,\Delta\right), \qquad m = 0, 1, ..., M_\rho - 1. \tag{7}$$

The number of samples in the scaled subset and shifted subset are denoted by M_σ and M_ρ, respectively, and it is required that $M_\sigma \geq 2n$ and $M_\rho \geq n$.

Next, the base terms are introduced:

$$\Psi_i = \exp(\nu_i \Delta), \qquad i = 1, ..., n. \tag{8}$$

The equations (6) and (7) can then be rewritten as

$$f_{m\sigma} = \sum_{i=1}^{n} \alpha_i \exp\left(\nu_i m\sigma\Delta\right) = \sum_{i=1}^{n} \alpha_i (\Psi_i^\sigma)^m, \qquad m = 0, 1, ..., M_\sigma - 1 \tag{9}$$

and

$$f_{m\sigma+\rho} = \sum_{i=1}^{n} \alpha_i \exp\left(\nu_i\,(m\sigma+\rho)\,\Delta\right) = \sum_{i=1}^{n} (\alpha_i \Psi_i^\rho)(\Psi_i^\sigma)^m, \qquad m = 0, 1, ..., M_\rho - 1. \tag{10}$$

An example of the scale-and-shift sampling configuration can be seen in Fig. 1. Here, the virtual dense samples are indicated by the black dots, the scaled samples are indicated by the red crosses and the shifted samples are indicated by the blue circles.

Figure 1: An example of the scale-and-shift sampling configuration. The black dots, red crosses and blue circles signify the virtual dense samples, scaled samples and shifted samples, respectively.

We refer to Ψ_i^σ and Ψ_i^ρ as the scaled and shifted base terms, respectively. Because of the sub-Nyquist sampled data, there are multiple aliased Ψ_i that can be recovered from Ψ_i^σ and Ψ_i^ρ. To find the true ones, a de-aliasing method is needed, which is discussed later in this section. First, solutions for the aliased base terms Ψ_i^σ and Ψ_i^ρ are found.

Computing the aliased base terms

The first step of VEXPA is to determine the scaled base terms Ψ_i^σ. To do this, an underlying Prony-based exponential analysis method is used. Popular choices include the Matrix-Pencil method [8], Estimation of Signal Parameters via Rotational Invariance Techniques (ESPRIT) [9], MUltiple SIgnal Classification (MUSIC) [10], Root-MUSIC [11] and the Eigenvector method [12]. The choice of method depends on the application. With

the exception of the Eigenvector method, the chosen method uses only the scaled subset of samples $f_{m\sigma}$ for $m = 0, 1, ..., M_\sigma - 1$, as the shifted samples will only be used at a later stage. If using the Eigenvector method, it solves for both the scaled base terms Ψ_i^σ and shifted base terms Ψ_i^ρ and therefore uses all the samples.

Computing the coefficients

In order to compute the coefficients of the exponential terms, we first write the equations in (9) as a Vandermonde structured linear system

$$\begin{bmatrix} 1 & 1 & \dots & 1 \\ \Psi_1^\sigma & \Psi_2^\sigma & \dots & \Psi_N^\sigma \\ \vdots & \vdots & \ddots & \vdots \\ \Psi_1^{\sigma(M_\sigma-1)} & \Psi_2^{\sigma(M_\sigma-1)} & \dots & \Psi_N^{\sigma(M_\sigma-1)} \end{bmatrix} \begin{bmatrix} \alpha_1 \\ \alpha_2 \\ \vdots \\ \alpha_N \end{bmatrix} = \begin{bmatrix} f_0 \\ f_{1\sigma} \\ \vdots \\ f_{(M_\sigma-1)\sigma} \end{bmatrix}, \tag{11}$$

which can also be expressed as the compact version $V_N \alpha = F$. Here, N is an overestimation of the number of terms n, i.e., $n < N \leq M_\sigma/2$. If there is no noise present in this system, n of the N equations are linearly independent, meaning that any n of the possible equations can be solved to find the α_i. However, in most scenarios, especially when working with practical data, we have samples that are perturbed by noise [13]. This means there is no exact solution to the system, and a least-squares approach is followed instead.

Computing the shifted base terms

Now that solutions are found for both Ψ_i^σ and α_i, the next step is to find the shifted base terms Ψ_i^ρ. Let us recall the shifted set of samples:

$$f_{m\sigma+\rho} = \sum_{i=1}^{n} \alpha_i \exp\left(\nu_i \left(m\sigma + \rho\right) \Delta\right) = \sum_{i=1}^{n} (\alpha_i \Psi_i^\rho)(\Psi_i^\sigma)^m, \qquad m = 0, 1, ..., M_\rho - 1. \tag{12}$$

As with the scaled set of samples in (11), a structured Vandermonde linear system is set up:

$$\begin{bmatrix} 1 & 1 & \dots & 1 \\ \Psi_1^\sigma & \Psi_2^\sigma & \dots & \Psi_N^\sigma \\ \vdots & \vdots & \ddots & \vdots \\ \Psi_1^{\sigma(M_\rho-1)} & \Psi_2^{\sigma(M_\rho-1)} & \dots & \Psi_N^{\sigma(M_\rho-1)} \end{bmatrix} \begin{bmatrix} \alpha_1\Psi_1^\rho \\ \alpha_2\Psi_2^\rho \\ \vdots \\ \alpha_N\Psi_N^\rho \end{bmatrix} = \begin{bmatrix} f_\rho \\ f_{\sigma+\rho} \\ \vdots \\ f_{(M_\rho-1)\sigma+\rho} \end{bmatrix}. \tag{13}$$

Seeing as $M_\rho \geq N$, the linear set of equations in (13) is solved to find the solutions to $\alpha_i \Psi_i^\rho$. From here, the shifted base terms are calculated as

$$\Psi_i^\rho = \frac{\alpha_i \Psi_i^\rho}{\alpha_i}, \tag{14}$$

since the α_i are already known.

Estimating the number of terms

VEXPA typically makes use of cluster analysis to estimate the number of terms as follows. Let us denote the number of snapshots as N_t. The underlying method is then solved a total of N_t times, with each execution using data of a different snapshot. Each snapshot delivers N results for Ψ_i^σ for $i = 1, ..., N$, where N is an overestimation of n. In turn, the same number of results are returned for Ψ_i^ρ.

Because of the random noise, only the n true solutions will cluster around the same position for each snapshot, whereas the $N - n$ noisy or spurious base terms will be dispersed randomly [7]. The number of terms will therefore be equal to the number of clusters formed by the solutions of Ψ_i^σ and Ψ_i^ρ. An example is shown in Fig. 2, where the number of detected clusters is four, from which it follows that $n = 4$.

A well-known cluster analysis algorithm that is often used by VEXPA is Density-Based Spatial Clustering of Applications with Noise (DBSCAN) [14].

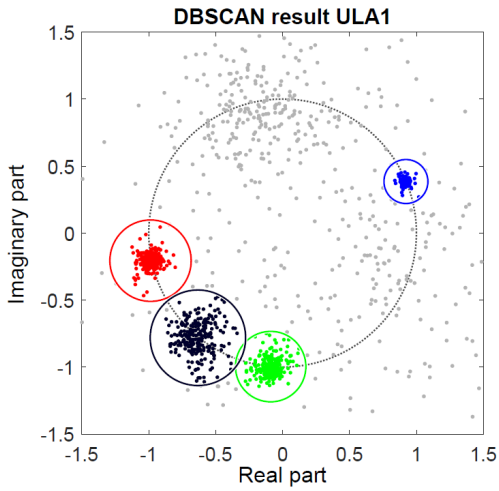

Figure 2: The clustering results using DBSCAN to illustrate the estimation of the number of terms. The total set of solutions for Ψ_i^σ are shown by the grey markers, with the ones forming clusters shown by the different coloured markers. In this case, the number of clusters is four, and therefore n is also estimated as $n = 4$.

Recovering the de-aliased base terms

At this stage of the method, the parameter n and the solutions to Ψ_i^σ and Ψ_i^ρ for $i = 1, ..., n$ have been found. Because of the sparseness of the data, multiple solutions for Ψ_i exist. The possible solutions can be found by taking the roots of Ψ_i^σ:

$$\begin{aligned} \Psi_i &= (\Psi_i^\sigma)^{\frac{1}{\sigma}} \\ &= \exp\left(\nu_i \Delta \sigma\right)^{\frac{1}{\sigma}} \\ &= \left\{ \exp\left(\nu_i \Delta + \frac{2\pi j}{\sigma} \ell\right) : \ell = 0, \ldots, \sigma - 1 \right\}. \end{aligned} \tag{15}$$

In a similar fashion, one can find the possible base terms from Ψ_i^{ρ}:

$$\begin{aligned}\Psi_i &= (\Psi_i^{\rho})^{\frac{1}{\rho}} \\ &= \exp\left(\nu_i \Delta \rho\right)^{\frac{1}{\rho}} \\ &= \left\{\exp\left(\nu_i \Delta + \frac{2\pi j}{\rho} k\right) : k = 0, \ldots, \rho - 1\right\}.\end{aligned} \tag{16}$$

There are therefore two sets of solutions for each Ψ_i of respective sizes of σ and ρ. Here, the importance of choosing σ and ρ as coprime becomes clear. Due to this coprimeness, there will be only one result for Ψ_i that appears in both sets. The true solution can therefore be obtained by finding the intersection of the two sets. This is visually explained in Fig. 3. For this example, $\nu_i \Delta = 1.5\pi j$, $\Psi_i = \exp(\nu_i \Delta) = -1j$, $\sigma = 5$ and $\rho = 3$. Note that we denote imaginary numbers by the symbol j. The 5 solutions from $(\Psi_i^{\sigma})^{\frac{1}{\sigma}}$ and 3 solutions from $(\Psi_i^{\rho})^{\frac{1}{\rho}}$ are indicated by the blue circles and red crosses, respectively. The true solution is found at the location where the circle and cross coincide.

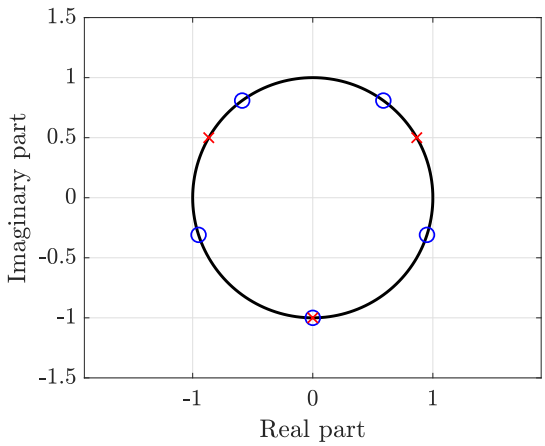

Figure 3: The two sets of solutions for $(\Psi_i^{\sigma})^{\frac{1}{\sigma}}$ (blue circles) and $(\Psi_i^{\rho})^{\frac{1}{\rho}}$ (red crosses). For this example, $\sigma = 5$ and $\rho = 3$, explaining the 5 circles and 3 crosses. The true solution for Ψ_i will be at $[0 - j]$, where the circle and cross coincide.

Now, all the parameters have been found. From here, the important information can be extracted from the de-aliased base terms, or the signal can be reconstructed. Next, we describe the relevant applications of VEXPA.

Direction-of-Arrival Estimation

Direction-of-arrival (DOA) estimation refers to the method of estimating the angle at which electromagnetic waves are impinging on an antenna array [15]. Some of the applications for DOA estimation include radio frequency interference (RFI) identification,

radar, sonar and seismology [16]. To approach the DOA estimation problem, most methods make the following assumptions [16]:

- *Isotropic and linear transmission medium*: By assuming that the incoming signal travels through a medium that is both isotropic and linear, it is construed that the propagation properties of the signal are not dependent on the angle of arrival, and that multiple incoming signals can be superimposed linearly to compute the received signal at a specific element.
- *Source in far-field of array*: The far-field of a receiving antenna array is defined as the region that is at a distance big enough that an incoming signal will have a planar, rather than a curved, wavefront. Specifically, this distance is defined as $r > 2D^2/\lambda$, with D the dimension of the array and λ the wavelength. By assuming all sources are in the far-field, the incoming signals are all parallel to one another.
- *Narrowband signals*: It is assumed that the frequency contents of the incoming signals are narrowly distributed around the centre frequency f_c. This implies that during the time taken for the signal to traverse the full array, there is no variation in the signal frequency.
- *Additive White Gaussian Noise (AWGN) channel*: It is assumed that the noise of the signals is additive complex white Gaussian noise with zero mean. The noise is uncorrelated among the different receiving antennas.

Consider n signals, denoted by $s_i(t)$ for $i = 1, ..., n$ arriving at a uniform linear array (ULA) with M antenna elements. Due to the narrow-band assumption, each signal has a slowly varying amplitude and phase [17]. The received sample at antenna m is then

$$f_m(t) = \sum_{i=1}^{n} s_i(t) \exp\left(-j\omega m \tau_i\right), \qquad m = 0, 1, ..., M-1, \tag{17}$$

where ω is the frequency in radians, and τ_i are the respective time delays caused by the inter-element spacing. The latter is given by

$$\tau_i = \frac{d \cos \phi_i}{c}, \tag{18}$$

where d is the inter-element spacing, ϕ_i is the ith angle of arrival, and c is the speed of light. The goal of DOA estimation methods is to find the ϕ_i for $i = 1, ..., n$.

Considering the top expression in (3), the Nyquist limit for the DOA estimation application is

$$\begin{aligned} \left|\frac{\omega d \cos \phi_i}{c}\right| &< \pi \\ \frac{2\pi f d |\cos \phi_i|}{c} &< \pi \\ \frac{2d |\cos \phi_i|}{\lambda} &< 1 \\ d &< \frac{\lambda}{2|\cos \phi_i|}. \end{aligned} \tag{19}$$

Since the maximum value of $|\cos\phi_i|$ is 1, the equation above can simplify to $d < \lambda/2$. This means that arrays with inter-element spacings of larger than half a wavelength, known as sparse arrays, are unable to identify incoming signals unambiguously. This ambiguity is seen in the antenna radiation pattern as unwanted large beams, referred to as grating lobes. Since grating lobes diminish the power in the main beam, they should be avoided in most applications. Essentially, the grating lobes are aliases of the main beam.

Sparse arrays have some advantages over dense arrays. The angular resolution in radians that can be resolved by a ULA is given by

$$\Delta_\phi = \frac{\lambda}{D}, \tag{20}$$

with D once again the dimension of the array. An array with M elements will then clearly have a finer resolution if the inter-element spacing is larger. Sparse arrays therefore have the advantage of a better resolution compared to a dense array with the same number of elements.

Another advantage of sparse arrays is reduced mutual coupling, which is the interaction of two antennas in the same vicinity, causing some of the energy directed to the one to be received by the other [18]. This interaction is caused by the nonideal directional characteristics of practical antennas, and is more prominent if the antennas are closer together. In most applications, mutual coupling is undesired, and therefore sparse arrays are preferred in this regard.

With the benefits that sparse arrays pose, DOA estimation is clearly an application that can gain from the use of sub-sampled analysis, as will be shown in Part 1 of this dissertation.

One-Bit DOA Estimation Using VEXPA

Consider a fixed time t and take the narrowband assumption into account, which states that the signal response does not change significantly as the signal traverses the array [17]. The equation (17) can then be written as

$$f_m = \sum_{i=1}^{n} s_i \exp(\psi_i m d), \qquad m = 0, 1, ..., M-1, \tag{21}$$

where

$$\psi_i = \frac{-j\omega\cos\phi_i}{c}. \tag{22}$$

Relating (5) and (21), it is seen that the DOA estimation problem follows the sampling scheme of Prony's method, where the inter-element spacing d is the equivalent regular sampling step and s_i are the coefficients.

The sub-sampled scale-and-shift configuration can then be created through the use of two sub-ULAs, each with an inter-element spacing of σd. The positions of the second ULA elements are the the same as the first ULA but shifted with a spacing ρd. This concept is elaborated in Part 1.

For cases where the antenna samples are quantised to one bit of data, the amplitude information is lost and therefore the coefficients s_i can not be retrieved accurately.

The classic VEXPA method described in this chapter, where the shifted base terms are computed from the coefficients, therefore needs to be altered to be independent of the coefficients. This requirement introduces the eigenvector method [19], which computes the scaled and shifted base terms concurrently and omits the calculation of the coefficients. This method is described in more detail in Chapter 2.

Antenna Position Estimation

Some antenna arrays are required to operate at a large fractional bandwidth, which means a strictly dense configuration would require an inter-element spacing less than half a wavelength at the highest frequency [20]. This means that the array is over-sampled at the lower range of the frequency band, which is undesirable due to the cost. A solution to this problem is a sparse spacing at the higher frequencies in the band.

A method that is used to alleviate the effect of the grating lobes of sparse arrays is to disturb the regularity of the array grid. This helps to spread out the grating lobes over all angles, smoothing out the main beam over frequency and scan angle. Irregular arrays have the added benefit that a fast and slightly inaccurate placement of the elements will not affect the performance significantly, but this also means an accurate knowledge of the element positions is lacking.

For large irregular arrays such as the Low-Frequency Aperture Array (LFAA) system of the SKA, the large number of antennas (up to hundreds of thousands) creates a difficulty in the precise placement of these elements. Moreover, the human error of connecting the cable of one element to a channel of another at the back-end becomes more likely when the number of antennas and cables is very large. Incorporating a method that accurately finds the positions after the antennas have already been installed could therefore help to save costs since less accuracy is required while placing the antennas [21].

The main idea of the method is to transmit harmonically related signals from an unmanned aerial vehicle (UAV) at a known position in the sky [22]. Essentially, the antenna position estimation problem is the inverse of the direction-of-arrival problem. For the former, the DOA is known and the position is extracted from the time delay; for the latter, it is the opposite case. However, the assumption made for the DOA problem that the source is in the far-field of the receiving array is no longer true, since feasible flight paths of the UAV will occupy the near-field. This requires a linearisation step in the VEXPA method, which is described in Chapter 3.

The Low Frequency Array (LOFAR) [23] is an important precursor to the LFAA of the SKA-Low. Developed by the Netherlands Institute for Radio Astronomy (ASTRON), it consists of 38 stations in the Netherlands and 14 international stations across Europe [24]. Two frequency bands are covered by LOFAR: the Low Band Antenna (LBA) array operating at 10 - 90 MHz, and the High Band Antenna (HBA) array at 110 - 240 MHz. The LBA is a sparse irregular configuration and is used as an example when employing our antenna position estimation method.

Part 2 of this dissertation is dedicated to the discussion of the application of sub-sampled exponential analysis to solve the antenna position estimation problem.

Antenna Position Estimation Using VEXPA

A UAV transmits narrowband odd harmonic signals at time t_p from a position $\mathbf{r}_p = x_p\mathbf{x} + y_p\mathbf{y} + z_p\mathbf{z}$ in the sky. The samples at the m_{th} antenna element on the ground at time t_p for frequency i are [22]:

$$f_{mip} = s_i(t_p)\exp(j\omega_i t_p)\exp\left((2i+1)\,\Psi_{mp}\right), \tag{23}$$

where the index $i \in \mathbb{N}$ distinguishes between frequencies $\omega_i = (2i+1)\omega_0$. The base frequency is $\omega_0 = 2\pi f_0$. The base terms Ψ_{mp} are defined as

$$\Psi_{mp} = j\omega_0\tau_{mp}, \tag{24}$$

with

$$\begin{aligned} \tau_{mp} &= \tau_m\left(x_p, y_p, z_p\right) = \frac{1}{c}\left(r_p - \sqrt{r_p^2 + \Delta_{mp}}\right), \\ \Delta_{mp} &= u_m^2 + v_m^2 - 2(u_m x_p + v_m y_p), \end{aligned} \tag{25}$$

where $r_p = \|\mathbf{r}_p\|$, and u_m and v_m are the unknown x- and y-positions of the m_{th} antenna, respectively. The sample set of each antenna are divided by that of the reference antenna ($m = 0$) to give

$$f'_{mip} = \frac{f_{mip}}{f_{0ip}} = \exp\left((2i+1)\,\Psi_{mp}\right). \tag{26}$$

From the above equation, we can see that in this case, the regular sampling step used by VEXPA is $2\omega_0$. The time delay τ_{mp} is more complex than that of the DOA estimation problem, since here it is assumed that the UAV is in the near-field of the antenna array, meaning that the incoming signal has a curved phase front. Because there is only one signal transmitted from the UAV, no detection of the number of signals is required.

The near-field base terms Ψ_{mp} are non-linear, thus the model is first linearised using a first order Taylor series partial sum. Another implication is that, instead of the usual scale-and-shift configuration of VEXPA, two coprime scale parameters (σ_j, j = 1,2) are used that relate to the height z_p of the UAV. This is discussed in detail in Chapter 3.

Ripple Characterisation

Reflector antennas operate by reflecting and transmitting incident plane waves from each reflector to a focal point [25]. The feed antenna is located at the focal point, and is usually a horn antenna. The largest reflector is known as the main reflector, with the remaining ones referred to as the sub reflectors.

The design of the MeerKAT telescope as well as the SKA-Mid is that of an offset Gregorian configuration. The term "Gregorian" refers to the fact that the shape of the sub reflector is an ellipsoid. The alternative is a Cassegrain layout, for which the shape of the sub reflector is a hyperboloid. The two different configurations are portrayed in Fig. 4.

The term "offset" refers to the fact that the antenna feed is not directly in front of the reflector, but rather offset to the side of the reflector. An offset reflector has the advantage that there is reduced blockage from the feed, supporting struts and sub reflector surface. Fig. 5 shows both a front feed and offset feed reflector.

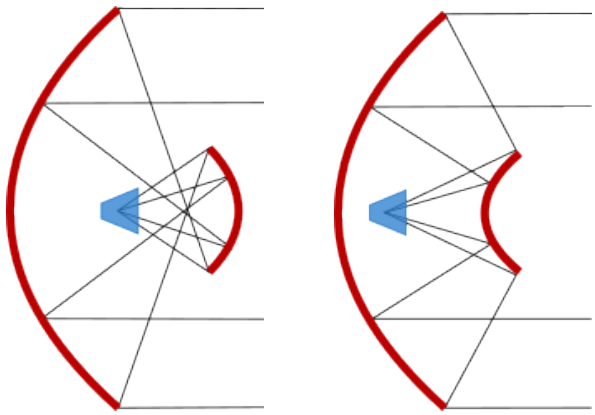

Figure 4: Gregorian (left) vs Cassegrain (right) reflector configuration

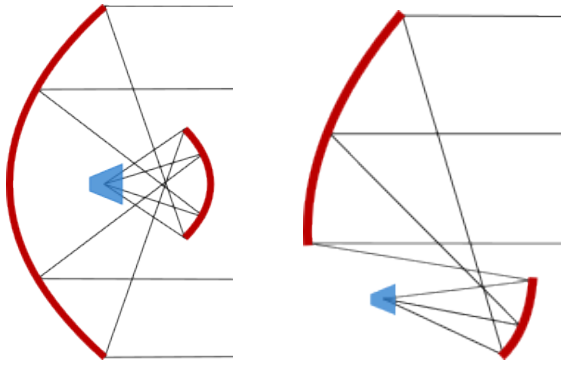

Figure 5: Front feed (left) vs offset (right) reflector configuration

Using spherical coordinates $\Omega = (\theta, \phi)$, the electric fields in the far-field of an antenna system can be described by

$$\mathbf{E}(f, \Omega) = E_\theta(f, \Omega)\hat{\boldsymbol{\theta}} + E_\phi(f, \Omega)\hat{\boldsymbol{\phi}}, \tag{27}$$

where the angle from zenith is denoted by θ and the azimuthal angle by ϕ. The operating frequency is f. From the electric field pattern, the radiation intensity can be computed, which is the radiated power per unit solid angle [25]:

$$P\left(f, \Omega\right) = \frac{r^2}{2\eta}\left(\left|E_\theta\left(f, \Omega\right)\right|^2 + \left|E_\phi\left(f, \Omega\right)\right|^2\right), \tag{28}$$

where r is the radius at which the electric field components are evaluated, and η is the intrinsic impedance of free space ($\eta = 120\pi\ \Omega \approx 377\ \Omega$).

Reflector antennas are often described in terms of electrical size, which is given as a number of wavelengths at a certain frequency. Since most reflectors are designed to operate over a frequency range, its electrical size will therefore increase with frequency while its physical size remains constant [26]. Small reflectors have evident advantages compared to larger ones such as reduced cost due to fewer materials and simpler manufacturing. Their compact and lightweight design also contribute to easier transportation and deployment.

The downside, however, to small reflectors is that non-ideal effects become more pronounced as the size of the reflector decreases. One of these effects is edge diffraction. This is the phenomenon where waves reaching a metal surface bend around the edges of the surface due to the spherical radiation caused by surface currents on these edges. This leads to radiation occurring in the shadow region behind the surface.

To understand why the effect of edge diffraction worsens as the size of the reflector decreases, consider two reflectors of different sizes. The ratio of the circumference to the area of the reflector will be larger for the smaller reflector, since the circumference scales linearly with the radius while the area scales quadratically [26]. The amount of diffracted energy is directly related to the circumference, since diffraction occurs at the edges of the reflector. On the other hand, the amount of directed energy is directly related to the radiating area. Because the ratio of circumference to area is higher for the smaller reflector, the ratio of diffracted to directed energy will also be higher, leading to more prominent non-idealities in the total radiation pattern.

The differences in path length between the fields reflected by the main reflector and the fields diffracted by the sub reflector will cause general interference. Specifically, the sub-reflected diffracted fields are smaller than the reflected fields, and this will result in a small ripple appearing on the main reflector fields over frequency [27]. This ripple will subsequently also appear in figures of merit that are influenced by the radiation pattern, such as the sensitivity, aperture efficiency and antenna noise temperature. It is important that this ripple is characterised and, if possible, minimised through optimisation of the reflector design.

Sensitivity

A primary figure of merit of reflectors is the so-called sensitivity, which is defined as the minimum detectable signal on a given collecting area [26]. Non-idealities such as

the previously-described interference of diffracted and reflected fields cause a ripple in the sensitivity over frequency. This ripple is negligible in larger reflector systems but is noticeable in smaller reflectors. This means that a fast and accurate computation of the sensitivity is more difficult.

The importance of the characterisation of the sensitivity ripple lies in the fact that, when the frequency response of the reflector is analysed, this ripple could be mistaken for a radio source, since the spectral widths of the ripples are often similar to those of HI galaxies [28]. It is therefore critical that the ripples are characterised to allow distinction between observations caused by instrumentation and true sources. However, this characterisation requires sampling the radiation pattern at Nyquist rate, which means a significant number of simulations at different frequencies are required. This is computationally expensive and introduces the appeal of using sub-sampled exponential analysis to reduce the number of frequency simulations and in turn the computational load.

The sensitivity is defined as the ratio between the effective aperture area and the system noise temperature

$$\frac{A_{\mathrm{e}}}{T_{\mathrm{sys}}} = \frac{\eta_{\mathrm{ap}} A_{\mathrm{phy}}}{T_{\mathrm{A}} + T_{\mathrm{rec}}}. \tag{29}$$

The product of the aperture efficiency η_{ap} and physical aperture area A_{phy} equates to the effective aperture area, while the addition of the antenna noise temperature T_{A} and the receiver noise temperature T_{rec} gives the system noise temperature. Assuming that the low-noise amplifier (LNA) and antenna are well-matched, the receiver noise temperature T_{rec} is slowly varying with frequency, while the physical aperture area A_{phy} is a constant. This means that the ripple behaviour noticed in the sensitivity mostly stems from the aperture efficiency η_{ap} and antenna noise temperature T_{A}.

Aperture Efficiency

The aperture efficiency η_{ap} of a reflector is defined as the ratio of the co-polarisation radiation intensity on axis to the radiation intensity of an aperture producing the same total power but without any cross-polarisation [29], computed as

$$\eta_{\mathrm{ap}} = \frac{\lambda^2 |E_{\mathrm{co}}(f,0,0)|^2}{A_{\mathrm{phy}} P_{\mathrm{rad}}}. \tag{30}$$

The co-polarisation component $E_{\mathrm{co}}(f,0,0)$ is defined by Ludwig's third definition [30]. Specifically, it is evaluated at the direction of the main beam, and at a frequency f with corresponding wavelength λ. The physical area of the aperture A_{phy} is determined by the main reflector and the total power radiated by the antenna is denoted as P_{rad}.

The aperture efficiency can be approximated as a product of a few sub-efficiencies [31]

$$\eta_{\mathrm{f}} = \eta_{\mathrm{BOR1}} \eta_{\mathrm{ill}} \eta_{\mathrm{sp}} \eta_{\mathrm{pol}} \eta_{\mathrm{ph}} \eta_{\mathrm{st}} \eta_{\mathrm{ab}} \eta_{\mathrm{d}}, \tag{31}$$

where the specific sub-efficiencies are defined as:

- η_{BOR1}: the Body Of Revolution Type 1 (BOR1) efficiency, relating to the rotational symmetry of the feed pattern,
- η_{ill}: the illumination efficiency, which relates to the uniformity of the field amplitude distribution over the surface of the reflector,

– η_{sp}: the spillover efficiency, which relates to the power radiated within the taper angle of the feed compared to the total power radiated by the feed,

– η_{pol}: the cross polarisation efficiency, relating to the amount of power radiated in the co-polar component relative to the total power radiated in the designed taper angle of the feed,

– η_{ph}: the phase efficiency, which relates to the proximity of the phase centre of the feed relative to the focus point of the reflector, which is an indication of the uniformity of the phase distribution in the aperture plane,

– η_{st}: the surface tolerance efficiency, which relates to manufacturing errors in the surface,

– η_{ab}: the aperture blockage efficiency, which relates to physical components that block the aperture area,

– η_{d}: the diffraction efficiency, which relates to the losses due to diffraction, e.g. edge diffraction.

The approximation in (31) does not take the frequency ripple into account, which is why (30) is preferred for accuracy. The calculation is made with only the main beam radiation pattern, i.e., one direction, which makes it easier and faster to simulate than the antenna noise temperature.

Antenna Noise Temperature

The antenna noise temperature is a measure of the total noise received by an antenna. It is calculated as

$$T_A\left(f|\hat{\boldsymbol{r}}_0\right) = \frac{\iint_{4\pi} N\left(f,\Omega|\hat{\boldsymbol{r}}_0\right)\sin\theta d\Omega}{P_{\text{rad}}}, \tag{32}$$

where

$$N\left(f,\Omega|\hat{\boldsymbol{r}}_0\right) = T_b\left(f,\Omega\right)P\left(f,\Omega|\hat{\boldsymbol{r}}_0\right). \tag{33}$$

The product in (33) consists of the brightness temperature $T_b\left(\cdot\right)$ and the antenna radiation intensity $P\left(\cdot\right)$, with the reflector pointing in the direction $\hat{\boldsymbol{r}}_0$ and operating at frequency f [32]. This product can be approximated as

$$N\left(f,\Omega|\hat{\boldsymbol{r}}_0\right) = \begin{cases} P\left(f,\Omega|\hat{\boldsymbol{r}}_0\right)T_{\text{b}}^{\text{sky}}\left(f,\theta\right), & 0 \le \theta \le \pi/2, \\ P\left(f,\Omega|\hat{\boldsymbol{r}}_0\right)\left[\left(1-\tilde{\Gamma}(\pi-\theta)\right)T_{\text{gnd}} + \tilde{\Gamma}(\pi-\theta)T_{\text{b}}^{\text{sky}}\left(f,\pi-\theta\right)\right], & \pi/2 < \theta \le \pi, \end{cases} \tag{34}$$

where $\tilde{\Gamma}$ is the average reflection coefficient for the ground [26]. The ground temperature is denoted as T_{gnd} and assumed to be 300 K, while $T_{\text{b}}^{\text{sky}}$ is the sky noise model.

The sky noise model, or sky brightness temperature, includes the temperature due to atmospheric absorption, the cosmic microwave background (CMB) and the galactic emission. The latter consists mostly of synchrotron emission, which is produced by the acceleration of ultrarelativistic electrons by a magnetic field [33]. Ultrarelativistic electrons have kinetic energies much larger than their rest mass ($E \gg m_e c^2$).

The synchrotron emission has a power law response, which then dominates the response of the antenna noise temperature T_A for relatively low microwave frequencies (below a few GHz), as seen in Chapter 5. On top of this power law shape is the contribution of the ripple that originates from the radiation intensity $P\left(f, \Omega|\hat{\boldsymbol{r}}_0\right)$.

The antenna noise temperature is calculated over the 4π steradian sphere and therefore its ripple is influenced by the ripple in the radiation intensity for each direction. The radiation intensity at each direction is weighed with the brightness temperature at that direction, which means that some directions will have a larger contribution to the T_A ripple than others. For these reasons, characterising the ripple in the antenna noise temperature is a more challenging task than that of the aperture efficiency, as will be seen in Chapter 6.

Ripple Characterisation Using VEXPA

The main difference between the ripple characterisation and the previous applications is that in this case, no physical parameter (such as a DOA or antenna position) needs to be extracted. Rather, we want to model a function using an exponential model. Furthermore, we are mostly interested in the frequency components in this exponential model, to get an understanding of the ripple behaviour.

In the first case, we want to model the real-valued antenna noise temperature as

$$T_A(f) = \sum_{i=1}^{n} a_i \exp\left(\nu_i f\right), \qquad a_i, \nu_i \in \mathbb{C}. \tag{35}$$

Dropping the subscript A, the temperature function is sampled at a regular dense interval, giving the samples

$$T_m = \sum_{i=1}^{n} a_i \exp\left(\nu_i f_0\right) \exp\left(\nu_i m \Delta\right), \tag{36}$$

for $m = 0, 1, ..., M-1$. A few pairs of scale and shift parameters are then used to determine subsets of samples for which the exponential analysis problem is solved individually. It should be mentioned that a densely-sampled function is assumed, but that the coprime sampling configuration is used in order to find solutions from a few subsets of samples instead of one solution from all the available samples. By doing this, a final, trustworthy solution can be found by seeing which one occurs for all or most cases.

Because only one snapshot of data is available, this application of VEXPA does not use cluster analysis to determine n, but rather an iterative method that increases the estimate of n until a reconstruction with a small enough error at the sampled points is found. This is described in Chapter 6.

The procedure for the reconstruction of the electric fields is very similar, except for the fact that the co-prime parameters are used for the sub-sampling of the function rather than just for validation. Both of the orthogonal components of the electric field are modelled for every required direction. If the goal is to characterise the ripple in the antenna noise temperature, this means all the directions considered for the integration over the 4π steradian sphere. On the other hand, if the goal is to characterise the ripple in the aperture efficiency, this means only the single direction of the reflector main beam.

Contributions

The following contributions arose from this research project:

1. The use of one-bit quantised data in the direction-of-arrival (DOA) estimation problem was investigated. A method was proposed that accurately obtains the DOAs of multiple sources impinging on sparse uniform linear arrays (ULAs). This method is also capable of accurately finding the number of incoming signals. The findings of this research were recorded in a conference paper [34] and a research letter [12]:

   (a) R.-M. Weideman, R. Louw and D.I.L. de Villiers, "Practical performance of the VEXPA estimation method in sparse regular arrays," *2021 XXXIVth General Assembly and Scientific Symposium of the International Union of Radio Science (URSI GASS)*, Rome, Italy, 2021, pp. 1-4, doi: 10.23919/URSI-GASS51995.2021.9560510.

   (b) R.-M. Weideman, F. Knaepkens, A. Cuyt, R. Raal, D.I.L. de Villiers and W.-S. Lee, "One-bit Direction-of-Arrival Estimation with Sparse Arrays," submitted.

2. A method was developed to estimate the positions of antenna elements in large sparse irregular arrays by transmitting harmonically related signals from an unmanned aerial vehicle (UAV) at known positions in the sky. The method is able to solve these positions when the UAV is in the near-field of the array by making use of a linearisation step. It was shown that the method works well with synthetic data as well as simulated data including practical effects such as mutual coupling. A research letter [22] and conference paper [35] describe the method and results:

   (a) R. Louw, F. Knaepkens, A. Cuyt, W.-S. Lee, S.J. Wijnholds, D.I.L. de Villiers, and R.-M. Weideman, "Antenna position estimation through sub-sampled exponential analysis of harmonically related input signals," in *URSI Radio Science Letters*, vol. 3, 2021. [Online]. Available: https://www.ursi.org/publications.php, 2021, pp. 1–4.

   (b) R.-M. Weideman, R. Louw, F. Knaepkens, D.I.L. de Villiers, A. Cuyt, W.-S. Lee, and S.J. Wijnholds, "Simulated performance of antenna position estimation through sub-sampled exponential analysis," in *2022 International Conference on Electromagnetics in Advanced Applications (ICEAA)*, Cape Town, South Africa, 2022, pp. 128–132, doi: 10.1109/ICEAA49419.2022.9900012.

3. The characterisation of the frequency ripple in reflector figures of merit such as aperture efficiency and antenna noise temperature was explored. Firstly it was shown how the frequency contents of the antenna noise temperature can accurately be described by using densely-sampled points. Subsequently, a method was established to model the reflector electric fields from sub-sampled data, whereafter accurate reconstructions of the previously mentioned figures of merit can be obtained. This research led to a conference paper [36] and a journal paper [32]:

   (a) R.-M. Weideman, A. Cuyt and D.I.L. De Villiers, "Characterising the Frequency Ripple in Antenna Noise Temperature Using Exponential Analysis," in

International Conference on Electromagnetics in Advanced Applications (ICEAA), Venice, Italy, 2023, in press.

(b) R.-M. Weideman, A. Cuyt and D.I.L. De Villiers, "Characterising the Electric Field Ripple in Reflector Antennas Using sub-sampled Exponential Analysis," submitted.

Conclusion

Sub-sampled exponential analysis methods allow sampling at a sub-Nyquist rate, which poses benefits such as improved computational complexity and increased resolution. The VEXPA method makes use of an underlying Prony-based method and builds on it by making use of a scale-and-shift coprime configuration.

In this dissertation, we use VEXPA in three main applications: direction-of-arrival estimation with quantised data, antenna position estimation and frequency ripple characterisation in reflector systems. The latter is described as two sub-applications: firstly, characterising the frequency contents of a well-known antenna noise temperature model, and secondly, sub-sampling the reflector electric fields and reconstructing them to identify the ripple across frequency. All of these applications adjust the VEXPA method to optimise its working for the specific problem description. Table 1 summarises the main specifications and variations of the different applications.

The versatility of the VEXPA method can be seen in the reliable performance and accurate results when used in different applications. If the problem statement is understood well, the adequate adaptions can be made to the method to fit the specific application at hand. This promises us that VEXPA is suitable to solve a myriad of real-world cases that are yet to be explored.

References

[1] "What Is Radio Astronomy?" (2023), [Online]. Available: `https://www.skatelescope.org/radio-astronomy/`.

[2] "The SKA Project." (2023), [Online]. Available: `https://www.skatelescope.org/the-ska-project/`.

[3] "SKAO: Science Goals". (2023), [Online]. Available: `https://www.skao.int/index.php/en/explore/science-goals/`.

[4] R. de Prony, "Essai expérimental et analytique sur les lois de la dilatabilité des fluides élastiques et sur celles de la force expansive de la vapeur de l'eau et de la vapeur de l'alkool, à différentes températures", *J. Ec. Poly.*, vol. 1, no. 22, pp. 24–76, 1795.

[5] L. Weiss and R. McDonough, "Prony's method, Z-transforms, and Padé approximation", *SIAM Rev.*, vol. 5, pp. 145–149, 1963.

[6] M. Briani, A. Cuyt, F. Knaepkens, and W.-S. Lee, "VEXPA: Validated EXPonential Analysis through regular subsampling", *Signal Processing*, vol. 177, p. 107 722, 2020, ISSN: 0165-1684.

Table 1: Main specifications of VEXPA in different applications

One-bit Direction-of-Arrival	
Regular dense parameter	Virtual inter-element spacing d
Underlying method	Eigenvector method
Estimating n	DBSCAN
Dimension	1D
Antenna Position Estimation	
Regular dense parameter	Virtual dense frequency ω_0
Underlying method	Root-MUSIC
Estimating n	N/A - only one source
Dimension	2D
Antenna Noise Temperature Ripple Characterisation	
Regular dense parameter	Dense sampling step Δ
Underlying method	Matrix Pencil
Estimating n	Iterative method - see Chapter 6
Dimension	1D
Electric Field Reconstruction	
Regular dense parameter	Dense sampling step Δ
Underlying method	Matrix Pencil
Estimating n	Iterative method - see Chapter 6
Dimension	1D

[7] A. Cuyt and W.-S. Lee, "How to get high resolution results from sparse and coarsely sampled data", *Appl. Comput. Harmon. Anal.*, vol. 48, pp. 1066–1087, 2020, (Published online October 11, 2018. Toolbox and experiments downloadable.)

[8] Y. Hua and T. K. Sarkar, "Matrix pencil method for estimating parameters of exponentially damped/undamped sinusoids in noise", *IEEE Transactions on Acoustics, Speech, and Signal Processing*, vol. 38, no. 5, pp. 814–824, 1990.

[9] R. Roy and T. Kailath, "ESPRIT–estimation of signal parameters via rotational invariance techniques", *IEEE Transactions on acoustics, speech, and signal processing*, vol. 37, no. 7, pp. 984–995, 1989.

[10] R. Schmidt, "Multiple emitter location and signal parameter estimation", *IEEE Transactions on Antennas and Propagation*, vol. 34, no. 3, pp. 276–280, 1986.

[11] A. Barabell, "Improving the resolution performance of eigenstructure-based direction-finding algorithms", in *ICASSP '83. IEEE International Conference on Acoustics, Speech, and Signal Processing*, vol. 8, 1983, pp. 336–339.

[12] R.-M. Weideman, F. Knaepkens, A. Cuyt, R. Raal, and D. I. L. De Villiers, "One-bit direction-of-arrival estimation with sparse arrays", submitted.

[13] F. Knaepkens, "Multidimensional exponential analysis: Theory and applications", Ph.D. dissertation, University of Antwerp, 2022.

[14] M. Ester, H.-P. Kriegel, J. Sander, X. Xu, *et al.*, "A density-based algorithm for discovering clusters in large spatial databases with noise.", in *Kdd*, vol. 96, 1996, pp. 226–231.

[15] T. Tuncer and B. Friedlander, *Classical and Modern Direction-of-Arrival Estimation*. Elsevier Science, 2009, ISBN: 9780080923079.

[16] Z. Chen, G. Gokeda, and Y. Yu, *Introduction to Direction-of-arrival Estimation* (Artech House signal processing library). Artech House, 2010, ISBN: 9781596930902.

[17] F. Knaepkens, A. Cuyt, W.-S. Lee, and D. I. L. de Villiers, "Regular sparse array direction of arrival estimation in one dimension", *IEEE Trans. Antennas Propag.*, vol. 68, pp. 3997–4006, 2020, (Published online January 08, 2020).

[18] C. Balanis, *Antenna Theory: Analysis and Design*. Wiley, 1996, ISBN: 9780471592686.

[19] A. Cuyt and W.-S. Lee, "Multiscale matrix pencils for separable reconstruction problems", *Numerical Algorithms*, 2023, (Published online June 22, 2023.)

[20] W. Van Cappellen, S. Wijnholds, and J. Bregman, "Sparse antenna array configurations in large aperture synthesis radio telescopes", in *2006 European Radar Conference*, IEEE, 2006, pp. 76–79.

[21] R. Raal, "Sub-sampled exponential analysis applied to sparse planar antenna array configurations", Ph.D. dissertation, Stellenbosch University & University of Antwerp, 2022.

[22] R. Louw, F. Knaepkens, A. Cuyt, W.-s. Lee, S. J. Wijnholds, D. de Villiers, and R.-M. Weideman, "Antenna position estimation through subsampled exponential analysis of signals in the near field", *URSI Radio Science Letters*, vol. 3, 2021.

[23] M. P. van Haarlem, M. W. Wise, A. W. Gunst, G. Heald, J. P. McKean, J. W. T. Hessels, A. G. de Bruyn, R. Nijboer, J. Swinbank, R. Fallows, *et al.*, "LOFAR: The LOw-Frequency ARray", *Astronomy & Astrophysics*, vol. 556, A2, 2013, ISSN: 1432-0746.

[24] "LOFAR." (2023), [Online]. Available: `https://www.astron.nl/telescopes/lofar`.

[25] P. Kildal, *Foundations of Antenna Engineering: A Unified Approach for Line-of-sight and Multipath*. Kildal Antenn, 2015, ISBN: 9789163785153.

[26] W. Cerfonteyn, "Impact and cause of sensitivity ripple in radio astronomy reflector antennas", Ph.D. dissertation, Stellenbosch University, 2023.

[27] D. I. L. De Villiers, "Prediction of aperture efficiency ripple in clear aperture offset gregorian antennas", *IEEE Transactions on Antennas and Propagation*, vol. 61, pp. 2457–2465, May 2013.

[28] D. G. Barnes, F. Briggs, and M. Calabretta, "Postcorrelation ripple removal and radio frequency interference rejection for parkes telescope survey data", *Radio science*, vol. 40, no. 05, pp. 1–10, 2005.

[29] R. Collin, "Aperture efficiency for paraboloidal reflectors", *IEEE Transactions on Antennas and Propagation*, vol. 32, no. 9, pp. 997–1000, 1984.

[30] A. Ludwig, "The definition of cross polarization", *IEEE Transactions on Antennas and Propagation*, vol. 21, no. 1, pp. 116–119, 1973.

[31] P.-S. Kildal, "Factorization of the feed efficiency of paraboloids and cassegrain antennas", *IEEE Transactions on Antennas and Propagation*, vol. 33, no. 8, pp. 903–908, 1985.

[32] R.-M. Weideman, A. Cuyt, and D. I. L. De Villiers, "Characterising the electric field ripple in reflector antennas using sub-sampled exponential analysis", submitted.

[33] J. Condon and S. Ransom, *Essential Radio Astronomy* (Princeton Series in Modern Observational Astronomy). Princeton University Press, 2016, ISBN: 9780691137797.

[34] R. Weideman, R. Louw, and D. I. L. de Villiers, "Practical performance of the vexpa estimation method in sparse regular arrays", in *2021 XXXIVth General Assembly and Scientific Symposium of the International Union of Radio Science (URSI GASS)*, 2021, pp. 1–4.

[35] R.-M. Weideman, R. Louw, F. Knaepkens, D. I. L. De Villiers, A. Cuyt, W.-S. Lee, and S. J. Wijnholds, "Simulated performance of antenna position estimation through sub-sampled exponential analysis", in *2022 International Conference on Electromagnetics in Advanced Applications (ICEAA)*, 2022, pp. 128–132.

[36] R.-M. Weideman, A. Cuyt, and D. I. L. De Villiers, "Characterising the frequency ripple in antenna noise temperature using exponential analysis", in *2023 International Conference on Electromagnetics in Advanced Applications (ICEAA)*, 2023.

[37] S. W. Ellingson, "Sensitivity of antenna arrays for long-wavelength radio astronomy", *IEEE Transactions on Antennas and Propagation*, vol. 59, no. 6, pp. 1855–1863, 2011.

Part I

Direction-of-Arrival Estimation with Quantised Data

Preface to Part I

The first part of this thesis is dedicated to the investigation of using VEXPA as a direction-of-arrival (DOA) estimation method in linear antenna arrays, specifically when using quantised data. In DOA estimation methods, the goal is to determine the angle from which a far-field signal is impinging on an antenna array. In [1], it was shown how VEXPA can be applied to sparse regular arrays in solving the DOA estimation problem. Sparse antenna arrays are often preferred to dense arrays because of a finer angular resolution and decreased mutual coupling.

In Chapter 1, the practical performance of VEXPA is investigated further by 1) simulating cases where the number of incoming signals is unknown, and 2) determining the effect of quantisation on the method [2]. This publication opened up the discussion on the need for an adaption of VEXPA that can accurately handle one-bit quantised data, since the analogue-to-digital converters with higher numbers of bits are more costly in practice.

The necessary adjustments to VEXPA are made to be suitable to one-bit data, and the method is discussed in Chapter 2 [3]. Different methods to estimate the number of incoming signals are also explored. The performance of one-bit VEXPA is compared to that of dense one-bit MUSIC and the sparse coprime method that makes use of a similar configuration as VEXPA.

References

[1] F. Knaepkens, A. Cuyt, W.-S. Lee, and D. I. L. de Villiers, "Regular sparse array direction of arrival estimation in one dimension", *IEEE Trans. Antennas Propag.*, vol. 68, pp. 3997–4006, 2020, (Published online January 08, 2020).

[2] R. Weideman, R. Louw, and D. I. L. de Villiers, "Practical performance of the vexpa estimation method in sparse regular arrays", in *2021 XXXIVth General Assembly and Scientific Symposium of the International Union of Radio Science (URSI GASS)*, 2021, pp. 1–4.

[3] R. Weideman, F. Knaepkens, A. Cuyt, R. Raal, and D. I. L. de Villiers, "One-bit direction-of-arrival estimation with sparse arrays", submitted.

Chapter 1

Practical Performance of the VEXPA Estimation Method in Sparse Regular Arrays

Practical performance of the VEXPA estimation method in sparse regular arrays

Rina-Mari Weideman*(1), Ridalise Louw(1) and Dirk I.L. de Villiers(1)
(1) Stellenbosch University, Stellenbosch, South Africa, 7600

Abstract

This paper presents an investigation into the practical performance of a direction of arrival (DOA) estimation method for sparse regular arrays, called VEXPA. Its ability to estimate the number of incoming signals through cluster analysis is compared to the traditional method used by dense estimation techniques. It is seen that the usefulness of the cluster analysis method depends on the underlying estimation method used by VEXPA. The effect of quantisation errors introduced by the use of an ADC is also investigated. It is found that VEXPA performs satisfactorily with one-bit data for a maximum of one signal.

1 Introduction

A common application of antenna array systems is to estimate the direction of arrival (DOA) of one or more incoming radio signals. Several well-established methods, such as MUSIC [1] and the Matrix-Pencil method [2] exist which traditionally use dense arrays. Such arrays adhere to the spatial Nyquist criterion that elements must be spaced less than a half-wavelength apart, so no ambiguity is caused in the output of their solutions, since aliasing does not occur.
A regular sub-sampling algorithm called VEXPA [3] has been formulated and successfully applied to the DOA estimation problem on sparse regular linear array examples using full-wave simulations in [4]. The elements in a sparse antenna array system are spaced more than a half-wavelength apart, which would normally lead to ambiguity in the output. The VEXPA algorithm overcomes this aliasing effect by intersecting the output of two sparse subarrays arranged in a co-prime configuration.
Sparse arrays have a number of advantages over dense arrays, including lower mutual coupling and an improved angular resolution. VEXPA introduces the possibility of solving the DOA problem in sparse regular arrays. It is used on top of a traditional Prony-like method, e.g. the Matrix-Pencil method, and includes features such as automatic detection of the number of incoming signals.
In this paper, the performance of VEXPA is investigated when practical non-idealities are present. Specifically, we investigate VEXPA's ability to correctly estimate the number of signals, as well as its performance when quantisation errors are introduced.

2 DOA Using Exponential Analysis

2.1 Dense Uniform Linear Array

With reference to Fig. 1, consider a uniform linear array (ULA) of M antenna elements receiving n signals $S_i(t)$. The output of the ULA at the mth element is the sum of the n signals, with time delays related to ϕ_i and d, the distance between antenna elements. The narrowband signals $S_i(t)$ at

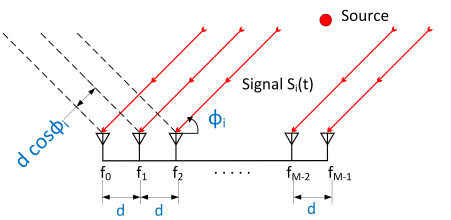

Figure 1. Illustration of a uniform linear array receiving a signal $S_i(t)$ at an angle ϕ_i.

a frequency ω and time t can be expressed as

$$S_i(t) = a_i(t)e^{jp_i(t)}e^{j\omega t} \tag{1}$$

with $a_i(t)$ and $p_i(t)$ denoting the slowly varying amplitude and phase of the signal, respectively. The source is assumed to be in the far-field of the antenna, so that $S_i(t)$ is a plane wave incident on the ULA. The time delay of incidence on consecutive antenna elements is given by

$$\tau_i = \frac{d\cos(\phi_i)}{c}, \tag{2}$$

with c equal to the propagation velocity of the signal or in free space, the speed of light. At a time t the output of the ULA at the mth element is

$$f_m(t) = \sum_{i=1}^{n} S_i(t + m\tau_i) \tag{3}$$

with n equal to the number of signals. According to the narrowband assumption, the signal does not change noticeably as it moves across the elements of the array so that

$$\begin{aligned} f_m(t) &= \sum_{i=1}^{n} S_i(t + m\tau_i) \approx \sum_{i=1}^{n} S_i(t)\exp(j\omega m\tau_i) \\ &= \sum_{i=1}^{n} S_i(t)\exp\left(\frac{j\omega md\cos\phi_i}{c}\right). \end{aligned} \tag{4}$$

Therefore, the time delay of each signal as it moves across the array leads to a phase shift that depends on the direction of the incoming angle of the signal ϕ_i. These angles can be recovered with the use of exponential analysis. At a fixed time t, the output of the ULA is called a snapshot. By introducing shorthand notations, the DOA problem is formulated as:

$$\begin{aligned} f_m &= f_m(t), & \alpha_i &= S_i(t), \\ \psi_i &= \frac{j\omega\cos\phi_i}{c}, & \Psi_i &= \exp(\psi_i d), \end{aligned} \tag{5}$$

where f_m is referred to as the samples of the exponential analysis problem, α_i are the coefficients, ψ_i the exponents and Ψ_i the base terms. Considering a single snapshot, it is possible to rewrite (4) as

$$f_m = \sum_{i=1}^{n} \alpha_i \Psi_i^m, \qquad m = 0,\ldots,M-1, \tag{6}$$

which can be solved from $2n$ samples if the base terms Ψ_i are mutually distinct and the number of signals n is known. Solutions of the base terms lead unambiguously to the directions of arrival of the signals ϕ_i.

2.2 Sparse Regular Linear Array

The VEXPA algorithm requires an antenna array consisting of two sparse ULAs in a co-prime configuration, where one is a shifted version of the other, as illustrated in Fig. 2. The

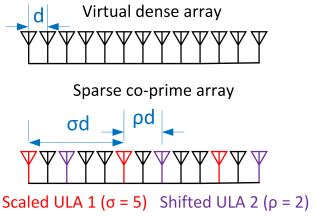

Figure 2. Layout of two sparse regular arrays in a co-prime configuration with an underlying virtual dense array.

array is configured from an underlying virtual dense ULA with antenna element spacing $d < \lambda/2$. The first sparse ULA is then found from a scale parameter σ which leads to a spacing of σd between the elements. For sparse ULA 2, a shift parameter ρ is used from which the sparse ULA 1 is shifted by a distance ρd. It is required that σ and ρ be chosen as co-prime, i.e., $\gcd(\sigma,\rho) = 1$ in order to recover from the aliasing effects of each sparse ULA. The samples from sparse ULA 1 satisfy

$$f_{m\sigma} = \sum_{i=1}^{n} \alpha_i (\Psi_i^{\sigma})^m, \quad m = 0,\ldots,M_{\sigma}-1, \tag{7}$$

from which the base terms Ψ_i^{σ} can be solved using any one-dimensional Prony-like exponential analysis method. The aliasing effect caused by the sparseness of the array can be seen by the fact that all values in the set

$$\left\{ \exp\left(\psi_i d + \frac{j2\pi}{\sigma}\ell\right) \quad : \quad \ell = 0,\ldots,\sigma-1 \right\}$$

are possible solutions to Ψ_i. The output from the second sparse ULA satisfies

$$f_{m\sigma+\rho} = \sum_{i=1}^{n} (\alpha_i \Psi_i^{\rho})(\Psi_i^{\sigma})^m, \quad m = 0,\ldots,M_{\rho}-1, \tag{8}$$

which contains the same base terms Ψ_i^{σ} as in (7). To locate the correct solution for Ψ_i, the coefficients α_i are first found from the Vandermonde structured set of linear equations using the samples $f_{m\sigma}$, after which another Vandermonde set of equations can be solved to find Ψ_i^{ρ} using the samples in (8). From the solutions Ψ_i^{ρ}, all values in the set

$$\left\{ \exp\left(\psi_i d + \frac{j2\pi}{\rho}\ell\right) \quad : \quad \ell = 0,\ldots,\rho-1 \right\}$$

are possible solutions to Ψ_i. Now, since σ and ρ were chosen to be co-prime, their intersection results in the de-aliased solution of Ψ_i. VEXPA overestimates the number of incoming signals, and repeats the underlying estimation method multiple times using different snapshots. By doing this, the true base terms will form clusters, whereas the spurious ones will be scattered. A clustering algorithm, such as DBSCAN, is used to detect the clusters and thereby determine the number of signals.

3 Estimation of the number of signals

In the previous section, we described how VEXPA makes use of cluster analysis to estimate the number of incoming signals. Traditional dense DOA estimation methods use a different approach. The covariance matrix of the output array data is decomposed into the signal and noise subspaces by using either a singular value decomposition (SVD) or eigenvalue decomposition. With the number of signals denoted as n, it is shown in [1] that only n eigenvalues rise up above the noise floor, while the others are equal to the noise variance. The number of signals can therefore be determined by subtracting the multiplicity of the smallest eigenvalue from the total number of eigenvalues.

3.1 Experimental Setup

The two methods for estimating the number of signals are compared by performing two simulations: one with VEXPA in its original form, and another with the cluster analysis step of VEXPA replaced with the eigenvalue-counting method. The latter method is incorporated by adding this step to the underlying estimation method, whereas the cluster analysis is performed on the base terms returned by the underlying method.
MATLAB is used to assemble the experimental setup, with ten elements in ULA 1 and five in ULA 2. This means a

maximum of $M_\sigma/2 = 5$ can be detected [4]. We vary the number of signals from one to four, with the respective angles of arrival at 90°, 70°, 60° and 5°, and the signal-to-noise ratio (SNR) is varied from 0 to 30 dB. We use both Root-MUSIC and the Matrix-Pencil method as underlying methods to VEXPA, and 100 Monte Carlo runs are performed. The scaling and shifting parameters are $\sigma = 11$ and $\rho = 5$.

3.2 Results

Fig. 3 shows the results from the experiment as explained above. The success rate is calculated as the percentage of the Monte Carlo runs that are successful. For a run to be considered successful, the number of signals must be estimated correctly, and the errors of the estimated angles need to be smaller than the angular resolution, given by $\Delta_\phi \approx \frac{\lambda}{D}$. D is the total length of the array in the linear case.
We see a considerable difference between the results of the different underlying methods. The main difference between using Root-MUSIC and the Matrix-Pencil method is that the latter is performed by using a single snapshot of data, whereas the former uses a subset of the total snapshots in order to estimate the covariance matrix more accurately. This means that, when Root-MUSIC is used together with the cluster analysis method, a slightly less accurate covariance matrix is used, as not all snapshots are used. This explains the slight improvement in success rate when using the eigenvalue counting method.
When using the eigenvalue counting method with the Matrix-Pencil method underlying, the results seem to worsen as the number of incoming signals are increased. On the other hand, when using the cluster analysis method, the results do not seem to depend on the number of signals to such an extent. For the cluster analysis method, the overestimation of the number of signals ensures that all possible base terms are returned, and later those that do not form clusters are discarded. For the eigenvalue method, some signals are wrongly identified as noise when their corresponding eigenvalues are too small. As the number of signals increases, it is evident that the distinction between noise eigenvalues and signal eigenvalues become vaguer.
From this, we can conclude that DOA estimation methods that are solved per snapshot can benefit from the cluster analysis method, whereas for methods using the covariance matrix, the effect of a higher number of snapshots has a more significant impact, and both the eigenvalue method and cluster analysis method are accurate.

4 Quantisation errors

In order to capture the data successfully from the antenna ports, an analogue-to-digital converter (ADC) is required. The resolution of the ADC contributes to the accuracy thereof, but as higher-resolution ADCs are more costly, low-resolution ADCs are often preferred in antenna array applications. For example, a one-bit ADC can very easily be implemented as it consists solely of a comparator. In [6]

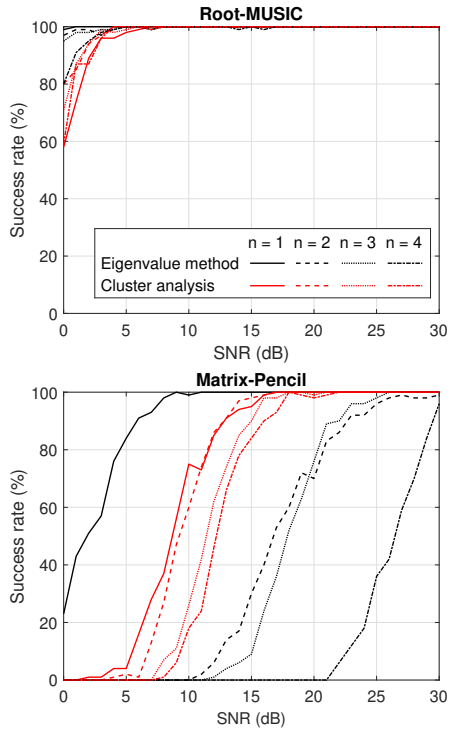

Figure 3. Success rate estimating the number of incoming signals by using two methods: identifying eigenvalues corresponding to the signal subspace (black), and using cluster analysis (red).

it was shown that MUSIC performs accurately when one-bit data is used. The question therefore arises whether VEXPA is able to do the same.

4.1 Experimental setup

Firstly we compare the performance of the two underlying methods on a dense configuration (12 elements, 0.48λ spacing). The number of signals vary from one to three and the angles of arrival are 10°, 30° and 90°. The number of bits of the ADC is varied from 1 to 8.
Next, we perform a similar experiment, but now we use VEXPA with a sparse co-prime configuration. The virtual dense spacing is 0.48λ and the scaling and shifting parameters are $\sigma = 11$ and $\rho = 5$. As before, 100 Monte Carlo runs are performed.

4.2 Results

The root-mean-square (RMS) error of Root-MUSIC and the Matrix-Pencil method with dense configurations are shown in Fig. 4. As expected from [6], we see that Root-MUSIC

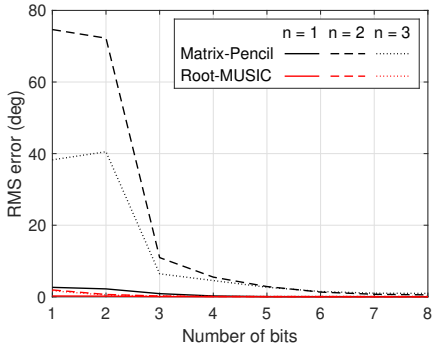

Figure 4. Performance of Matrix-Pencil and Root-MUSIC with a dense array configuration, with data quantised by ADCs of different bit sizes. Root-MUSIC performs accurately with low-resolution quantised data, whereas Matrix-Pencil has difficulty estimating the correct directions when multiple signals are present.

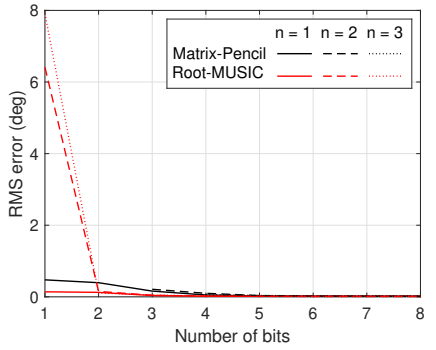

Figure 5. Performance of VEXPA (with Matrix-Pencil and Root-MUSIC underlying) with a sparse co-prime array configuration, with data quantised by ADCs of different bit sizes. Root-MUSIC performs accurately with low-resolution quantised data, whereas Matrix-Pencil does not return any DOA when multiple signals are present.

delivers small errors even when the number of ADC bits is as low as 1. On the other hand, the Matrix-Pencil method performs well with few bits only when a single signal is present.

In Fig. 5 we show the results of VEXPA with a sparse configuration using quantised data. For one incoming signal, the results are comparable to those of the dense setup in Fig. 4. For multiple signals, however, even Root-MUSIC cannot estimate the DOAs accurately with one-bit data. The Matrix-Pencil method fails to return any DOAs for multiple signals for data quantised by fewer than three bits.

The lowered accuracy at low-resolution data for the co-prime setup is introduced by the fact that the signal coefficients α_i play an important role in the formulation of the Vandermonde system in (8). As quantisation decreases the resolution of the signal amplitudes, a significant error is added to these coefficients, which negatively affects the performance of VEXPA.

We can therefore conclude that, if only low-resolution quantised data is available, the preferred underlying method for VEXPA is Root-MUSIC, although for multiple signals the performance will be compromised.

5 Conclusion

The investigation of the practical performance of VEXPA, a DOA estimation for sparse arrays, is presented. It is shown that, to estimate the number of signals, the cluster analysis method introduced by VEXPA is useful when incorporated with an underlying method that uses a single snapshot. When quantisation errors are considered, it it shown that for one signal, VEXPA performs comparably to its underlying method, but if multiple signals are present, the performance worsens.

6 Acknowledgements

This work is based on the research supported wholly by the National Research Foundation of South Africa (Grant Number: 75322).

References

[1] R. Schmidt, "Multiple emitter location and signal parameter estimation," *IEEE Transactions on Antennas and Propagation*, vol. 34, no. 3, pp. 276 - 280, March 1986.

[2] Y. Hua and T. K. Sarkar, "Matrix pencil method for estimating parameters of exponentially damped/undamped sinusoids in noise," *IEEE Transactions on Acoustics, Speech, and Signal Processing*, vol. 38, no. 5, pp. 814 - 824, May 1990.

[3] M. Briani, A. Cuyt, and W.-s. Lee, "VEXPA: Validated EXPonential Analysis through regular subsampling" arXiv e-prints, p. arXiv:1709.04281, Sep 2017.

[4] F. Knaepkens, A. Cuyt, W. Lee, and D. I. L. de Villiers, "Regular sparse array direction of arrival estimation in one dimension," *IEEE Transactions on Antennas and Propagation*, 2020.

[5] F. Sohrabi and W. Yu, "Hybrid digital and analog beamforming design for large-scale antenna arrays," *IEEE Journal of Selected Topics in Signal Processing*, vol. 10, no. 3, pp. 501 - 513, 2016.

[6] X. Huang and B. Liao, "One-Bit MUSIC," IEEE Signal Processing Letters, vol. 26, no. 7, pp. 961 - 965, 2019.

Chapter 2

One-bit Direction-of-Arrival Estimation with Sparse Arrays

One-bit Direction-of-Arrival Estimation with Sparse Arrays

Rina-Mari Weideman
Dept of Electrical & Electronic Eng.
Stellenbosch University
Stellenbosch, South Africa
18954626@sun.ac.za

Ferre Knaepkens
Dept of Mathematics
University of Antwerp
Antwerp, Belgium
ferre.knaepkens@uantwerpen.be

Annie Cuyt
Dept of Computer Science
University of Antwerp
Antwerp, Belgium
University of Stirling
Scotland, UK
Eindhoven University of Technology
Eindhoven, The Netherlands
annie.cuyt@uantwerpen.be

Ridalise Raal
Dept of Electrical & Electronic Eng.
Stellenbosch University
Stellenbosch, South Africa
17002567@sun.ac.za

Dirk de Villiers
Dept of Electrical & Electronic Eng.
Stellenbosch University
Stellenbosch, South Africa
ddv@sun.ac.za

Wen-Shin Lee
Div. of Computing Science and Mathematics
University of Stirling
Scotland, UK
wen-shin.lee@stir.ac.uk

***Abstract*—One-bit data may be used in direction-of-arrival (DOA) estimation to reduce system costs. In this paper, we present a DOA estimation method that is specifically tailored for one-bit data analysis. The method builds on the VEXPA method that uses two sparse sub-uniform linear arrays (sub-ULAs). The results show that multiple DOAs can accurately be identified by this method. It is also shown that an estimate can be found for the number of incoming signals, if the signal-to-noise ratio (SNR) is reasonable.**

I. Introduction

Sparse antenna arrays have advantages over dense arrays, such as an improved angular resolution for the same number of sensors and reduced mutual coupling. Validated EXPonential Analysis (VEXPA) is a sub-sampling exponential analysis method that was first applied to the direction-of-arrival (DOA) problem in sparse arrays in [1]. In a follow-up paper, an investigation was performed into the performance of VEXPA when practical effects, such as quantisation, are considered [2].

An important step in the data capturing process of an antenna array is the quantisation of the incoming analogue signals. This is done by an analogue-to-digital converter (ADC), with a certain number of quantisation levels [3]. Each quantisation level is represented by a binary number, which is made up of a number of bits b relating to the number of quantisation levels L by $2^b = L$. The resolution of the quantiser is then $\Delta = \frac{R}{2^b-1}$, where R is the range thereof. As higher-resolution quantisers come with the disadvantage of a higher cost and intricate circuit design [4], the use of low-resolution ADCs is desirable for antenna array applications. One-bit ADCs are especially attractive as they can be implemented by simply using a single comparator, as these return a logical value indicating whether the signal amplitude is above or below a certain threshold value. A quantiser with one bit results in $2^1 = 2$ quantisation levels. The quantisation function can be described as

$$Q(z) = \frac{1}{\sqrt{2}} \left(\text{sign}\left(\text{Re}\{z\}\right) + j\, \text{sign}\left(\text{Im}\{z\}\right) \right). \qquad (1)$$

In practice, the real component is the received signal itself, whereas the imaginary component is derived from the real part by techniques such as the Hilbert transform [5]. Hence, by (1), each complex sample is quantised to become one of the four values $\frac{1}{\sqrt{2}}(\pm 1 \ \pm 1j)$. It is noteworthy that all amplitude information is therefore lost, with only phase and frequency information remaining.

Examples of DOA estimation methods successfully applied to one-bit data include one-bit MUSIC [6], [7] and the coprime sparse array method [8]. The traditional MUSIC algorithm was adapted in [6] for one-bit data by reconstructing the unquantised covariance matrix from its quantised equivalent. However, in [7] it was shown that accurate results can be achieved without this reconstruction.

In [2], it was noted that the amplitude information is cardinal in the original implementation of VEXPA. It is therefore to be expected that the method suffers when using one-bit data. In this paper, we present an alternative implementation of VEXPA that avoids the use of the signal amplitude information, which makes it suitable for use with low resolution quantised data. When discussing this method in II, III and IV, we keep it general to both unquantised and quantised data.

II. Scale-and-shift sparse array configuration

Consider a dense uniform linear array (ULA) consisting of M_d elements, oriented along the z-axis of a Cartesian coordinate system, spaced along the x-axis. The elements are linearly polarised in the z direction. From its far-field, n uncorrelated narrowband z-polarised signals are arriving at azimuthal angles ϕ_i for $i = 1, ..., n$. The regular spacing between neighbouring elements is small enough that the spatial Nyquist criterion is satisfied, i.e., $d < \lambda/2$, where λ is the wavelength.

At a fixed time t, the sample received at element m can then be described by

$$f_m = \sum_{i=1}^{n} \alpha_i \Psi_i^m + n_m, \qquad m = 0, ..., M_d - 1. \tag{2}$$

Here, the α_i are the coefficients and n_m is the additive noise, which both consist of complex random Gaussian values. The terms Ψ_i are defined as the base terms

$$\Psi_i = \exp\left(-\frac{j\omega d \cos\phi_i}{c}\right), \tag{3}$$

where ω is the narrowband frequency in radians and c is the speed of light. For a dense array with half-wavelength spacing, these base terms simplify to

$$\Psi_i = \exp\left(j2\pi\overline{\phi_i}\right), \tag{4}$$

where $\overline{\phi_i} = 0.5\cos(\phi_i)$ is termed the normalised DOA as in [8].

VEXPA creates a sparse array configuration by placing antenna elements at a subselection of the dense array antenna positions [9]. This subselection is described by the so-called scale and shift parameters, denoted by σ and ρ, respectively. Specifically, the configuration consists of two sparse sub-ULAs. Firstly, every σth element of the dense array is chosen to describe the scaled sub-ULA, starting at element $m = 0$. The measured signal at this ULA is then described by

$$f_{m\sigma} = \sum_{i=1}^{n} \alpha_i \Psi_i^{m\sigma} + n_{m1} = \sum_{i=1}^{n} \alpha_i (\Psi_i^{\sigma})^m + n_{m1}, \qquad m = 0, ..., M_\sigma - 1. \tag{5}$$

A shifted ULA is also created by translating the elements of the scaled ULA by a distance of ρd. The samples at its output are

$$f_{m\sigma+\rho} = \sum_{i=1}^{n} \alpha_i \Psi_i^{m\sigma+\rho} + n_{m2} = \sum_{i=1}^{n} (\alpha_i \Psi_i^{\rho})(\Psi_i^{\sigma})^m + n_{m2}, \qquad m = 0, ..., M_\rho - 1. \tag{6}$$

Both the scaled and shifted arrays are therefore ULAs with interelement spacings of σd, consisting of M_σ and M_ρ elements, respectively. Fig. 1 illustrates the scale-and-shift configuration, along with that of a dense ULA and a coprime array. The scale-and-shift array is similar to the coprime array in the sense that both use a virtual dense array with two coprime parameters, but the latter applies both of these parameters as scaling factors, whereas the former applies the second as a shift parameter.

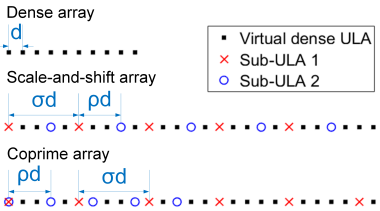

Fig. 1. Configuration of a dense array (top), scale-and-shift array (middle) and coprime array (bottom). The parameters for the sparse arrays are $\sigma = 5$, $\rho = 3$ and $M_\sigma = M_\rho = 5$.

VEXPA first solves the scaled and shifted base terms Ψ_i^σ and Ψ_i^ρ using a method specific to the relevant application. For the one-bit case, the eigenvector method is used, which is described in the next section. After these base terms are computed, the de-aliased base terms can be found by using the method described in [9]. This method requires the parameters σ and ρ to be coprime, meaning that the greatest common divisor (GCD) of the two numbers should be 1. Finally, the DOAs are determined by using (3).

III. The eigenvector method

Samples are collected from the two sub-ULAs at a fixed time t to construct the data vectors

$$\mathbf{f}_\sigma^T = \begin{bmatrix} f_0 & f_\sigma & \dots & f_{(M_\sigma-1)\sigma} \end{bmatrix}. \tag{7}$$

and

$$\mathbf{f}_\rho^T = \begin{bmatrix} f_\rho & f_{\sigma+\rho} & \dots & f_{(M_\rho-1)\sigma+\rho} \end{bmatrix}. \tag{8}$$

In the case of the eigenvector method, the number of antenna elements in the two sub-ULAs are equal, i.e., $M_\sigma = M_\rho$. The total number of elements is denoted as $M = M_\sigma + M_\rho$. The maximum number of signals that can be identified is $n_{\max} = M_\sigma = M_\rho$.

The concatenated data vector of the full array can be expressed as

$$\mathbf{f} = \begin{bmatrix} \mathbf{f}_\sigma \\ \mathbf{f}_\rho \end{bmatrix} = V\boldsymbol{\alpha} + \mathbf{n}, \tag{9}$$

where

$$V = \begin{bmatrix} V_\sigma \\ V_\sigma D_\rho \end{bmatrix}, \tag{10}$$

with

$$V_\sigma = \begin{bmatrix} 1 & 1 & \dots & 1 \\ \Psi_1^\sigma & \Psi_2^\sigma & \dots & \Psi_n^\sigma \\ \vdots & \vdots & \ddots & \vdots \\ \Psi_1^{(M_\sigma-1)\sigma} & \Psi_2^{(M_\sigma-1)\sigma} & \dots & \Psi_n^{(M_\sigma-1)\sigma} \end{bmatrix} \tag{11}$$

and

$$D_\rho = \text{diag}\left[\Psi_1^\rho \quad \cdots \quad \Psi_n^\rho\right]. \tag{12}$$

The signal vector $\boldsymbol{\alpha}$ consists of the coefficients $\alpha_i,\ i = 1, ..., n$. The noise vector $\mathbf{n}$ has size $M \times 1$.

As with most subspace-based DOA methods, we first express the covariance matrix of the received signal as

$$\begin{aligned} R &= E[\mathbf{f}\ \mathbf{f}^H] \\ &= VE[\boldsymbol{\alpha}\ \boldsymbol{\alpha}^H]V^H + E[\mathbf{n}\ \mathbf{n}^H] \\ &= VR_{ss}V^H + p_nI, \end{aligned} \tag{13}$$

where R_{ss} represents the signal covariance matrix and p_n the noise power [10]. The statistical expectation $E[\ .\ ]$ can be approximated by using the temporal average of the antenna samples. The data vector $\mathbf{f}$ is therefore collected at K different snapshots, denoted as $\mathbf{f}(t_k)^T = [\mathbf{f}_\sigma(t_k)^T\ \mathbf{f}_\rho(t_k)^T]$ for $k = 1, ..., K$. The approximated covariance matrix is then computed as

$$R \approx \frac{1}{K}\sum_{k=1}^{K}\mathbf{f}(t_k)\mathbf{f}^H(t_k). \tag{14}$$

A singular value decomposition (SVD) is performed on the covariance matrix to give

$$R = U\Sigma W^H. \tag{15}$$

Assuming the number of signals n is known, we can define the signal subspace U_S and noise subspace U_N by splitting the matrix of singular vectors U as

$$U = [U_S\ U_N], \tag{16}$$

where U_S is of size $M \times n$, containing the eigenvectors corresponding to the n largest singular values. Similarly, U_N consists of the $M-n$ eigenvectors corresponding to the smaller singular values.

If the incoming signals are incoherent, the columns of V and U_S span the same subspace. This means that a nonsingular matrix T exists such that

$$U_S = VT. \tag{17}$$

Separating U_S into two matrices corresponding to the two sub-ULAs leads to

$$U_S = \begin{bmatrix} U_\sigma \\ U_\rho \end{bmatrix} = \begin{bmatrix} V_\sigma T \\ V_\sigma D_\rho T \end{bmatrix}. \tag{18}$$

An $n \times n$ nonsingular matrix can be defined to map the signal subspace of the one sub-ULA to that of the other [11]:

$$\begin{aligned} U_\sigma\Lambda &= U_\rho \\ V_\sigma T\Lambda &= V_\sigma D_\rho T, \end{aligned} \tag{19}$$

from which it follows that

$$V_\sigma T\Lambda T^{-1} = V_\sigma D_\rho. \tag{20}$$

Assuming that V_σ is full rank, the equation above leads to

$$T\Lambda T^{-1} = D_\rho. \tag{21}$$

The equation above takes the form of a similarity transformation, which means that the diagonal elements of D_ρ are the eigenvalues of Λ [10]. The shifted base terms Ψ_i^ρ for $i = 1, ..., n$ are therefore computed by finding the eigenvalues of the matrix Λ, which is formed by solving the top equation in (19) in a least-squares sense.

To find the scaled base terms Ψ_i^σ, we first note that the matrix $U_\sigma T^{-1}$ consists of the properly normalised right eigenvectors of Λ. This means that

$$U_\sigma T^{-1} = V_\sigma, \tag{22}$$

implicating that the multiplication of the matrix U_σ with the properly normalised right eigenvectors of Λ delivers the matrix V_σ containing the information on the scaled base terms. Specifically, we can find $M_\sigma - 1$ estimates for each Ψ_i^σ by the element-wise division

$$\frac{(V_\sigma)_{j+1,i}}{(V_\sigma)_{j,i}}, \qquad j = 0, 1, ..., M_\sigma - 2. \tag{23}$$

A final value for each Ψ_i^σ is found by taking the mean of the $M_\sigma - 1$ solutions. At this point, the normalisation of the matrix V_σ is no longer important, as the base terms result from the ratios in (23). Since the largest possible size of both U_σ and U_ρ is $M_\sigma \times M_\sigma$, the maximum number of columns in V_σ is M_σ, which means the maximum number of detectable incoming sources is $n_{\max} = M_\sigma = M_\rho$.

It is clear that, by using this method, we get solutions for Ψ_i^σ and Ψ_i^ρ while avoiding the need of an accurate computation of the coefficients α_i, which is impractical when one-bit data are used.

IV. Estimating the number of signals

It is often the case that the number of incoming signals is unknown. In these cases, traditional DOA methods use the structure of the eigenvalue or singular value decomposition to find an estimation of the number of signals. The singular values, found as the diagonal entries of the matrix Σ in (15), are used. Since the rank of the data matrix is equal to the number of terms n, only n of the singular values are non-zero [10]. When working with noisy data, the $M - n$ singular values that correspond to the noise subspace will, however, not be exactly zero but still significantly smaller than the signal singular values. The number of terms can therefore be estimated by inspecting the ratio of each singular value to the maximum singular value, i.e., $s_i/s_{\max}$. A threshold p is chosen for this singular value to be regarded as a noise singular value. The estimated number of terms is then the number of singular values for which

$$\frac{s_i}{s_{\max}} \geq p \tag{24}$$

is true [12]. The parameter p can be chosen according to the noise level of the data, but this is a subjective process and is therefore not ideal.

In [13], a method is presented that requires no subjective judgment. Specifically, the number of signals is estimated as

the value for which the Minimum Description Length (MDL) criterion is minimised. The MDL criterion is given by

$$\text{MDL}(k) = -\log\left(\frac{\prod_{i=k+1}^{M} s_i^{1/(M-k)}}{\frac{1}{M-k}\sum_{i=k+1}^{M} s_i}\right)^{(M-k)K} + \frac{1}{2}k(2M-k)\log K, \qquad k = 1, ..., M, \quad (25)$$

where $s_1 > s_2 ... > s_M$, M and K are the singular values, number of antennas and number of snapshots, respectively. The estimation for the number of signals is then determined as the value of k between 1 and M that minimises (25).

The VEXPA method avoids using the singular values, and rather uses cluster analysis to estimate the number of signals. To do this, the K total snapshots are divided into K_s subsets of snapshots, each containing K_t snapshots. These subsets are selected at random. The value K_t should be smaller than K, but since the covariance matrix is estimated by taking the temporal average of the antenna samples, it should also be sufficiently large. An example of a good choice is $K_t = 0.5K$. The eigenvector method is then performed a total of K_s times, with each execution using data of a different subset. With each run, the number of signals is assumed to be the maximum possible value, i.e., M_σ. This means M_σ results are delivered for both Ψ_i^σ and Ψ_i^ρ with each run. A total number of $K_s \times M_\sigma$ solutions are therefore collected for each base term.

Because of the random noise, only the n true solutions will cluster around the same position for each run, whereas the $M_\sigma - n$ noisy or spurious base terms will be dispersed randomly [9]. The number of signals therefore equals the number of clusters formed by the solutions of Ψ_i^σ and Ψ_i^ρ.

A well-known cluster analysis algorithm that is often incorporated by VEXPA is Density-Based Spatial clustering of Applications with Noise (DBSCAN) [14]. This algorithm identifies clusters by using two parameters: m_δ and δ, where the first indicates the minimum number of points required in the neighbourhood of a specific point for that point to be recorded as the core point of a cluster, and the latter represents the maximum distance between two points for them to be considered neighbours.

In the case of quantised data, the clusters do not appear in such a predictable manner as when using unquantised data. This makes it difficult to choose the DBSCAN parameters. For this reason, we take a slightly different approach. For the solutions of both Ψ_i^σ and Ψ_i^ρ, we find a total of M_σ clusters. This is done by firstly searching for the densest point among the possible K_s points. The densest point has a specified minimum number of points m_δ around it within the smallest possible radius. This point is identified by calculating the Euclidean distance between all possible pairs of points, and finding the point for which the distance to the m_δth closest point is the smallest. After the first cluster has been found, the points contributing to this cluster are removed and the process is repeated $M_\sigma - 1$ times. This method avoids defining the radius parameter δ. The parameter m_δ is slightly larger for the Ψ_i^ρ cluster identification than that of Ψ_i^σ, since the scaled base terms are computed as the eigenvectors of the generalised eigenvalue problem, which is less accurate than the eigenvalues, which give the solutions for the shifted base terms.

A last step is to discard the clusters that are significantly larger than the others. Specifically, this is done by computing the ratio of the radius of each cluster with the radius of the smallest cluster, and subsequently discarding the clusters for which this ratio is larger than a threshold τ. Through empirical evaluation, this threshold is chosen as $\tau = 3$.

Finally, the number of incoming signals is estimated as the number of validated clusters, and the final value for both Ψ_i^σ and Ψ_i^ρ are determined as the centroid of each cluster.

The method is summarised in Algorithm 1.

V. Results

We consider a dense ULA with an inter-element spacing of $d = \lambda/2$ and $M = 12$ elements. A scale-and-shift array with the same number of elements has a virtual dense spacing d and parameters $\sigma = 11$ and $\rho = 5$. Each sub-ULA has $M_\sigma = M_\rho = M/2 = 6$ elements. We also consider a standard coprime sparse array with the same parameters. The performance of VEXPA is compared to the coprime method [8] and dense one-bit MUSIC [7].

The number of incoming signals is varied as $n = 2$, $n = 4$ and $n = 5$. The respective angles of arrival are $10°$, $90°$, $30°$, $120°$ and $135°$, with the normalised DOA defined as $\overline{\phi_i} = 0.5\cos(\phi_i)$. The coefficients $\alpha_i(t_k)$ for $i = 1, ..., n$ and $k = 1, ..., K$ are complex Gaussian random values. The received samples are quantised to one-bit data by using (1).

Firstly we vary the signal-to-noise ratio (SNR) from -10 dB to 30 dB, while the number of snapshots stays constant at $K = 2^8 = 256$. It is assumed that the number of incoming signals n is known, which means that DBSCAN is not needed and all the snapshots are used to calculate a single covariance matrix. A total of 100 Monte Carlo runs are executed.

The results are shown in Fig. 2, with the vertical axis indicating the mean-squared error (MSE), which is defined as $\text{MSE} = \sum_{i=1}^{n}(\hat{\overline{\phi_i}} - \overline{\phi_i})^2/n$, where $\hat{\overline{\phi_i}}$ is the estimation of the normalised DOA. It is clear that VEXPA performs very well, especially for an SNR value of 0 or higher, where the error is smaller than that of both dense MUSIC and the coprime method.

Next, an experiment is performed where the SNR stays constant at SNR $= 0$ dB, with the number of snapshots increasing in powers of two, i.e., $K = 2^p$ with $p = 5, 6, ..., 10$. In Fig. 3 we see that the MSE decreases as the snapshots increase, which is to be expected. The performance of the three methods is comparable, with VEXPA delivering results of up to an order of magnitude better when more snapshots are available.

To evaluate the different methods estimating the number of incoming signals, we keep the same experimental setup but do not specify the parameter n. Once again, the number of snapshots remains constant at $K = 256$ while the SNR value

Algorithm 1 One-bit Sparse DOA Estimation

At K different timestamps t_k, $k = 1, ..., K$, collect M antenna samples $\mathbf{f}(t_k)$ from the scale-and-shift configuration.
Set m_{δ_σ}, m_{δ_ρ} and $K_s = K_t = 0.5K$.
for $j = 1$ to K_s **do**
    Select a random subset of K_t snapshots from the total K snapshots.
    Compute the covariance matrix R using (14), where k now assumes the K_t values of the chosen subset in the previous step.
    Compute the SVD as $[U, S, W] = \text{SVD}(R)$.
    Separate the matrix U into U_σ and U_ρ, containing the first and last M_σ rows of U, respectively.
    Find the matrix Λ by solving the top equation in (19) in a least squares sense.
    Find M_σ solutions for Ψ_i^ρ by computing the eigenvalues of Λ.
    Compute the matrix V_σ by using U_σ and the normalised right eigenvectors of Λ in the multiplication in (22).
    Find M_σ solutions for Ψ_i^σ by taking the mean of the division in (23).
end for
for $m = 1$ to M_σ **do**
    From the $K_s M_\rho$ available solutions for the Ψ_i^ρ values, find the m_{δ_ρ} ones that form the densest cluster. Take the mean of these points to find the final solution for Ψ_m^ρ.
    From the $K_s M_\sigma$ available solutions for the Ψ_i^σ values, find the m_{δ_σ} ones that form the densest cluster. Take the mean of these points to find the final solution for Ψ_m^σ.
    Remove the solutions found in the two previous steps from the total set of solutions and decrease $K_s M_\rho$ and $K_s M_\sigma$, respectively.
end for
For Ψ_i^ρ, discard the clusters for which the radius is at least $\tau = 3$ times larger than the radius of the smallest cluster. The number of remaining clusters is the final estimation of the number of signals n.
Use the de-aliasing method in [9] to solve for Ψ_i from Ψ_i^σ and Ψ_i^ρ for $i = 1, ..., n$.
Use (3) to find the DOAs ϕ_i for $i = 1, ..., n$.

is varied. The threshold in (24) is chosen as $p = 0.4$. A total of 1000 Monte Carlo runs are performed and the success rate is defined as the percentage of these runs that result in an accurate estimation of the number of signals. The number of runs is set higher than the previous experiments because of the anomalous behaviour of some of the results, which are shown in Fig. 4.

We see that for SNR values of 10 dB and higher, VEXPA in conjunction with DBSCAN delivers a success rate of 84% or higher for all three cases of incoming signals. When using the MDL criterion with the covariance singular values, a very high success rate is obtained when $n = 5$, but the results are less promising for $n = 2$ and $n = 4$. For these cases, the number of signals is successfully identified at SNR $= 0$ dB, but the success rate does not rise far above 0% for the other SNR values. When investigating the estimated number of signals returned by the MDL method, it is seen that the estimate increases with the SNR. At SNR = 0 dB, an accurate estimation is found, but at higher values the method overestimates the number of signals and fails to return an accurate result.

The method using the threshold as in (24) delivers a 100% success rate for all cases when the SNR value is at 0 dB or above. Here it should be mentioned that the threshold was chosen specifically to be conducive to the estimation. In practice, it is a difficult task to choose an appropriate threshold.

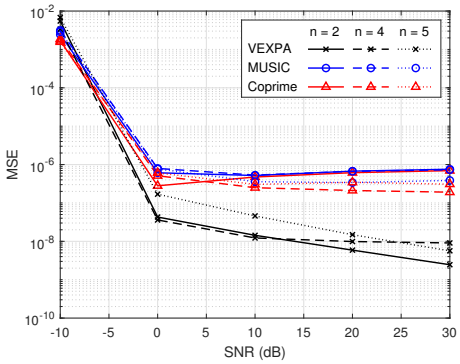

Fig. 2. The performance of VEXPA, one-bit dense MUSIC and the coprime method on one-bit quantised data for $n = 2$, $n = 4$ and $n = 5$ incoming signals. Each point is averaged from 100 Monte Carlo runs.

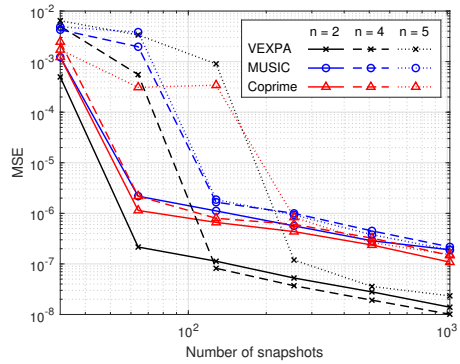

Fig. 3. The performance of VEXPA, one-bit dense MUSIC and the coprime method on one-bit quantised data for $n = 2$, $n = 4$ and $n = 5$ incoming signals. Each point is averaged from 100 Monte Carlo runs.

Part II

Antenna Position Estimation

Preface to Part II

The next application we explore is the antenna position estimation problem. In large irregular arrays, faults can easily happen where the cable of one antenna is connected to the receiver of another, and it is therefore helpful to have accurate knowledge of the antenna positions. This problem is essentially the inverse of the direction-of-arrival estimation problem, where we now know the direction of the incoming signal and want to estimate the position of the antennas on the ground. The known source in the sky, from an unmanned aerial vehicle (UAV), is in the near-field of the antenna array and therefore the necessary adaptions to VEXPA need to be made.

In Chapter 3, the method is described, explaining how a linearisation step is used to account for the near-field case [1]. A simulation is performed on synthetic data considering the LOFAR low band antenna (LBA) array [2] to show that the method works.

Next, the practical effect of mutual coupling is considered in Chapter 4, by making use of a simulated experiment in the full-wave solver FEKO [4], [3]. It is shown how the effect of mutual coupling changes as the antenna elements are moved closer and further away from one another.

References

[1] R. Louw, F. Knaepkens, A. Cuyt, W.-S. Lee, S. J. Wijnholds, D. I. L. de Villiers, and R.-M. Weideman, "Antenna position estimation through sub-sampled exponential analysis of signals in the near-field", *Radio Science Letters*, vol. 3, 2021.

[2] "LOFAR." (2023), [Online]. Available: `https://www.astron.nl/telescopes/lofar`.

[3] "Altair Development S.A. (Pty) Ltd, Stellenbosch, South Africa. FEKO 2021.2." (2021), [Online]. Available: `https://altairhyperworks.com/feko/`.

[4] R.-M. Weideman, R. Louw, F. Knaepkens, D. I. L. De Villiers, A. Cuyt, W.-S Lee, and S. J. Wijnholds, "Simulated performance of antenna position estimation through sub-sampled exponential analysis", in *2022 International Conference on Electromagnetics in Advanced Applications (ICEAA)*, 2022, pp. 128–132.

Chapter 3

Antenna Position Estimation Through Sub-Sampled Exponential Analysis of Signals in the Near-Field

Antenna Position Estimation Through Subsampled Exponential Analysis of Signals in the Near Field

Ridalise Louw, Ferre Knaepkens, Annie Cuyt, Wen-shin Lee, Stefan J. Wijnholds, Dirk I. L. de Villiers, and Rina-Mari Weideman

Abstract – In a previous article we explored the use of a subsampled exponential analysis algorithm to find the antenna-element positions in a large irregular planar array after the installation phase. The application requires an unmanned aerial vehicle to be flown over the antenna array while transmitting several odd harmonic signals. The received signal samples at a chosen reference antenna element are then compared to those at every other element in the array in order to find its position. Previously, the far-field approximation was used to calculate the time delay between received signals. In this article the method is reconsidered for the more realistic case of when the source is in the near field of the array. A number of problems that arise are addressed, and results from a controlled simulation are presented to illustrate that the computational method works.

1. Introduction

Ensuring accurate placement of the antenna elements in large-N radio interferometers like the Low Frequency Array (LOFAR) [1] and the Square Kilometre Array [2] is a costly and time-consuming process. Methods for finding the positions of individual antenna elements within an irregular array after the installation phase have been proposed [3, 4] in which signals are transmitted from an unmanned aerial vehicle (UAV) toward the array. This saves time and money by allowing for errors from the designed positions during placement of the elements, as well as indicating which elements are connected incorrectly to the back end. The application of a subsampled exponential analysis algorithm using the far-field approximation was presented in [4]. Here the method is extended for when the UAV is in the near field of the array.

Manuscript received 28 December 2021.

Ridalise Louw, Dirk de Villiers, and Rina-Mari Weideman are with the Department of Electrical and Electronic Engineering, Stellenbosch University, Cnr Banghoek Road & Joubert Street, Stellenbosch, 7600, South Africa; e-mail: 17002567@sun.ac.za, ddv@sun.ac.za, 18954626@sun.ac.za.

Ferre Knaepkens is with the Department of Computer Science, University of Antwerp, Middelheimlaan 1, 2020 Antwerpen, Belgium; e-mail: ferre.knaepkens@uantwerpen.be.

Annie Cuyt is with the Department of Computer Science, University of Antwerp, Middelheimlaan 1, 2020 Antwerpen, Belgium, and the College of Mathematics and Statistics, Shenzhen University, Shenzhen, Guangdong 518060, China; e-mail: annie.cuyt@uantwerpen.be.

Wen-shin Lee is with the Division of Computing Science and Mathematics, University of Stirling, Stirling FK9 4LA, Scotland (UK), and the Department of Computer Science, University of Antwerp, Middelheimlaan 1, 2020 Antwerpen, Belgium; e-mail: wen-shin.lee@stir.ac.uk.

Stefan Wijnholds is with the Netherlands Institute for Radio Astronomy (ASTRON), Dwingeloo, The Netherlands, and the Department of Electrical and Electronic Engineering, Stellenbosch University, Stellenbosch 7600, South Africa; e-mail: wijnholds@astron.nl.

2. Problem Formulation

Figure 1 illustrates narrowband odd harmonic signals $S_i(t_p)$ transmitted from the UAV when it is located at position $\mathbf{r}_p$ at time t_p. The index $i \in \mathbb{N}$ distinguishes between frequencies $\omega_i = (2i + 1)\omega_0$, where ω_0 is the baseband frequency. At time t_p, the signals are expressed as

$$S_i(t_p) = s_i(t_p) \exp(j\omega_i t_p) \tag{1}$$

where $s_i(t_p)$ is assumed to remain constant during the measurement of $S_i(t_p)$. As in [3, 4], we assume the signals are strong enough that astronomical sources in the field of view of the array can be ignored. With the UAV in the radiating near field of the antenna, a curved phase front is incident on the array.

A reference antenna element $\mathbf{a}_1 = (0, 0, 0)$ is chosen to coincide with the origin. All elements are assumed to be located in the (x, y)-plane, so their z-coordinates are zero. In the near field, the time delay of incidence on the mth antenna element at position $\mathbf{a}_m = u_m\mathbf{x} + v_m\mathbf{y} + (0)\mathbf{z}$ relative to $\mathbf{a}_1$ at time t_p is

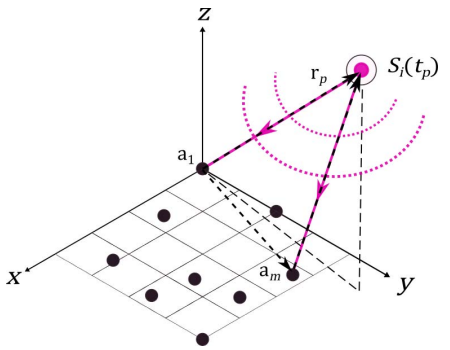

Figure 1. The UAV transmits signals $S_i(t_p)$ at time t_p while in the near field of the planar array.

$$\tau_m(x_p,y_p,z_p) = \frac{\|\mathbf{r}_p\| - \|\mathbf{r}_p - \mathbf{a}_m\|}{c} = \frac{r_p - \sqrt{r_p^2 + u_m^2 + v_m^2 - 2(u_m x_p + v_m y_p)}}{c} \tag{2}$$

where $\mathbf{r}_p = x_p\mathbf{x} + y_p\mathbf{y} + z_p\mathbf{z}$ is the vector from the origin to the UAV's position, $r_p = \|\mathbf{r}_p\|$, $\mathbf{r}_p - \mathbf{a}_m$ is the vector from the mth antenna element to the UAV, and c is the propagation velocity of the signal, or the speed of light in free space. From the narrowband assumption, the samples at the mth element at time t_p for frequency i are

$$f_{mi}(t_p) = S_i(t_p + \tau_m(x_p,y_p,z_p)) \approx s_i(t_p)\exp(j\omega_i t_p)\exp(j\omega_i \tau_m(x_p,y_p,z_p)) \tag{3}$$

To extract the positions $(u_m, v_m, 0)$, we need multiple samples at time t_p, and this from several positions $\mathbf{r}_p$, with $p = 1, \ldots, P$ [5]. We use the following shorthand notations for a fixed UAV position $\mathbf{r}_p$:

$$\begin{aligned} f_{mip} &= f_{mi}(t_p),\\ \alpha_{ip} &= s_i(t_p)\exp(j\omega_i t_p),\\ \Delta_{mp} &= u_m^2 + v_m^2 - 2(u_m x_p + v_m y_p),\\ \tau_{mp} &= \tau_m(x_p,y_p,z_p) = \frac{1}{c}\left(r_p - \sqrt{r_p^2 + \Delta_{mp}}\right),\\ \Psi_{mp} &= j\omega_0\tau_{mp} \text{ so that } (2i+1)\Psi_{mp} = j\omega_i\tau_{mp} \end{aligned} \tag{4}$$

The samples at each element m are filtered into subbands, so for position p,

$$f_{mip} = \alpha_{ip}\exp((2i+1)\Psi_{mp}) \tag{5}$$

The frequency and positional dependence of the coefficients α_{ip} are undesirable. Therefore, we first divide the sample sets f_{mip} by the reference antenna element's samples $f_{1ip} = s_i(t_p)\exp(j\omega_i t_p)\exp(0) = \alpha_{ip}$, which gives

$$f'_{mip} = \frac{f_{mip}}{f_{1ip}} = \exp((2i+1)\Psi_{mp}) \tag{6}$$

3. Subsampled Exponential Analysis

To ensure that no aliasing occurs, we need $|2\Psi_{mp}| < \pi$, which leads to the spatial Nyquist criterion

$$\left|2\left(r_p - \sqrt{r_p^2 + \Delta_{mp}}\right)\right| < \frac{\lambda_0}{2} \tag{7}$$

where λ_0 is the wavelength of ω_0. In the dense case where (7) holds, the base terms Ψ_{mp} can be recovered from the signal samples by using any Prony-like method. If (7) is not satisfied, we have a subsampled exponential analysis problem that we can solve with a technique similar to [6, 7]. This dealiasing method works with coprime scale parameters σ_1 and σ_2 and can also be used in the multivariate case [5]. The equations for the near-field base terms Ψ_{mp} in (4) are nonlinear, so in order to recover from aliasing using this approach, we first linearize our model with a first-order Taylor-series partial sum.

4. Linearization of the Near-Field Model

While u_m and v_m denote the coordinates of antenna element $\mathbf{a}_m$ in the (x,y)-plane and (x_p, y_p, z_p) denotes the location of the UAV in space at time t_p, we introduce the general coordinates u and v in the plane. During the linearization, we keep $\mathbf{r}_p = x_p\mathbf{x} + y_p\mathbf{y} + z_p\mathbf{z}$ at time t_p fixed, so that the expression

$$g_p(u,v) = \|\mathbf{r}_p\| - \sqrt{\|\mathbf{r}_p\|^2 + \Delta_p(u,v)},\qquad \Delta_p(u,v) = u^2 + v^2 - 2(ux_p + vy_p)$$

varies only with the planar position (u, v). We approximate $g_p(u, v)$ by

$$L_p(u,v) = g_p(\tilde{u},\tilde{v}) + (u-\tilde{u})g_p^{(u)}(\tilde{u},\tilde{v}) + (v-\tilde{v})g_p^{(v)}(\tilde{u},\tilde{v}) \tag{8}$$

where $g_p^{(u)}$ and $g_p^{(v)}$ are the partial derivatives with respect to u and v,

$$g_p^{(u)}(u,v) = \frac{x_p - u}{\sqrt{\|\mathbf{r}_p\|^2 + \Delta_p(u,v)}},\qquad g_p^{(v)}(u,v) = \frac{y_p - v}{\sqrt{\|\mathbf{r}_p\|^2 + \Delta_p(u,v)}} \tag{9}$$

Substituting these equations into (8), the linearized approximation $L_p(u, v)$ becomes

$$L_p(u,v) = r_p - \sqrt{r_p^2 + \Delta_p(\tilde{u},\tilde{v})} + \frac{(u-\tilde{u})(x_p-\tilde{u})}{\sqrt{r_p^2 + \Delta_p(\tilde{u},\tilde{v})}} + \frac{(v-\tilde{v})(y_p-\tilde{v})}{\sqrt{r_p^2 + \Delta_p(\tilde{u},\tilde{v})}} \tag{10}$$

Let the constant terms in (10), for a certain estimation $(\tilde{u},\tilde{v})$, be denoted by

$$\kappa_p(\tilde{u},\tilde{v}) = r_p - \sqrt{r_p^2 + \Delta_p(\tilde{u},\tilde{v})} - \frac{\tilde{u}(x_p-\tilde{u}) + \tilde{v}(y_p-\tilde{v})}{\sqrt{r_p^2 + \Delta_p(\tilde{u},\tilde{v})}} \tag{11}$$

Then we can use the remaining function

$$L_p(u,v) - \kappa_p(\tilde{u},\tilde{v}) = \frac{u(x_p-\tilde{u}) + v(y_p-\tilde{v})}{\sqrt{r_p^2 + \Delta_p(\tilde{u},\tilde{v})}} \tag{12}$$

to solve the positions of the elements in the antenna array in the near-field sub-Nyquist case, where the common factor $1\Big/\sqrt{r_p^2 + \Delta_p(\tilde{u},\tilde{v})}$ can be used to model σ_j, $j = 1, 2$, as explained in the next section.

5. Exponential Analysis of the Linearized Near-Field Problem

Choose $2P$ radial positions $\mathbf{r}_{p_j} = x_p\mathbf{x} + y_p\mathbf{y} + z_{p_j}\mathbf{z}$ with radial distance $r_{p_j} = \|\mathbf{r}_{p_j}\|$, for $j = 1, 2$ and $p = 1, \ldots, P$. Let $\tilde{u}_m$ and $\tilde{v}_m$ be estimates of the coordinates u_m and v_m in the (x, y)-plane of antenna $\mathbf{a}_m$, and let us denote $\tilde{\Delta}_{mp} = \Delta_p(\tilde{u}_m, \tilde{v}_m)$ and $\kappa_{mp_j} = \kappa_{p_j}(\tilde{u}_m, \tilde{v}_m)$. Note that $\tilde{\Delta}_{mp}$ is independent of the z-coordinate and therefore simply indexed by p, not p_j. With p and m fixed, the linearization

$$L_{p_j}(u_m, v_m) - \kappa_{mp_j} = \frac{u_m(x_p - \tilde{u}_m) + v_m(y_p - \tilde{v}_m)}{\sqrt{r_{p_j}^2 + \tilde{\Delta}_{mp}}} \tag{13}$$

is used to model the near-field nonlinear

$$g_{p_j}(u_m, v_m) = r_{p_j} - \sqrt{r_{p_j}^2 + \Delta_{mp}} \approx L_{p_j}(u_m, v_m) \tag{14}$$

The approximation in the right-hand side of (14) becomes more accurate as the value of $(\tilde{u}_m, \tilde{v}_m)$ gets closer to the true antenna element position (u_m, v_m). We additionally introduce the virtual UAV position $\mathbf{R}_p = x_p\mathbf{x} + y_p\mathbf{y} + Z_p\mathbf{z}$ with virtual height Z_p and $R_p = \|\mathbf{R}_p\|$, such that the spatial Nyquist criterion

$$\left|2\left(R_p - \sqrt{R_p^2 + \Delta_{mp}}\right)\right| < \frac{\lambda_0}{2} \tag{15}$$

is met for all m. With R_p, we rewrite the value C_{mp_j} as a scaled C_{mp},

$$\begin{aligned} C_{mp_j} &= \frac{1}{\sqrt{r_{p_j}^2 + \tilde{\Delta}_{mp}}} = \sigma_{jmp} C_{mp}, \\ C_{mp} &= \frac{1}{\sqrt{R_p^2 + \tilde{\Delta}_{mp}}} \end{aligned} \tag{16}$$

and we start the iterative improvement of the estimation $(\tilde{u}_m, \tilde{v}_m)$. During the iteration, the values of r_{p_j} remain constant while $\tilde{\Delta}_{mp}$ is updated at every iteration step. The values of σ_{jmp} and R_p are manipulated in every iteration step to give (16), with the only restrictions being that the spatial Nyquist criterion in (15) must be met and σ_{jmp}, $j = 1, 2$ must be coprime in order to recover from aliasing. If we set $r_{p_1} > r_{p_2}$, then $C_{mp_2} > C_{mp_1}$ for all m. The ratios

$$\frac{\sigma_{2mp}}{\sigma_{1mp}} = \frac{C_{mp_2}}{C_{mp_1}} \tag{17}$$

rounded to two significant digits provide coprime values for σ_{1mp} and σ_{2mp}. For each antenna, we start with $\tilde{u}_m = \tilde{v}_m = 0$ so that $\tilde{\Delta}_{mp} = 0$ and $\kappa_{mp} = 0$. A new value of the estimated antenna position $(\tilde{u}_m, \tilde{v}_m)$ is found as follows, using our approximated model in conjunction with the subsampled exponential algorithm.

The samples at each antenna element normalized by f_{1ip_j} according to (6) are

$$f'_{mip_j} = \exp\left((2i+1)j\frac{\omega_0}{c}\left(r_{p_j} - \sqrt{r_{p_j}^2 + \Delta_{mp}}\right)\right) \tag{18}$$

Thus, a priori we compute the base terms

$$\exp\left(2j\frac{\omega_0}{c}\left(r_{p_j} - \sqrt{r_{p_j}^2 + \Delta_{mp}}\right)\right) \tag{19}$$

using any Prony-like method for the samples f'_{mip_j}. Here we prefer the Root-MUSIC algorithm [8] because of its accuracy. For every antenna element $\mathbf{a}_m$, every position p, and every j we use N_t time samples of the form in (18), with added white Gaussian noise from systematic effects in the antenna array's channels. Fortunately, the noise encourages clustering in the complex plane around the true solution of the base terms in (19) [6]. We use the densest point from all evaluations as our best estimate of (19), which is defined as the point inside the smallest possible radius that contains a specified minimum number of points around it.

Subsequently, in every iteration step the estimated base terms are shifted by multiplying them with $\exp\left(-j\frac{2\omega_0}{c}\kappa_{mp_j}\right)$. Since $\Delta_{mp} \approx \tilde{\Delta}_{mp}$, we find that

$$g_{p_j}(u_m, v_m) = r_{p_j} - \sqrt{r_{p_j}^2 + \Delta_{mp}} \approx r_{p_j} - \sqrt{r_{p_j}^2 + \tilde{\Delta}_{mp}}$$

and hence that the linearization in (13) can be used. Moreover,

$$\begin{aligned} &j\frac{2\omega_0}{c}\left(r_{p_j} - \sqrt{r_{p_j}^2 + \Delta_{mp}} - \kappa_{mp_j}\right) \\ &\quad\approx j\frac{2\omega_0}{c}\left(\frac{u_m(x_p - \tilde{u}_m) + v_m(y_p - \tilde{v}_m)}{\sqrt{r_{p_j}^2 + \tilde{\Delta}_{mp}}}\right) \\ &\quad= j\frac{2\sigma_{jmp}\omega_0}{c}\left(\frac{u_m(x_p - \tilde{u}_m) + v_m(y_p - \tilde{v}_m)}{\sqrt{R_p^2 + \tilde{\Delta}_{mp}}}\right) \end{aligned} \tag{20}$$

We can therefore denote the left-hand side of (20) by $\sigma_{jmp}\Phi_{mp}$. The possible arguments Φ_{mp} of $\exp(\sigma_{jmp}\Phi_{mp})$ are collected in two sets ($j = 1, 2$):

$$\left\{\Phi_{mp} + \frac{j2\pi}{\sigma_{jmp}}l \;:\; l = 0, \ldots, \sigma_{jmp} - 1\right\} \tag{21}$$

Since σ_{jmp} are chosen as coprime for every m and p, the intersection of the sets (21) for $j = 1, 2$ contains the unique dealiased argument which is the valid Φ_{mp} [7].

A complication arises when trying to extract the values of (u_m, v_m) from Φ_{mp}, which is our ultimate goal. From the expression for Φ_{mp} we find

$$j\frac{c}{2\omega_0}\Phi_{mp} + \frac{r_{p_j} - \kappa_{mp_j}}{\sigma_{jmp}} = \sqrt{R_p^2 + \Delta_{mp}}$$

Inside the square root we have

$$\begin{aligned} R_p^2 + \Delta_{mp} &= x_p^2 + y_p^2 + Z_p^2 + u_m^2 + v_m^2 - 2(u_m x_p + v_m y_p) \\ &= (u_m - x_p)^2 + (v_m - y_p)^2 + Z_p^2 \end{aligned} \tag{22}$$

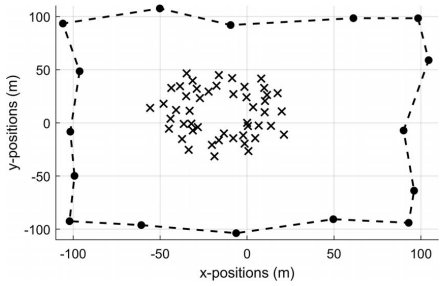

Figure 2. Antenna positions and UAV flight path.

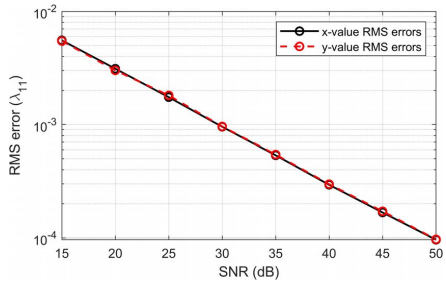

Figure 3. Root-mean-square errors of element positions in a LOFAR LBA outer substation for different noise levels using the linearized near-field model with $P = 16$ and $N_t = 80$.

Equation (22) defines a circle with center (x_p, y_p) and radius $R_p^2 - Z_p^2 + \Delta_{mp}$. Thus for any two distinct positions of the UAV, the possible solutions of (u_m, v_m) occur at the intersections of two circles. To find the correct solution, we add distinct UAV positions so that $P \geq 3$ and we have $N_c = \binom{P}{2}$ combinations of pairs of circles whose intersections are possible solutions of (u_m, v_m). We use the mean of the N_c closest intersections as the solution to (u_m, v_m), which then becomes the updated value of $(\tilde{u}_m, \tilde{v}_m)$ in the linear model in (13). The entire procedure discussed in this section is repeated until

$$\sqrt{(u_m - \tilde{u}_m)^2 + (v_m - \tilde{v}_m)^2} < 0.01 \qquad (23)$$

This iterative process should converge due to the convexity of the linearized function

$$\begin{aligned} g_p(u, v) &= r_p - \sqrt{r_p^2 + u^2 + v^2 - 2(ux_p + vy_p)} \\ &= r_p - \sqrt{(x_p - u)^2 + (y_p - v)^2 + z_p^2}. \end{aligned}$$

6. Simulation Results

In practice, this method is performed off-line using the time-series signals from each antenna element in the respective frequency bins, as described in (3). To demonstrate that the algorithm works, we present results from a controlled simulation that does not include practical considerations such as mutual coupling or the precision with which the UAV's position can be determined. However, the simulation parameters are from actual in situ measurement campaigns that were performed on the LOFAR low-band antenna (LBA), such as in [9]. We use the outer LBA substation for our simulation, for which the positions of the antenna elements are indicated by the crosses in Figure 2. The flight path of the UAV is a 100 m × 100 m square, with some deviations caused by wind. The black dots indicate the $P = 16$ positions that are used.

The fifth, seventh, ninth, and 11th harmonics of the baseband frequency $f_0 = 6.3585$ MHz are transmitted from the UAV, so $i = [2,3,4,5]$. One hundred Monte Carlo runs were performed for signal-to-noise ratios (SNRs) of 15 dB to 50 dB. The number of samples at each position is $N_t = 80$. For each antenna, the median estimated position over all runs was taken and compared with the actual position. The root-mean-square (RMS) errors of the difference between the x- and y-positions for all the antenna elements were calculated at each noise level. The results are presented in Figure 3 in terms of the wavelength of the highest frequency harmonic $\lambda_{11} = 4.29$ m transmitted from the UAV. Even at an SNR of 15 dB, the RMS error is less than 1% of the smallest transmitted wavelength λ_{11}, confirming the efficacy of the computational method.

7. Conclusion

This article expands on the work in [4] by replacing the far-field approximation with the more realistic near-field model, along with other subtle improvements. In order to use the proposed subsampling algorithm, it is necessary to linearize the model and solve for the antenna positions iteratively. Simulation results that do not yet consider various practical problems indicate that the algorithm works well. In future, practical effects such as mutual coupling between antenna elements in the array will be considered before moving on to applying the algorithm to practical data from the field.

8. Acknowledgments

This research received funding from the European Union's Horizon 2020 Research and Innovation Programme under the Marie Skłodowska-Curie grant agreement 101008231 (EXPOWER). It is also based on research supported in part by the National Research Foundation of South Africa (grant 75322), as well as the Netherlands Organisation for Scientific Research.

9. References

1. M. P. van Haarlem, M. W. Wise, A. W. Gunst, G. Heald, J. P. McKean, et al., "LOFAR: The Low-Frequency Array,"

Astronomy & Astrophysics, **556**, August 2013, p. A2, doi: 10.1051/0004-6361/201220873.
2. P. E. Dewdney, P. J. Hall, R. T. Schilizzi, and T. J. L. W. Lazio, "The Square Kilometre Array," *Proceedings of the IEEE*, **97**, 8, August 2009, pp. 1482-1496, doi: 10.1109/JPROC.2009.2021005.
3. S. J. Wijnholds, G. Pupillo, P. Bolli, and G. Virone, "UAV-Aided Calibration for Commissioning of Phased Array Radio Telescopes," 2016 URSI Asia-Pacific Radio Science Conference (URSI AP-RASC), Seoul, South Korea, August 21–25, 2016, pp. 228-231, doi: 10.1109/URSIAP-RASC.2016.7601375.
4. R. Louw, F. Knaepkens, A. Cuyt, W.-s. Lee, S. J. Wijnholds, et al., "Antenna Position Estimation Through Sub-Sampled Exponential Analysis of Harmonically Related Input Signals," 2021 XXXIVth General Assembly and Scientific Symposium of the International Union of Radio Science (URSI GASS), Rome, Italy, August 28–September 4, 2021, pp. 1-4, doi: 10.23919/URSIGASS51995.2021.9560519.
5. A. Cuyt, Y. Hou, F. Knaepkens, and W-s. Lee, "Sparse Multidimensional Exponential Analysis With an Application to Radar Imaging," *SIAM Journal on Scientific Computing*, **42**, 3, 2020, pp. B675-B695, doi: 10.1137/19M1278004.
6. M. Briani, A. Cuyt, F. Knaepkens, and W-s. Lee, "VEXPA: Validated EXPonential Analysis Through Regular Sub-Sampling," *Signal Processing*, **177**, December 2020, p. 107722, doi: 10.1016/j.sigpro.2020.107722.
7. A. Cuyt and W-s. Lee, "How to Get High Resolution Results From Sparse and Coarsely Sampled Data," *Applied and Computational Harmonic Analysis*, **48**, 3, May 2020, pp. 1066-1087, doi: 10.1016/j.acha.2018.10.001.
8. A. Barabell, "Improving the Resolution Performance of Eigenstructure-Based Direction-Finding Algorithms," ICASSP '83: IEEE International Conference on Acoustics, Speech, and Signal Processing, Boston, MA, USA, April 14–16, 1983, pp. 336-339, doi: 10.1109/ICASSP.1983.1172124.
9. G. Virone, P. Bolli, F. Paonessa, G. Pupillo, S. J. Wijnholds, et al., "Strong Mutual Coupling Effects on LOFAR: Modeling and In Situ Validation," *IEEE Transactions on Antennas and Propagation*, **66**, 5, May 2018, pp. 2581-2588, doi: 10.1109/TAP.2018.2816651.

Chapter 4

Simulated Performance of Antenna Position Estimation through Sub-Sampled Exponential Analysis

Simulated Performance of Antenna Position Estimation through Sub-Sampled Exponential Analysis

Rina-Mari Weideman
Dept of Electrical & Electronic Engineering
Stellenbosch University
Stellenbosch, South Africa
18954626@sun.ac.za

Ridalise Louw
Dept of Electrical & Electronic Engineering
Stellenbosch University
Stellenbosch, South Africa
17002567@sun.ac.za

Ferre Knaepkens
Dept of Computer Science
University of Antwerp
Antwerp, Belgium
ferre.knaepkens@uantwerpen.be

Dirk de Villiers
Dept of Electrical & Electronic Engineering
Stellenbosch University
Stellenbosch, South Africa
ddv@sun.ac.za

Annie Cuyt
Dept of Computer Science
University of Antwerp
Antwerp, Belgium
annie.cuyt@uantwerpen.be

Wen-Shin Lee
Division of Computing Science and Mathematics
University of Stirling
Scotland, UK
wen-shin.lee@stir.ac.uk

Stefan J. Wijnholds
Dept of Innovation & Systems
Netherlands Institute for Radio Astronomy (ASTRON)
Dwingeloo, The Netherlands
Dept of Electrical & Electronic Engineering
Stellenbosch University
Stellenbosch, South Africa
wijnholds@astron.nl

***Abstract*—Antenna position estimation is an important problem in large irregular arrays where the positions might not be known very accurately from the start. In a previous paper we presented a method using harmonically related signals transmitted from an Unmanned Aerial Vehicle (UAV), with the added advantage that the UAV can be in the near-field of the receiving antenna array. It was shown that the method delivers excellent results using ideal synthetic data with added noise. In this paper we continue the work by simulating the problem in a full-wave solver. Although the results are less accurate than when synthetic data are used, due to the effects of mutual coupling, the method still performs satisfactorily, with errors smaller than 4% of the smallest transmitted wavelength.**

***Index Terms*—Antenna Arrays, Antenna Measurements, Mutual Coupling, Unmanned Aerial Vehicles**

I. Introduction

Large irregular antenna arrays such as the Low Frequency Array (LOFAR) [1] and the Square Kilometre Array (SKA) [2] have the disadvantage that the position of each antenna needs to be verified after installation. Connection problems such as switched cables will also translate to positional errors. By using signals transmitted from an Unmanned Aerial Vehicle (UAV) and received at each individual element, proposed methods such as those in [3] and [4] can accurately find the positions, compensating for inaccurate placements during the installation phase.

In [4], we specifically focused on cases where the UAV is in the near-field of the array. It was shown that the method delivers sufficiently accurate results with synthetic data, with the Root Mean Square (RMS) error less than 1% of the smallest transmitted wavelength at a signal-to-noise ratio (SNR) of $15\,\mathrm{dB}$.

In this paper, we investigate the performance of the method further with the effect of mutual coupling included, by simulating the problem in a full-wave solver, FEKO [5].

II. Sub-Sampled Exponential Analysis of the Linearised Near-Field Problem

In order to ensure that this paper is self-contained, we provide a brief summary of the mathematical details presented in [4].

The UAV transmits narrowband odd harmonic signals

$$S_i(t_p) = s_i(t_p)\exp(j\omega_i t_p)$$

towards the array at time t_p when located at position $\mathbf{r}_p = x_p\mathbf{x} + y_p\mathbf{y} + z_p\mathbf{z}$ where $s_i(t_p)$ is assumed to remain constant during the measurement of $S_i(t_p)$. The index $i \in \mathbb{N}$ distinguishes between frequencies $\omega_i = (2i+1)\omega_0$ where $\omega_0 = 2\pi f_0$ is the base frequency.

Let the reference antenna element have position $\mathbf{a}_0 = (0,0,0)$, coinciding with the origin. All M antenna

elements are assumed to be located in the (x, y)-plane so that the m_{th} element is at position $\mathbf{a}_m = u_m\mathbf{x} + v_m\mathbf{y} + (0)\mathbf{z}$ with $m = 0, \ldots, M-1$. The UAV is in the radiating near-field of the antenna, so a curved phase front is incident on the array and the time delay of incidence on $\mathbf{a}_m$ relative to $\mathbf{a}_0$ at time t_p is

$$\begin{aligned}\tau_m(x_p, y_p, z_p) &= \frac{\|\mathbf{r}_p\| - \|\mathbf{r}_p - \mathbf{a}_m\|}{c} \\ &= \frac{r_p - \sqrt{r_p^2 + u_m^2 + v_m^2 - 2(u_m x_p + v_m y_p)}}{c},\end{aligned} \tag{1}$$

where $r_p = \|\mathbf{r}_p\|$, $\mathbf{r}_p - \mathbf{a}_m$ is the vector from the m_{th} antenna element to the UAV, and c is the propagation velocity of the signal, or the speed of light in free space.

To extract the positions $(u_m, v_m, 0)$ we collect samples at each antenna element while the UAV is at a fixed position $\mathbf{r}_p$ at time t_p, with $p = 1, \ldots, P$ [6]. Then from the narrowband assumption, the samples at the m_{th} element at time t_p for frequency i are:

$$\begin{aligned}f_{mip} &= S_i(t_p + \tau_{mp}) \\ &\approx s_i(t_p)\exp(j\omega_i t_p)\exp(j\omega_i \tau_{mp}) \\ &= s_i(t_p)\exp(j\omega_i t_p)\exp\left((2i+1)\,\Psi_{mp}\right).\end{aligned} \tag{2}$$

where

$$\begin{aligned}\Psi_{mp} &= j\omega_0 \tau_{mp}, \\ \tau_{mp} &= \tau_m(x_p, y_p, z_p) = \frac{1}{c}\left(r_p - \sqrt{r_p^2 + \Delta_{mp}}\right), \\ \Delta_{mp} &= u_m^2 + v_m^2 - 2(u_m x_p + v_m y_p).\end{aligned} \tag{3}$$

To get rid of the frequency and positional dependence in (2), we divide the sample sets f_{mip} by the reference antenna element's samples

$$f_{0ip} = s_i(t_p)\exp(j\omega_i t_p)\exp(0)$$

to give

$$f'_{mip} = \frac{f_{mip}}{f_{0ip}} = \exp\left((2i+1)\,\Psi_{mp}\right). \tag{4}$$

In the dense case where $|2\Psi_{mp}| < \pi$ and no aliasing occurs, the base terms Ψ_{mp} can be recovered from (4) using any Prony-like method. Otherwise, we use the de-aliasing method described in [4] to solve the resulting sub-sampled exponential analysis problem, which uses co-prime scale parameters $\sigma_j, j = 1, 2$. These parameters are generated from two distinct UAV flights performed at different heights z_{p_j} and overlapping planar flight paths. This gives us samples from $2P$ positions $\mathbf{r}_{p_j} = x_p\mathbf{x} + y_p\mathbf{y} + z_{p_j}\mathbf{z}$ normalised by f_{0ip_j} according to (4) at each element

$$\begin{aligned}f'_{mip_j} &= \exp\left((2i+1)\,\Psi_{mp_j}\right) \\ &= \exp\left((2i+1)\,j\frac{\omega_0}{c}\left(r_{p_j} - \sqrt{r_{p_j}^2 + \Delta_{mp}}\right)\right).\end{aligned} \tag{5}$$

The near-field base terms Ψ_{mp_j} are non-linear, so we first linearise the model with a first order Taylor series partial sum. During the linearisation $\mathbf{r}_{p_j}$ remains fixed and

$$g_{p_j}(u_m, v_m) = r_{p_j} - \sqrt{r_{p_j}^2 + \Delta_{mp}} \tag{6}$$

only varies with the planar position (u_m, v_m). We approximate (6) with

$$\begin{aligned}L_p(u_m, v_m) &= r_{p_j} - \sqrt{r_{p_j}^2 + \tilde{\Delta}_{mp}} + \frac{(u_m - \tilde{u}_m)(x_p - \tilde{u}_m)}{\sqrt{r_{p_j}^2 + \tilde{\Delta}_{mp}}} \\ &\quad + \frac{(v_m - \tilde{v}_m)(y_p - \tilde{v}_m)}{\sqrt{r_{p_j}^2 + \tilde{\Delta}_{mp}}} \\ &= \frac{u_m(x_p - \tilde{u}_m) + v_m(y_p - \tilde{v}_m)}{\sqrt{r_{p_j}^2 + \tilde{\Delta}_{mp}}} + \kappa_{mp_j}\end{aligned} \tag{7}$$

where $\tilde{\Delta}_{mp} = \tilde{u}_m^2 + \tilde{v}_m^2 - 2(\tilde{u}_m x_p + \tilde{v}_m y_p)$ and

$$\kappa_{mp_j} = r_{p_j} - \sqrt{r_{p_j}^2 + \tilde{\Delta}_{mp}} - \frac{\tilde{u}_m(x_p - \tilde{u}_m) + \tilde{v}_m(y_p - \tilde{v}_m)}{\sqrt{r_{p_j}^2 + \tilde{\Delta}_{mp}}}$$

denote the constant terms in (7) for a certain estimation $(\tilde{u}_m, \tilde{v}_m)$ of the m_{th} antenna element's true planar position. Through an iterative process, the estimation of $(\tilde{u}_m, \tilde{v}_m)$ gets updated so that the approximation in (7) becomes more accurate as the estimation gets closer to the true value of (u_m, v_m). The remaining function

$$L_p(u_m, v_m) - \kappa_{mp_j} = \frac{u_m(x_p - \tilde{u}_m) + v_m(y_p - \tilde{v}_m)}{\sqrt{r_{p_j}^2 + \tilde{\Delta}_{mp}}} \tag{8}$$

is used to solve the positions of the elements in the antenna array in the near-field sub-Nyquist case, since the common factor

$$C_{mp_j} = \frac{1}{\sqrt{r_{p_j}^2 + \tilde{\Delta}_{mp}}}$$

can be used to model σ_j, $j = 1, 2$ if we introduce the virtual UAV position $\mathbf{R}_p = x_p\mathbf{x} + y_p\mathbf{y} + Z_p\mathbf{z}$ with virtual height Z_p and $R_p = \|\mathbf{R}_p\|$, so that the spatial Nyquist criterion

$$\left|2\left(R_p - \sqrt{R_p^2 + \Delta_{mp}}\right)\right| < \frac{\lambda_0}{2} \tag{9}$$

is met for all m and p, and λ_0 is the wavelength of the base frequency f_0. Then, let

$$C_{mp} = \frac{1}{\sqrt{R_p^2 + \tilde{\Delta}_{mp}}}$$

such that

$$C_{mp_j} = \sigma_{jmp} C_{mp}. \tag{10}$$

We start the iterative process for each antenna with $\tilde{u}_m = \tilde{v}_m = 0$ so that $\tilde{\Delta}_{mp} = 0$ and $\kappa_{mp_j} = 0$. For every iteration step a new estimation of $(\tilde{u}_m, \tilde{v}_m)$ and thus $\tilde{\Delta}_{mp}$ is found, while r_{p_j} remains constant throughout. The values of σ_{jmp} and R_p get updated at every iteration step to give (10), with the only restrictions being that the spatial Nyquist criterion in (9) must be met and $\sigma_{jmp}, j = 1, 2$ must be co-prime in order to recover from aliasing. Assuming $r_{p_1} > r_{p_2}$ then $C_{mp_2} > C_{mp_1}$ for all m and p. From the ratios

$$\frac{\sigma_{2mp}}{\sigma_{1mp}} = \frac{C_{mp_2}}{C_{mp_1}} \tag{11}$$

rounded to two significant digits we get co-prime values for σ_{1mp} and σ_{2mp}. Finally, we denote

$$\begin{aligned}\sigma_{jmp}\Phi_{mp} &= j\frac{2\omega_0}{c}\left(r_{p_j} - \sqrt{r_{p_j}^2 + \Delta_{mp}} - \kappa_{mp_j}\right) \\ &\approx j\frac{2\omega_0}{c}\left(\frac{u_m(x_p - \tilde{u}_m) + v_m(y_p - \tilde{v}_m)}{\sqrt{r_{p_j}^2 + \tilde{\Delta}_{mp}}}\right) \\ &= j\frac{2\sigma_{jmp}\omega_0}{c}\left(\frac{u_m(x_p - \tilde{u}_m) + v_m(y_p - \tilde{v}_m)}{\sqrt{R_p^2 + \tilde{\Delta}_{mp}}}\right) \quad (12)\end{aligned}$$

in order to find the unique de-aliased argument Φ_{mp} from the intersection of the two sets ($j = 1, 2$):

$$\left\{\Phi_{mp} + \frac{j2\pi}{\sigma_{jmp}}l \quad : \quad l = 0, \ldots, \sigma_{jmp} - 1\right\}. \quad (13)$$

A new estimation for the antenna position $(\tilde{u}_m, \tilde{v}_m)$ is found using

$$\Phi_{mp} = j\frac{2\omega_0}{c}\left(\frac{r_{p_j} - \kappa_{mp_j}}{\sigma_{jmp}} - \sqrt{R_p^2 + \Delta_{mp}}\right) \quad (14)$$

as described in [4]. The process is repeated until

$$\epsilon = \sqrt{(u_m - \tilde{u}_m)^2 + (v_m - \tilde{v}_m)^2} < 0.01.$$

A summary of the algorithm is described in Algorithm 1.

Algorithm 1 Antenna Position Estimation in the Near-Field

1: Set ω_0, i, P and the $2P$ UAV positions at $\mathbf{r}_{p_1} = x_p\mathbf{x} + y_p\mathbf{y} + z_{p_1}\mathbf{z}$ and $\mathbf{r}_{p_2} = x_p\mathbf{x} + y_p\mathbf{y} + z_{p_2}\mathbf{z}$
2: Collect the samples $f'_{mip_j}, j = 1, 2$ when the UAV is at $\mathbf{r}_{p_1}$ and $\mathbf{r}_{p_2}$ as in (5)
3: **for** $m = 1$ to $M - 1$ **do**
4: Compute the aliased $\exp\left(2\Psi_{mp_j}\right), j = 1, 2$ with Root-MUSIC [7]
5: Initialize $u_m \leftarrow 0$, $v_m \leftarrow 0$
6: **repeat**
7: $\tilde{u}_m \leftarrow u_m$, $\tilde{v}_m \leftarrow v_m$
8: Calculate $\tilde{\Delta}_{mp}, C_{mp_1}, C_{mp_2}, \kappa_{mp_1}$ and κ_{mp_2}
9: Find co-prime values for σ_{1mp} and σ_{2mp} from (11)
10: Find the de-aliased Φ_{mp} from the intersections in (13)
11: Solve (u_m, v_m) from (14) as the intersections of circle pairs as described in [4]
12: **until** $\epsilon < 0.01$
13: **end for**

III. Experimental Setup

Our experiment consists of a full-wave method of moment (MoM) simulation using FEKO [5]. A simple model is created to represent the 96 antennas of a LOFAR low-band antenna (LBA) sub-station. The elements are inverted-V dipoles, with the height of the vertical pole measuring $1.7\,\mathrm{m}$, and each arm having a length of $1.38\,\mathrm{m}$. Fig. 1 shows a single element as displayed in FEKO.

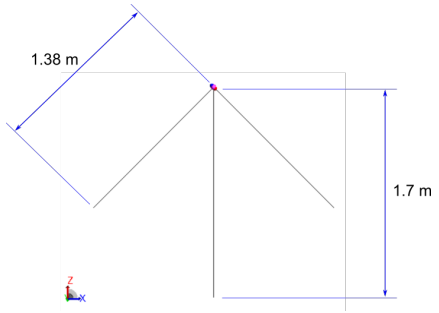

Fig. 1. Example of the inverted-V dipole antenna used as array elements in FEKO. The port is located at the end of one of the dipole arms.

A voltage source of $1\,\mathrm{V}$ is added to the port of a $2\,\mathrm{m}$-long dipole, representing the UAV. Both the transmit and receive antennas have $50\,\Omega$ loads.

A realistic flight path with $P = 16$ positions was chosen, taking on the shape of a $100\,\mathrm{m} \times 100\,\mathrm{m}$ square, slightly altered by the effect of the wind. The positions of the antenna elements, as well as the UAV flight path, are shown in Fig. 2.

The frequencies used in the simulation are $31.79\,\mathrm{MHz}$, $44.51\,\mathrm{MHz}$, $57.23\,\mathrm{MHz}$ and $69.94\,\mathrm{MHz}$. These are equivalent to the 5^{th}, 7^{th}, 9^{th} and 11^{th} harmonics of the base frequency $f_0 = 6.36\,\mathrm{MHz}$, meaning $i = [2, 3, 4, 5]$.

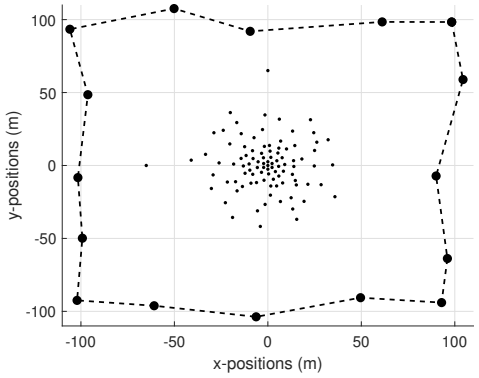

Fig. 2. Antenna positions and UAV flight path.

IV. Results

We calculate the error in position of each antenna individually in both directions, as a fraction of the smallest transmitted wavelength $\lambda_{11} = 4.3\,\mathrm{m}$. The results are shown in the middle panels of Fig. 3 and Fig. 4. The mean errors of all antenna positions in the x- and y-direction are $0.023\,\lambda_{11}$ and $0.031\,\lambda_{11}$, respectively.

In [4], at an SNR of $15\,\mathrm{dB}$, the RMS errors in both directions are smaller than $0.01\,\lambda_{11}$. It is to be expected that

the results of the FEKO-simulated experiment will be less accurate than those of [4], as the physical properties are now included, leading to mutual coupling. However, the errors in Fig. 3 and Fig. 4 are sufficiently low for accurate position estimation.

To investigate further, we scale the entire array with a factor of 0.5. This means the position of each element changes from (u_m, v_m) to $\left(\frac{u_m}{2}, \frac{v_m}{2}\right)$. The element dimensions remain unchanged, as well as the UAV dimensions, flight path and frequencies. As the spacing between the elements becomes smaller, we expect the mutual coupling effects to be stronger and the results to worsen. This expectation is confirmed, as seen in the top panels of Fig. 3 and Fig. 4, where the mean errors in the x- and y-direction are $0.11\,\lambda_{11}$ and $0.098\,\lambda_{11}$, respectively. In a similar fashion, we also scale the array with a factor 1.5, to enlarge the spacing between the elements. These results are shown in the bottom panels of Fig. 3 and Fig. 4. As expected, the results have improved from the top panels, as the mutual coupling is weakened. The mean Euclidean errors of the three experiments are summarised in Table I. Here we can clearly see the trend that a larger spacing between elements leads to smaller errors.

As part of future work, we will investigate the case of switched cables in the array, and also incorporate a calibration technique to mitigate the mutual coupling effects.

TABLE I
POSITIONAL ERRORS RELATING TO ELEMENT SPACING

Scale	Mean Euclidean error (λ_{11})
0.5	0.17
1	0.042
1.5	0.038

V. CONCLUSION

In this paper, we extend the work done in [4], which described the results of the sub-sampled antenna position estimation in the near-field using synthetic data. To advance to a scenario that is truer to the practical system, we specifically focus on a simulated experiment including mutual coupling. We do this by creating a FEKO model based on the LOFAR LBA, with a UAV transmitting harmonically related signals from known positions in the sky.

The results prove to be accurate, with the mean errors in both x- and y-directions lower than 4% of the smallest transmitted wavelength. We also see how the spacing between the array elements relates to the positional error, with larger separations translating into smaller errors due to decreased mutual coupling.

Future work includes investigating the case of switched cables, incorporating a calibration method, investigating the impact of other practical effects, and testing our method with practical data of LOFAR.

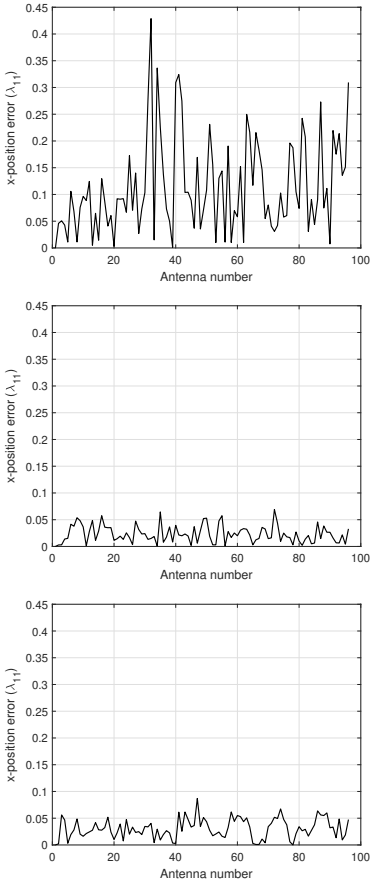

Fig. 3. Positional errors in the x-direction in terms of the smallest transmitted wavelength $\lambda_{11} = 4.3\,\mathrm{m}$. The nominal positions are scaled coordinates of the LOFAR LBA elements, with a scale factor of 0.5, 1 and 1.5 for the top, middle and bottom panels, respectively.

ACKNOWLEDGMENT

This research has received funding from the European Union's Horizon 2020 research and innovation programme under the Marie Skłodowska-Curie grant agreement No 101008231 (EXPOWER). It is also based on research supported in part by the National Research Foundation of South Africa (Grant Number 75322), as well as the Netherlands Organisation for Scientific Research.

REFERENCES

[1] M.P. van Haarlem et al., "LOFAR: The Low Frequency Array", Astronomy & Astrophysics, 556, A2, August 2013, pp. 1–53, doi: 10.1051/0004-6361/201220873

[2] P. E. Dewdney, P. J. Hall, R. T. Schilizzi, and T. J. L. W. Lazio, "The Square Kilometre Array," Proceedings of the IEEE, 97, 8, August 2009, pp. 1482–1496, doi: 10.1109/JPROC.2009.2021005.

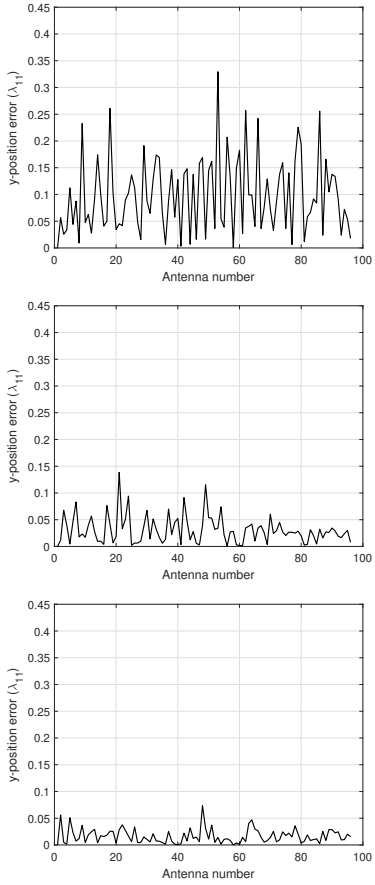

Fig. 4. Positional errors in the y-direction in terms of the smallest transmitted wavelength $\lambda_{11} = 4.3\,\mathrm{m}$. The nominal positions are scaled coordinates of the LOFAR LBA elements, with a scale factor of 0.5, 1 and 1.5 for the top, middle and bottom panels, respectively.

[3] S. J. Wijnholds, G. Pupillo, P. Bolli, and G. Virone, "UAV-Aided Calibration for Commissioning of Phased Array Radio Telescopes," in URSI Asia-Pacific Radio Science Conference (URSI AP-RASC), 2016, pp. 228–231, doi: 10.1109/URSIAP-RASC.2016.7601375.

[4] R. Louw, F. Knaepkens, A. Cuyt, W-s. Lee, S. J. Wijnholds, D. I. L. de Villiers R. Weideman, "Antenna Position Estimation through Sub-Sampled Exponential Analysis of Signals in the Near-Field," URSI Radio Science Letters, 2022, in press.

[5] Altair Development S.A. (Pty) Ltd, Stellenbosch, South Africa. FEKO 2021.2. [Online]. Available: https://altairhyperworks.com/feko/

[6] A. Cuyt, Y. Hou, F. Knaepkens and W-s. Lee, "Sparse Multidimensional Exponential Analysis with an Application to Radar Imaging," *SIAM Journal on Scientific Computing*, **42**, 3, 2020, pp. B675-B695, doi:10.1137/19M1278004.

[7] A. Barabell, "Improving the resolution performance of eigenstructure-based direction-finding algorithms," ICASSP '83. IEEE International Conference on Acoustics, Speech, and Signal Processing, 1983, pp. 336-339, doi: 10.1109/ICASSP.1983.1172124.

Part III

Reflector Frequency Ripple Characterisation

Preface to Part III

In the final part of this dissertation, it is shown how VEXPA can be used to characterise the frequency ripple in different reflector antenna figures of merit. Simulating reflector antennas at densely-sampled frequencies is computationally expensive, and therefore the sub-sampling capability that VEXPA offers is useful in this application.

In Chapter 5, it is assumed that a densely-sampled function of the antenna noise temperature is available, and VEXPA is used to extract the frequency components of this function [1]. The method is compared to the Fourier transform with different pre-processing steps. These steps are required due to the dominating power law behaviour of the antenna noise temperature, while VEXPA requires no pre-processing.

Introducing the use of sub-sampling, in Chapter 6 we show how the electric field components can be reconstructed from sub-sampled data points [2]. By achieving an accurate reconstruction of the electric fields, corresponding figures of merit can accurately be predicted. Specifically, these figures of merit are the antenna noise temperature and the aperture efficiency. As in Chapter 5, it is shown how VEXPA can be used for the spectral analysis of the reconstructed function, without the need for any pre-processing steps required by the Fourier transform.

References

[1] R.-M. Weideman, A. Cuyt, and D. I. L. De Villiers, "Characterising the frequency ripple in antenna noise temperature using exponential analysis", in *2023 International Conference on Electromagnetics in Advanced Applications (ICEAA)*, 2023.

[2] R.-M. Weideman, A. Cuyt, and D. I. L. De Villiers, "Characterising the electric field ripple in reflector antennas using sub-sampled exponential analysis", submitted.

Chapter 5

Characterising the Frequency Ripple in Antenna Noise Temperature Using Exponential Analysis

Characterising the Frequency Ripple in Antenna Noise Temperature Using Exponential Analysis

Rina-Mari Weideman
Dept of Electrical & Electronic Eng.
Stellenbosch University
Stellenbosch, South Africa
18954626@sun.ac.za

Annie Cuyt
Dept of Computer Science
University of Antwerp
Antwerp, Belgium
University of Stirling
Scotland, UK
Eindhoven University of Technology
Eindhoven, The Netherlands
annie.cuyt@uantwerpen.be

Dirk de Villiers
Dept of Electrical & Electronic Eng.
Stellenbosch University
Stellenbosch, South Africa
ddv@sun.ac.za

***Abstract*—This paper presents a method for characterising the ripple observed in the antenna noise temperature of reflector systems as a function of operating frequency. The ripple, which is superimposed on the dominant power-law shape, must be accurately characterised in order to determine its impact. Traditional methods, such as Fourier transform analysis, typically involve some preprocessing to reduce the effect of the power law, which may inadvertently introduce additional ripple components. To overcome this limitation, it is shown how the Validated EXPonential Analysis (VEXPA) method can be used without the need to remove the trend of the curve. The results demonstrate that VEXPA produces accurate results and is therefore a valuable alternative to traditional methods.**

***Index Terms*—Ripple, Antenna Noise Temperature, Exponential Analysis**

I. Introduction

Ground-based reflector antennas employed in radio telescope instruments such as the MeerKAT [1], Square Kilometre Array (SKA) [2], and HIRAX [3] telescopes operate over wide instantaneous bandwidths. Characterization of the instrumental response over the full operating frequency range is an important requirement to determine the suitability of using the instrument for observations towards specific science goals. Specifically, one of the primary figures of merit is the receiving sensitivity, which is a measure of the weakest signal strength that can be detected by a receiver [4]. It is described as the ratio between the effective aperture area and system noise temperature:

$$\frac{A_{\mathrm{e}}}{T_{\mathrm{sys}}} = \frac{\eta_{\mathrm{ap}} A_{\mathrm{phy}}}{T_{\mathrm{A}} + T_{\mathrm{rec}}}. \tag{1}$$

One can see from the equation above that the effective aperture area is described as the product of the aperture efficiency η_{ap} and the main reflector projected aperture area A_{phy}, whereas the system noise temperature T_{sys} is the sum of the antenna noise temperature T_{A} and the receiver noise temperature T_{rec}. The antenna noise temperature is calculated as

$$T_A\left(f|\widehat{\boldsymbol{r}}_0\right) = \frac{\iint_{4\pi} N\left(f,\Omega|\widehat{\boldsymbol{r}}_0\right)\sin\theta d\Omega}{\iint_{4\pi} P\left(f,\Omega\right)\sin\theta d\Omega}, \tag{2}$$

where

$$N\left(f,\Omega|\widehat{\boldsymbol{r}}_0\right) = T_b\left(f,\Omega\right) P\left(f,\Omega|\widehat{\boldsymbol{r}}_0\right). \tag{3}$$

The product in (3) consists of the brightness temperature $T_b\left(\cdot\right)$ and the antenna radiation intensity $P\left(\cdot\right)$, with the reflector pointing in the direction $\widehat{\boldsymbol{r}}_0$ and operating at frequency f. The spherical coordinate system is described by $\Omega = (\theta, \phi)$.

In reflector systems, the radiation intensity $P\left(\cdot\right)$ often contains a frequency ripple, in turn creating a ripple in T_A. This is due to interference between plane waves apparently emanating, due to reflection and diffraction, from the different structures of the antenna - the feed, sub-reflector and main-reflector [5]. This ripple could be troublesome when radio frequency spectroscopy is performed, specifically in HI observations where the spectral width of the principle ripple components are similar to the HI line widths of galaxies [5], [6]. It is therefore important that this ripple is characterised to determine its effect.

In this paper, we propose an exponential analysis method to obtain an accurate description of the frequency contents of T_A, thereby characterising the ripple. Since the calculation of T_A is non-trivial, we assume its values are known at densely-sampled frequency points, and only focus on converting it to its frequency-domain representation.

We apply our method to an example reflector antenna, and discuss how it circumvents certain issues that arise when applying classic Fourier methods, while delivering accurate results.

II. Method

We approach the ripple characterisation problem by considering a fixed pointing direction $\widehat{\boldsymbol{r}}_0$, and expressing T_A as a sum of exponentials

$$T_A(f) = \sum_{i=1}^{n} a_i \exp\left(\nu_i f\right), \qquad a_i, \nu_i \in \mathbb{C} \tag{4}$$

where the a_i are the complex amplitudes and the ν_i are the complex frequencies in radians. Assume samples of T_A are

available at frequencies $f_m = f_0 + m\Delta$ for $m = 0, 1, ..., M-1$, where Δ is the sampling step and M is the total number of samples. Dropping the subscript A, the samples can then be represented by

$$T_m = \sum_{i=1}^{n} a_i \exp(\nu_i f_0) \exp(\nu_i m\Delta), \tag{5}$$

for $m = 0, 1, ..., M-1$. Because the factor $\exp(\nu_i f_0)$ is constant, it can be included in the coefficient

$$T_m = \sum_{i=1}^{n} \alpha_i \exp(\nu_i m\Delta), \tag{6}$$

with $\alpha_i = a_i \exp(\nu_i f_0)$.

Validated EXPonential Analysis (VEXPA) [7] is an exponential analysis method that computes the coefficients α_i and frequencies ν_i, as well as the number of frequency components n. It makes use of scaled and shifted sets of samples, defined by the co-prime scale and shift parameters σ and ρ.

Firstly, the scaled sets of samples are obtained by sampling at the sampling step Δ scaled with a factor σ, i.e., at frequencies $f_{m\sigma} = f_0 + m\sigma\Delta$ for $m = 0, 1, ..., M_\sigma - 1$. The scaled samples are expressed as

$$\begin{aligned} T_{m\sigma} &= \sum_{i=1}^{n} \alpha_i \exp(\nu_i m\sigma\Delta) \\ &= \sum_{i=1}^{n} \alpha_i (\Psi_i^\sigma)^m, \qquad m = 0, 1, ..., M_\sigma - 1, \end{aligned} \tag{7}$$

where $\Psi_i = \exp(\nu_i \Delta)$.

The first step is to use any Prony-based algorithm to compute the so-called aliased base terms Ψ_i^σ. In this case, our method of choice is the Matrix-Pencil method [8]. A total of N base terms are computed, where N is an overestimation of the number of frequency components n. Since $2n$ samples are needed to extract the $2n$ parameters α_i and Ψ_i^ρ, a total of at least $M_\sigma = 2n$ samples are needed to recover n terms. N is therefore set equal to a value between $\lfloor M_\sigma/3 \rfloor$ and $\lfloor M_\sigma/2 \rfloor$ [7], [8]. The lower limit is chosen if many samples are available, making it safe to assume that the number of samples $\lfloor M_\sigma/3 \rfloor$ is larger than the number of terms n.

It should be noted that, depending on the sampling step, the recovery of the frequencies ν_i from the base terms Ψ_i^σ might deliver ambiguous results if the Nyquist sampling criterion is not met. This is dealt with by VEXPA through the use of shifted sets of samples, taken at frequencies $f_{m\sigma + r\rho} = f_0 + \Delta(m\sigma + r\rho)$ for $m = 0, 1, ..., M_\rho - 1$ and $r = 0, 1, ..., R-1$. Here, ρ is the shift parameter and R is the number of shifts that are performed. The shifted samples are

$$\begin{aligned} T_{m\sigma+r\rho} &= \sum_{i=1}^{n} \alpha_i \exp(\nu_i \Delta(m\sigma + r\rho)) \\ &= \sum_{i=1}^{n} (\alpha_i \Psi_i^{r\rho})(\Psi_i^\sigma)^m, \qquad m = 0, 1, ..., M_\rho - 1. \end{aligned} \tag{8}$$

For each shift r, we solve the Vandermonde system using the base terms Ψ_i^σ (which have been computed by the Matrix-Pencil method) and the shifted samples $T_{m\sigma+r\rho}$ to find the values of $\alpha_i \Psi_i^{r\rho}$:

$$\begin{bmatrix} 1 & \dots & 1 \\ \Psi_1^\sigma & \dots & \Psi_N^\sigma \\ \vdots & \ddots & \vdots \\ \Psi_1^{\sigma(M_\sigma-1)} & \dots & \Psi_N^{\sigma(M_\sigma-1)} \end{bmatrix} \begin{bmatrix} \alpha_1 \Psi_1^{r\rho} \\ \alpha_2 \Psi_2^{r\rho} \\ \vdots \\ \alpha_N \Psi_N^{r\rho} \end{bmatrix} = \begin{bmatrix} T_0 \\ T_{\sigma+r\rho} \\ \vdots \\ T_{(M_\sigma-1)\sigma+r\rho} \end{bmatrix}. \tag{9}$$

This system is solved R times, r taking a distinct value between 0 and $R-1$ each time. The combined results of each system give the sequence

$$\alpha_i,\ \alpha_i \Psi_i^\rho,\ \alpha_i \Psi_i^{r\rho},\ \dots,\ \alpha_i \Psi_i^{(R-1)\rho}. \tag{10}$$

For fixed i, this follows the same exponential model as in (7) [7]. The Matrix-Pencil method is therefore used again, now to compute the Ψ_i^ρ for $i = 1, ..., N$.

Because a large number of samples are available, one can repeat the above-mentioned process for a number of different starting frequencies f_0. Define the number of repetitions as K. For each repetition, solutions are collected for both Ψ_i^σ and Ψ_i^ρ for $i = 1, ..., N$, where N is the overestimated number of terms. There are therefore in total KN solutions for both Ψ^σ and Ψ^ρ. To get a final solution for the aliased base terms, one can pass these KN solutions to a cluster analysis method such as Density-Based Spatial Clustering of Applications with Noise (DBSCAN) [9]. The underlying function will stay unchanged with each repetition, while the noise will have a different realisation with each one. This means that the true base terms will form clusters, while the noisy ones will be scattered [7]. The number of frequency components n is therefore estimated as the number of clusters found by DBSCAN[1], and the final values of the base terms are the centroids of these clusters.

To extract the de-aliased base terms Ψ_i from the aliased ones, we find the intersections of the sets $(\Psi_i^\sigma)^{\frac{1}{\sigma}}$ and $(\Psi_i^\rho)^{\frac{1}{\rho}}$ for $i = 1, ..., n$, as described in [7]. From Ψ_i, the complex frequencies can be found as $\nu_i = \ln(\Psi_i)/\Delta$.

When working with real-valued data such as the antenna noise temperature, the frequencies ν_i appear as a combination of two options: 1) real-valued ν_i that translate to exponential decaying terms, and 2) complex conjugate pairs that translate to cosine terms when summed as in (4). To illustrate the latter option, consider a case with no decaying terms. We can write the coefficients a_i in their polar form as $a_i = |a_i| \exp(jp_i)$ and rewrite (4) as the sum of exponents consisting of complex

[1] Slightly adapted since publication.

conjugate pairs:

$$\begin{aligned} T_A(f) &= \sum_{i=1}^{n/2} |a_i| \exp\left(\mathrm{Re}(\nu_i) f + j\left(\mathrm{Im}\left(\nu_i\right) f + p_i\right)\right) \\ &+ \sum_{i=1}^{n/2} |a_i| \exp\left(\mathrm{Re}(\nu_i) f - j\left(\mathrm{Im}\left(\nu_i\right) f + p_i\right)\right) \\ &= \sum_{i=1}^{n/2} 2|a_i| \exp\left(\mathrm{Re}(\nu_i) f\right) \cos\left(\left(\mathrm{Im}\left(\nu_i\right) f + p_i\right)\right). \end{aligned} \tag{11}$$

From the equation above, we see that $n/2$ ripple components are extracted from n exponential terms, with the ripple frequencies being equivalent to the imaginary parts of the complex frequencies ν_i.

The maximum number of detected ripple components is therefore half of the maximum number of detected exponential terms, i.e., $\lfloor \lfloor M_\sigma/2 \rfloor /2 \rfloor = \lfloor M_\sigma/4 \rfloor$. On the other hand, if we are working with a signal with decaying terms exclusively, the maximum number of detected terms is the same as the maximum number of exponential terms, i.e., $\lfloor M_\sigma/2 \rfloor$. In most cases, both of these types of terms are present, and therefore the maximum number of terms lies somewhere in between these values. Since the data are densely-sampled, however, we have a large number of samples available and can safely find all the ripple components.

Now that we have found the frequencies of the ripple components, the only step that remains is to find their weights. This is done by computing the coefficients α_i through solving the Vandermonde system

$$\begin{bmatrix} 1 & \dots & 1 \\ \Psi_1 & \dots & \Psi_n \\ \vdots & \ddots & \vdots \\ \Psi_1^{M-1} & \dots & \Psi_n^{M-1} \end{bmatrix} \begin{bmatrix} \alpha_1 \\ \alpha_2 \\ \vdots \\ \alpha_n \end{bmatrix} = \begin{bmatrix} T_0 \\ T_1 \\ \vdots \\ T_{M-1} \end{bmatrix} \tag{12}$$

in a least squares sense.

A summary of the method is described in Algorithm 1.

Algorithm 1 Ripple Frequency Characterisation

1: Collect M densely-sampled T_A data points for fixed $\widehat{\boldsymbol{r}}_0$ and varying f.
2: **for** $k = 0$ to $K - 1$ **do**
3: Use the Matrix-Pencil method to compute the aliased base terms Ψ_i^σ for $i = 1, ..., N$ using the samples described in (7) with starting frequency $f_0 = f_k$.
4: **for** $r = 0$ to $R - 1$ **do**
5: Compute the terms $\alpha_i \Psi_i^{r\rho}$ for $i = 1, ..., N$ by using (9).
6: **end for**
7: Use the Matrix-Pencil method to compute Ψ_i^ρ for $i = 1, ..., N$ using the terms $\alpha_i \Psi_i^{r\rho}$ computed in the previous step.
8: **end for**
9: Pass the KN solutions of Ψ_i^σ and Ψ_i^ρ to DBSCAN to find the final estimation of the number of terms n, and the final solutions of Ψ_i^σ and Ψ_i^ρ for $i = 1, ..., n$.
10: Use the de-aliasing method described in [7] to solve for Ψ_i.
11: Find the ripple frequencies by discarding one term of each complex conjugate pair in Ψ_i and taking the imaginary part of $\nu_i = \ln(\Psi_i)/\Delta$.

III. Experimental Setup

In order to investigate the performance of our method, we construct an example using the T_A data of a reflector antenna at 801 frequency points in the range $[0.7 - 1.5]$ GHz, and at tipping angle $\theta_p = 0°$. The reflector system is an offset Gregorian system, defined using the description in [10], with parameters $D_m = 6$m, $\theta_0 = -73.7°$, $\theta_e = 45°$, $L_s = 1.3228$m and $\beta = 41.36°$. A Gaussian pattern with -10 dB edge taper is used to illuminate the dish. Fig. 1 shows the antenna noise temperature at zenith, calculated using the background temperature model described in [11]. It is clear that a slowly varying power law dominates the behaviour of the function, meaning that performing a standard Fourier analysis will result in a spectrum where the ripple components are unidentifiable. A simple yet imperfect solution to this problem is detrending the data. This refers to the process of fitting an approximation to the trend of the data, and subtracting this approximation. The problem with this approach is that the subtraction could lead to the injection of false ripple components. VEXPA holds the advantage of avoiding this subtraction, since the method will resolve both the power law and ripple components as separate terms. The power law will simply appear as real-valued ν_i, whereas the ripple components are the result of the sum of complex conjugate pairs, as described by (11).

Other methods attempting to distinguish the ripple components from the power law behaviour include applying a window function or a high-pass filter to the data before performing the Fourier transform. By applying a window function, the amplitude of the signal is reduced towards the edges of the window, which diminishes the impact of the dominant power law in the Fourier spectrum. By filtering the data with a high-pass filter, the components at lower frequencies are suppressed, which will also remove the power law component from the spectrum. However, these methods are also not faultless, as will be shown in the next section.

To confirm the results delivered by VEXPA, we execute the algorithm five times with different σ and ρ parameter pairs. A frequency component is considered confirmed if it appears as a result at least four out of five times.

The chosen parameters used by VEXPA for the different σ, ρ pairs are summarised in Table I.

IV. Results

The T_A function reconstructed by using the results from VEXPA and the exponential model in (4) is shown in Fig. 2, with its absolute error. The reconstructed function clearly follows the original function very closely and the error is very

TABLE I
VEXPA PARAMETERS

$\sigma,\ \rho$	M_σ	M_ρ	R	K
5, 2	161	161	3	σ
5, 3	161	161	3	σ
7, 2	115	115	3	σ
7, 3	115	115	3	σ
8, 3	101	101	3	σ

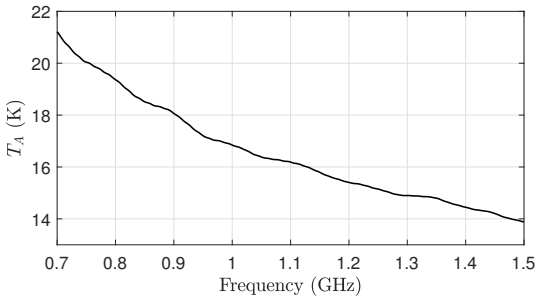

Fig. 1. Antenna noise temperature sampled at 801 frequency points.

small, with a maximum absolute error of 0.027K. This means that the corresponding frequency components can be trusted.

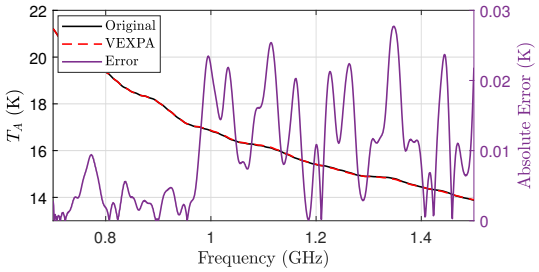

Fig. 2. Original T_A function, with the reconstructed version as described by VEXPA, and the absolute error of the reconstruction function. The reconstructed version follows the original one very closely, with a maximum absolute error of 0.027K. This means that the frequency components used for the reconstruction will be an accurate description of the ripple.

Fig. 3 shows the results of analysing the T_A function with the different Fourier transforms and VEXPA. The horizontal axis displays the oscillation period; a peak located at a smaller period implies a faster varying ripple component. The vertical axis displays the magnitude in decibels for the Fourier transforms, and the normalised magnitude for VEXPA.

For the top graph in Fig. 3, VEXPA is performed on the original data with no subtraction of the trend. Because the method returns individual frequency terms instead of constructing a spectrum, one can simply discard the terms with negligible imaginary parts, since these contribute to the power law behaviour. The number of exponential terms n returned by VEXPA for the five different $\sigma,\ \rho$ pairs is summarised in Table II. By inspecting the table, we can follow the process that finally delivers the results in Fig. 3. Firstly, n refers to the number of exponential terms that VEXPA returns. From these n terms, n_{decay} are discarded as they have purely real frequency values. The remaining number of terms are the complex conjugate pairs $n_{\text{pairs}} = (n - n_{\text{decay}})/2$. Finally, the terms with small weights are discarded; specifically, after the weights have been normalised, those with values smaller than 0.05 are discarded. This leaves a final value of ripple components n_{final}. The four components seen in the top graph of Fig. 3 are the ones that appear as a final result for four out of the five $\sigma,\ \rho$ pairs.

TABLE II
NUMBER OF TERMS n RETURNED BY VEXPA

$\sigma,\ \rho$	5, 2	5, 3	7, 2	7, 3	8, 3
n	46	46	33	33	31
n_{decay}	2	2	3	3	3
n_{pairs}	22	22	15	15	14
n_{final}	5	5	6	6	6

By delivering the resulting ripple components as definitive terms, VEXPA holds an advantage to the Fourier transform, as the latter depends on identifying peaks in a spectrum, which could be a difficult task. Considering the Fourier transform results in Fig. 3, it is clear that the peaks are not easily distinguishable.

The Fourier transform is applied to three different sets of data. Firstly, shown in blue in Fig. 3, are the results from the Fourier transform performed on the windowed data. A Blackman-Harris window is used, chosen due to its low side-lobe levels in the frequency domain. Even though the addition of the window succeeds in revealing some of the ripple components, it still contains dominating power law behaviour at the higher end of the spectrum, meaning that the right-most peak identified by VEXPA will not be identified.

Next, a high-pass filter is applied to the data, producing the results in orange. The filter has a cut-off frequency that corresponds to an oscillation period of 5 GHz (equivalent to 3.7 on the horizontal axis of the graph). The difficulty with this approach is that some knowledge about the ripple in the noise temperature is needed in order to provide a filter cut-off frequency.

Finally, consider the detrended data, i.e., the original data from which a trend approximation has been subtracted. The trend is approximated by using a Trust-Region algorithm and consists of two exponential terms, which can be denoted by $T_{\text{fit}}(f) = a\exp(bf) + c\exp(df)$. The fitted curve can be seen alongside the raw T_A data in Fig. 4. The resulting Fourier transform is shown in black in Fig. 3.

We see that VEXPA and the Fourier transform on the filtered and detrended data deliver similar results, with the components identified by VEXPA corresponding to peaks in the Fourier spectrum. The one exception is the peak in the Fourier spectrum at a horizontal value of approximately 3.7, which goes undetected by VEXPA.

To investigate if this peak might have been introduced by the subtraction of the trend behaviour, we also use VEXPA on the detrended data, which is shown in the bottom graph of Fig. 3. Comparing its results to those in the top graph, we see that a new component has been detected. We can therefore conclude that this component has been injected by the subtraction and is not representative of the ripple in the antenna noise temperature. The Fourier transform thus suffers from the potential misidentification of ripple components when the data is preprocessed through detrending or filtering.

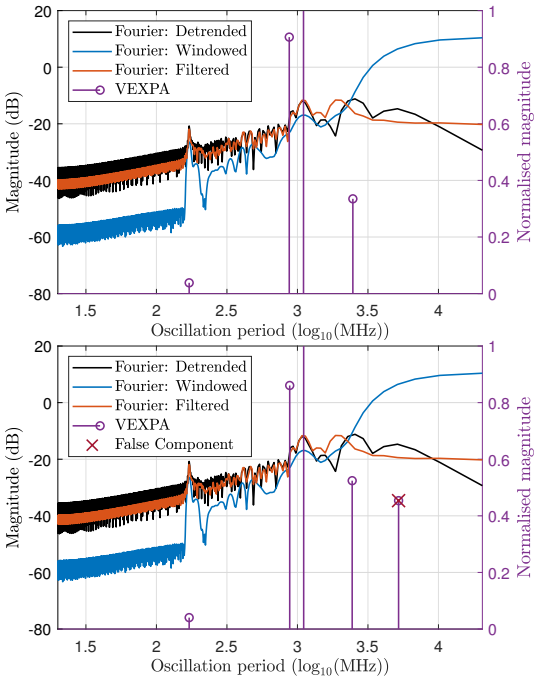

Fig. 3. Frequency contents delivered by VEXPA and the Fourier transform, with the latter being performed on data that have been preprocessed by three different methods. In the top graph, VEXPA uses the original data, whereas it uses the detrended data in the bottom graph. As indicated by the red cross, detrending the data could cause false ripple components to be injected into the frequency analysis and should therefore be avoided.

V. Conclusion

In this paper, we describe how one can apply the exponential analysis method VEXPA to characterise the frequency ripple in densely-sampled antenna noise temperature functions. Traditional methods like the Fourier transform rely on some preprocessing of the data, which is cumbersome and could inject artificial ripple components into the frequency analysis. We show how VEXPA avoids this preprocessing, which leads to a more accurate result.

Future work includes using exponential analysis to acquire an accurate representation of the antenna noise temperature function when it is sampled at a sub-Nyquist rate. This is especially important since sampling the temperature at a large number of frequency points is computationally expensive.

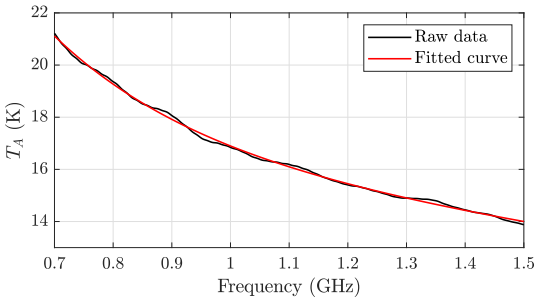

Fig. 4. Antenna noise temperature sampled at 801 frequency points at tipping angle $\theta_p = 0$ degrees (black), and its trend approximation (red).

Acknowledgment

This research has received funding from the European Union's Horizon 2020 research and innovation programme under the Marie Skłodowska-Curie grant agreement No 101008231 (EXPOWER). It is also based on research supported in part by the National Research Foundation of South Africa (Grant Number 75322).

References

[1] J.L. Jonas, "MeerKAT—The South African Array With Composite Dishes and Wide-Band Single Pixel Feeds," in Proceedings of the IEEE, vol. 97, no. 8, pp. 1522-1530, Aug. 2009, doi: 10.1109/JPROC.2009.2020713.

[2] P.E. Dewdney, P.J. Hall, R.T. Schilizzi, and T.J.L.W. Lazio, "The square kilometer array," Proc. IEEE, vol. 97, no. 8, pp. 1482–1496, Aug. 2009.

[3] B.R. Saliwanchik et al., "Mechanical and optical design of the HIRAX radio telescope," Proc. SPIE, vol. 11445, pp. 1047–1067, Jan. 2021.

[4] D.I.L. de Villiers and R. Lehmensiek, "Rapid calculation of antenna noise temperature in offset Gregorian reflector systems," IEEE Trans. Antennas Propag., vol. 63, no. 4, pp. 1564–1571, Apr. 2015.

[5] D.I.L. de Villiers, "Prediction of aperture efficiency ripple in clear aperture offset Gregorian antennas," IEEE Trans. Antennas Propag., vol. 61, no. 5, pp. 2457–2465, 2013.

[6] D.G. Barnes, F.H. Briggs, and M.R. Calabretta, "Postcorrelation ripple removal and radio frequency interference rejection for Parkes Telescope survey data," Radio Science, vol. 40, p. SS513, 2005.

[7] M. Briani, A. Cuyt, F. Knaepkens, and W.-S Lee, "VEXPA: Validated EXPonential Analysis through regular sub-sampling," Signal Processing, vol. 177, p. 107722, 2020. [Online]. Available: https://www.sciencedirect.com/science/article/pii/S0165168420302656

[8] Y. Hua and T.K. Sarkar, "Matrix pencil method for estimating parameters of exponentially damped/undamped sinusoids in noise," in IEEE Transactions on Acoustics, Speech, and Signal Processing, vol. 38, no. 5, pp. 814-824, May 1990, doi: 10.1109/29.56027.

[9] M. Ester, H.-P. Kriegel, J. Sander, X. Xu et al., "A density-based algorithm for discovering clusters in large spatial databases with noise." in Kdd, vol. 96, no. 34, 1996, pp. 226-231.

[10] C. Granet, "Designing classical offset Cassegrain or Gregorian dual-reflector antennas from combinations of prescribed geometric parameters," in IEEE Antennas and Propagation Magazine, vol. 44, no. 3, pp. 114-123, June 2002, doi: 10.1109/MAP.2002.1028736.

[11] G. C. Medellín, "Antenna noise temperature calculation," in SKA Memo, vol. 95, Jul. 2007.

Chapter 6

Characterising the Electric Field Ripple in Reflector Antennas Using Exponential Analysis

Characterising the Electric Field Ripple in Reflector Antennas Using Sub-Sampled Exponential Analysis

Rina-Mari Weideman
Dept of Electrical & Electronic Eng.
Stellenbosch University
Stellenbosch, South Africa
18954626@sun.ac.za

Annie Cuyt
Dept of Computer Science
University of Antwerp
Antwerp, Belgium
University of Stirling
Scotland, UK
Eindhoven University of Technology
Eindhoven, The Netherlands
annie.cuyt@uantwerpen.be

Dirk de Villiers
Dept of Electrical & Electronic Eng.
Stellenbosch University
Stellenbosch, South Africa
ddv@sun.ac.za

***Abstract*—Reflector antennas often exhibit frequency ripples in key performance metrics, including aperture efficiency and antenna noise temperature. These ripples stem from corresponding fluctuations in the electric field pattern, due to interference between fields radiated, reflected or diffracted by the feed and reflectors, and it is important that they are characterised.**

In this paper, we introduce an innovative approach for reconstructing the electric fields of reflector antennas using simulated data across a range of frequencies. By leveraging the power of sub-Nyquist sampling, the number of required samples can be reduced, leading to increased computational efficiency. This presents an advantage to traditional methods such as the Fourier transform that requires Nyquist sampling. We demonstrate how these reconstructions can be used to characterise the frequency contents of resulting reflector properties, such as aperture efficiency and antenna noise temperature.

I. Introduction

In electrically small clear aperture dual-offset reflector systems, frequency ripples can often be observed in the electric field components of their radiation pattern. These ripples stem from standing waves between the main reflector and the feed and/or sub-reflector, as well as from the interference of diffracted fields from the sub-reflector and the reflected fields from the main reflector [1], [2]. Consequently, this ripple is also present in corresponding figures of merit, such as antenna noise temperature and aperture efficiency. Characterisation of this ripple is important in several applications in wideband radio astronomy and radiometry, where the systematic response of the instrument must be accurately known in order to remove its effect from the science products [3]–[5].

The prediction is challenging due to several reasons. Firstly, multiple ripples may be present due to interfering fields with multiple characteristic lengths, which also vary with angle. Both long and short distances between the origins of interfering waves are present. Long distances translate to fast ripples, in turn requiring a dense sampling due to the Nyquist sampling criterion [2]. On the other hand, the additional presence of short distances means that the response needs to be evaluated over a large bandwidth. Since the response is wideband, the possibility of band-limited Nyquist sampling is ruled out. Dense sampling requires a large number of simulations at many frequency points, which is computationally expensive.

Validated Exponential Analysis (VEXPA) is an exponential analysis method that models a function as a sum of real and complex exponentials, while facilitating sampling at a sub-Nyquist rate. By using this method, we can therefore acquire an accurate model to predict the behaviour of the ripple with a decreased number of required frequency samples. This will in turn speed up the computation of the ripple.

In [6] we showed how VEXPA can be used to identify the frequency components from a densely-sampled antenna noise temperature function. In this paper, the VEXPA method is applied to the possibly sub-sampled electric field components to characterise its ripple. From here, an accurate model of the electric field is used to characterise the ripple in related properties of the reflector, specifically its antenna noise temperature and aperture efficiency.

II. Background

An example of an offset Gregorian dual reflector can be seen in Fig. 1, with some important parameters denoted.

A. Antenna Noise Temperature Ripple

When characterising the performance of reflector antennas, one of the primary figures of merit that is considered is the receiving sensitivity, which is a measure of the weakest signal strength that can be detected by a receiver [7]. It is described as the ratio between the effective aperture area and system noise temperature:

$$\frac{A_{\mathrm{e}}}{T_{\mathrm{sys}}} = \frac{\eta_{\mathrm{ap}} A_{\mathrm{phy}}}{T_{\mathrm{A}} + T_{\mathrm{rec}}}. \tag{1}$$

In the equation above, it is seen that the effective aperture area is equal to the product of the aperture efficiency η_{ap} and the main-reflector projected aperture area A_{phy}, while the system noise temperature T_{sys} is the sum of the antenna noise

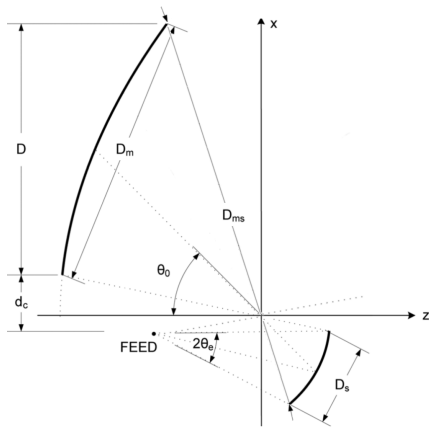

Fig. 1. An offset Gregorian dual reflector system, shown along the xz-symmetry plane. Some of the important parameters used to describe the reflector are shown.

temperature T_{A} and the receiver noise temperature T_{rec}. The antenna noise temperature is calculated as

$$T_A\left(f|\hat{\boldsymbol{r}}_0\right) = \frac{\iint_{4\pi} N\left(f,\Omega|\hat{\boldsymbol{r}}_0\right)\sin\theta d\Omega}{P_{\text{rad}}}, \tag{2}$$

where P_{rad} is the total power radiated by the antenna, and

$$N\left(f,\Omega|\hat{\boldsymbol{r}}_0\right) = T_b\left(f,\Omega\right)P\left(f,\Omega|\hat{\boldsymbol{r}}_0\right). \tag{3}$$

The product in (3) consists of the brightness temperature $T_b\left(\cdot\right)$ and the antenna radiation intensity $P\left(\cdot\right)$, with the reflector pointing in the direction $\hat{\boldsymbol{r}}_0$ and operating at frequency f. The brightness temperature $T_b\left(\cdot\right)$ is described in [8]. It incorporates various influencing elements, such as the cosmic microwave background, galactic emissions, atmospheric emissions and absorptions, as well as ground emissions and scattering [2]. The spherical coordinate system is described by $\Omega = (\theta, \phi)$, where θ is the elevation angle measured from the z-axis, which coincides with the antenna main beam, and ϕ is the azimuthal angle measured from the x-axis toward the y-axis. The resolution at which the grid is evaluated is dictated by the convergence of the integral in (2) [9].

The radiation intensity $P\left(\cdot\right)$ is given by

$$P\left(f,\Omega\right) = \frac{r^2}{2\eta}\left(\left|E_\theta\left(f,\Omega\right)\right|^2 + \left|E_\phi\left(f,\Omega\right)\right|^2\right), \tag{4}$$

where r is the radius at which the electric field components are evaluated, and η is the intrinsic impedance of free space ($\eta = 120\pi\ \Omega \approx 377\ \Omega$).

It is clear that, for a fixed direction $\hat{\boldsymbol{r}}_0$, a ripple in $E_\theta\left(f\right)$ or $E_\phi\left(f\right)$ will translate to an equivalent ripple in the behaviour of the noise temperature in (2). VEXPA is therefore used to model both $E_\theta\left(f\right)$ and $E_\phi\left(f\right)$ for each direction on the grid independently, from where an accurate representation of the noise temperature can be found using (2).

B. Aperture Efficiency Ripple

In (1), one of the factors influencing the sensitivity is the aperture efficiency η_{ap}, which is defined as the ratio of the antenna gain in a specific direction and the gain of an ideal uniformly illuminated aperture [10]. It is computed as [11]

$$\eta_{\text{ap}} = \frac{\lambda^2|E_{\text{co}}(f,0,0)|^2}{A_{\text{phy}}P_{\text{rad}}}, \tag{5}$$

where $E_{\text{co}}(f,0,0)$ is the co-polarisation component of the radiation pattern as defined by Ludwig's third definition [12]. Specifically, it is evaluated at boresight, where the radiation intensity is at a maximum, and at a frequency f with corresponding wavelength λ. The projected aperture area A_{phy} is determined by the main-reflector size.

As with the noise temperature ripple, VEXPA is used to reconstruct the field component $E_{\text{co}}(f,0,0)$, from which an accurate representation of the ripple in the aperture efficiency η_{ap} can be found using (5).

C. Sub-Nyquist Sampling

According to the Nyquist sampling limit, in order to reconstruct a sampled signal without the risk of aliasing, the sampling step needs to be smaller or equal to half of the minimum frequency rate of the signal. In the application of reflector antennas, the minimum frequency variation of the electric field is dependant on the dimensions of the reflector system, and the Nyquist sampling limit is

$$F_{S(\max)} = c/(2D_{\text{ms}}), \tag{6}$$

where c is the speed of light and D_{ms} is the maximum distance between the main- and sub-reflectors, as indicated in Fig. 1. Generally, this is a worst-case scenario limit, as most ripple components in the aperture efficiency and noise temperature will be caused by effects of shorter path lengths than this maximum.

If the aperture efficiency or antenna noise temperature is sampled instead of the electric field, the maximum sampling step is half of that in (6), since the field component frequencies are squared in (4) and (5).

VEXPA allows sampling at a rate above this limit, in turn allowing an accurate reconstruction from fewer simulated frequency points.

III. Method

A. Overview

Reflector antenna simulations are usually executed by frequency domain methods, such as the method of moments (MoM) for full-wave simulations or physical optics (PO) for asymptotic approximations. For both methods, frequency samples are more computationally expensive than angular ones. For this reason, VEXPA is used on each direction Ω independently while sub-sampling across frequency.

Consider a fixed direction Ω and the generic field component E, representing either E_θ or E_ϕ. The goal is to

approximate E as a sum of real and complex exponentials to fit the model

$$E(f) = \sum_{i=1}^{n} a_i \exp(\nu_i f), \qquad a_i, \nu_i \in \mathbb{C} \tag{7}$$

where a_i and ν_i are the complex amplitudes and frequencies in radians, respectively. The electric field E is sampled densely at frequencies $f = f_0 + m\Delta$ for $m = 0, 1, ..., M-1$, where M is the total number of samples. For now, the sampling step Δ is sufficiently small that the Nyquist sampling criterion is respected. The samples can then be represented by

$$\begin{aligned} E_m &= \sum_{i=1}^{n} a_i \exp(j\nu_i (f_0 + m\Delta)) \\ &= \sum_{i=1}^{n} a_i \exp(j\nu_i f_0) \exp(j\nu_i m\Delta), \\ & \qquad\qquad m = 0, 1, ..., M-1. \end{aligned} \tag{8}$$

Because the factor $\exp(j\nu_i f_0)$ is constant, it can be included in the coefficient:

$$E_m = \sum_{i=1}^{n} \alpha_i \exp(j\nu_i m\Delta), \tag{9}$$

with $\alpha_i = a_i \exp(j\nu_i f_0)$.

One can use VEXPA to reduce the number of samples M by means of a co-prime scale-and-shift configuration using a possible sub-Nyquist sampling step. The sampling configuration is visually portrayed in Fig. 2. The co-prime parameters σ and ρ define two subsets of samples. First, the scaled samples are defined as

$$\begin{aligned} E_{m\sigma} &= \sum_{i=1}^{n} \alpha_i \exp(j\nu_i m\sigma\Delta) \\ &= \sum_{i=1}^{n} \alpha_i (\Psi_i^{\sigma})^m, \qquad m = 0, 1, ..., M_\sigma - 1, \end{aligned} \tag{10}$$

where $\Psi_i = \exp(j\nu_i\Delta)$. Note that Δ need no longer be the true sampling step, but may be virtual, as one only truly samples at multiples of $\sigma\Delta$.

With the samples in (10), VEXPA first uses an underlying Prony-based exponential analysis method that computes the base terms $\Psi_i^{\sigma} = \exp(j\nu_i\sigma\Delta)$. In general, Prony-based methods can construct models of up to $n = \lfloor M_\sigma/2 \rfloor$ terms, where M_σ is the number of samples in the scaled subset. Subsequently, the coefficients α_i for $i = 1, ..., n$ are determined by solving the Vandermonde linear set of equations in (10).

Since the sampling step $\sigma\Delta$ may now be larger than the Nyquist sampling limit, the frequencies ν_i can no longer be recovered unambiguously from the base terms Ψ_i^{σ} [13].

Second, a subset of samples is created to mitigate this problem. This subset makes up the so-called shifted samples, defined as

$$\begin{aligned} E_{m\sigma+\rho} &= \sum_{i=1}^{n} \alpha_i \exp(j\nu_i (m\sigma + \rho)\Delta) \\ &= \sum_{i=1}^{n} (\alpha_i \Psi_i^{\rho})(\Psi_i^{\sigma})^m \qquad m = 0, 1, ..., M_\rho - 1. \end{aligned} \tag{11}$$

As with the scaled subset, this set of equations is solved to find the coefficients $\alpha_i\Psi_i^{\rho}$. Since the coefficients α_i have already been computed by using (10), the shifted base terms are found as the quotients $(\alpha_i\Psi_i^{\rho})/\alpha_i$ for $i = 1, ..., n$.

From the M_σ samples in the scaled subset, $2n$ parameters are found, i.e., the n base terms Ψ_i^{σ}, and the n coefficients α_i. Since only n parameters are obtained from the shifted subset, the number of samples in this subset need only be half of that of the scaled subset. Here it should be noted that n is unknown and requires an estimation technique, which is described in an upcoming section.

The goal is to interpolate the field values over a specific frequency range, and therefore we want to distribute the used samples evenly to achieve an adequate coverage of this range. Since the number of samples in the shifted subset is only half that of the scaled subset, a shifted sample is placed after every second scaled sample. Essentially, this means that the indices $m = 0, 1, ..., M_\rho - 1$ in (11) are changed to $m = 0, 2, ..., 2(M_\rho - 1)$. The sample configuration is visually described in Fig. 2.

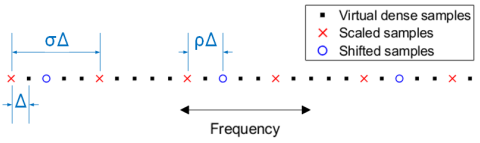

Fig. 2. Placement of the sampling points for the co-prime scale-and-shift sparse configuration. For this case, the parameters are $\sigma = 5$, $\rho = 2$, $M_\sigma = 6$ and $M_\rho = 3$. Note that a shifted sample is placed only after every second scaled sample.

Now that both the scaled and shifted base terms are known, the de-aliasing method presented in [13] is used to compute the base terms $\Psi_i = \exp(j\nu_i\Delta)$ from the aliased base terms and the co-prime parameters σ and ρ.

Finally, the electric field values are computed at the frequencies of interest by using the continuous exponential model, after which an accurate representation of the antenna noise temperature or aperture efficiency can be found.

B. Underlying Method

The first step while using VEXPA in a new application is to decide which underlying Prony-method is used to compute the scaled base terms Ψ_i^{σ}. In this case, methods using the covariance matrix are immediately discarded, since an accurate

estimation of the covariance matrix requires many temporal samples. As the electric field components are independent of time, we only have one snapshot or time sample with which to work. Therefore methods such as MUSIC and Root-MUSIC are unfitting. The Matrix Pencil method [14] seems to be the ideal underlying method to use in this application. In short, the MP method constructs Hankel matrices from the received signals, after which it uses the singular value decomposition (SVD) to obtain the signal and noise subspaces. The base terms Ψ_i^σ then equal the generalised eigenvalues of the signal subspace.

C. Choosing the Number of Terms

As with most subspace-based methods, the MP method usually estimates the number of exponential terms n by exploiting the structure of the SVD. When dealing with a sum of n exponentials, there will be n singular values that are significantly larger than the others, signifying the signal subspace. Using this information, we can estimate the number of terms by counting the number of singular values that are larger than a certain threshold, i.e., those for which

$$\sigma_i/\sigma_{\max} \; > \; 10^{-p} \; (i \; = \; 1, ..., N) \tag{12}$$

is true. Here, N is an overestimation of the number of terms. The maximum number of terms that can be returned by the MP method is $\lfloor M_\sigma/2 \rfloor$ and therefore N is often set to this value. The threshold value p can be chosen by considering noise levels.

In many applications, this is a very accurate method to estimate n. However, since we do not have exact exponential signals at hand but rather want to approximate these signals by using exponentials, there is not such a clear distinction between the singular values corresponding to the signal subspace and those of the noise subspace. This can be seen in Fig. 3. Here, the ratio of the singular values to the largest singular value is shown. The red line indicates the singular values when using the sparsely sampled data of the E_θ component for a particular reflector and direction. The black line indicates the same, but when using data from a synthetic exponential signal containing four terms. Specifically, the exponential signal is the one found from an accurate reconstruction of the real data. For the black line, there is a clear drop in the ratios between singular value $\sigma_i \; = \; 4$ and $\sigma_i \; = \; 5$. The number of terms can therefore be confidently estimated as $n = 4$. On the other hand, for the red line, the decline in ratio values is much more gradual, making the distinction between the signal and noise subspace more vague. Still, this singular value approach is a good starting point to get a rough idea of the number of terms needed to reconstruct the signals. If, for example, p is set equal to 3 in (12), this would result in a first estimate of $n \; = \; 6$ for the real data of Fig. 3.

After this first estimate is made, the rest of the algorithm proceeds. Once the reconstruction of E is completed, an evaluation is performed to see if enough exponential terms have been used to accurately interpolate the signal. This is done by comparing the estimates $|\hat{E}|^2$ to the true values of $|E|^2$ at the

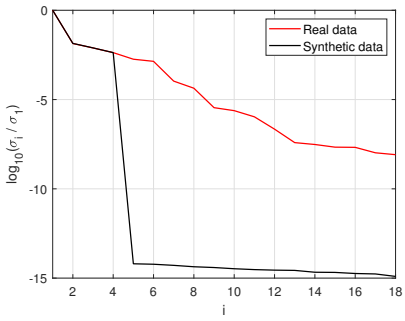

Fig. 3. The ratios of the 18 singular values to the largest singular value. The black line shows the ratios for the singular values when using a synthetic exponential signal with $n = 4$ terms. The red line shows those when using the electric field data.

sampled points. These are sampled at the frequencies defined as $f_{m\sigma} \; := \; f_0 \; + \; m\sigma\Delta$ for $m \; = \; 0, 1, ..., M_\sigma - 1$ and $f_{m\sigma+\rho} \; := \; f_0 \; + \; (m\sigma + \rho)\,\Delta$ for $m \; = \; 0, 2, ..., 2(M_\rho - 1)$. The estimates $|\hat{E}|^2$ are computed by using the computed coefficients and base terms in the continuous model (7) at the respective frequencies, and subsequently squaring the modulus of these values. Note that the squared values are compared rather than the absolute values, since these are the ones used in the reconstruction in (4) and (5). If the approximated values are close enough to the true ones, the number of exponential terms is regarded as adequate to reconstruct the signals accurately.

To set a criterion for determining if the approximation is satisfactory, the relative error is used. However, for some of the interpolation points the magnitude of the sample is inherently small. For these cases, the relative error would misleadingly appear to be very large. The absolute error is therefore rather used for these samples. To summarize, the error is calculated as

$$\epsilon(f) = \frac{||E(f)|^2 - |\hat{E}(f)|^2|}{|E(f)|^2} \tag{13}$$

if

$$|\hat{E}(f)|^2 \geq \frac{\max(|\hat{E}_{m\sigma}|^2 \cup |\hat{E}_{m\sigma+\rho}|^2)}{1000} \tag{14}$$

and else,

$$\epsilon(f) = ||E(f)|^2 - |\hat{E}(f)|^2|. \tag{15}$$

Furthermore, two different domains are defined, namely the centre and the edges. The set of centre frequencies is defined in (19). The remaining frequencies are classified as the edge frequencies. Because the interpolation will evidently be less accurate towards the ends of the interpolation range, different tests are used for these two domains, with the one for the edge frequencies being less stringent.

An approximation is seen as acceptable if

$$\max(\epsilon(f)) < \gamma, \tag{16}$$

where γ is a threshold value, defined as $\gamma_e = 2 \times 10^{-2}$ and $\gamma_c = 1 \times 10^{-2}$ for the edge and centre cases, respectively. Thus, the error ϵ is also defined separately for the edge and centre cases as

$$\epsilon_e = \max\{\epsilon(f) : (f = f_{m\sigma} \text{ or } f = f_{m\sigma+\rho}) \text{ and } f \notin C\}, \tag{17}$$

and

$$\epsilon_e = \max\{\epsilon(f) : (f = f_{m\sigma} \text{ or } f = f_{m\sigma+\rho}) \text{ and } f \in C\}, \tag{18}$$

where

$$C = \{f : f_0 + 0.1(M_\sigma - 1)\sigma\Delta \leq f \leq f_0 + 0.9(M_\sigma - 1)\sigma\Delta\}. \tag{19}$$

If this test fails, an iterative process is started: the estimated number of terms is incremented by 1, and the reconstruction procedure recommences. This is repeated until either the approximation is close enough to the true signal, or the maximum number of terms that can be used, i.e. $\lfloor M_\sigma/2 \rfloor$, has been reached. If the latter case occurs, the final estimated number of terms is set to the value of n for which the error ϵ is the smallest.

An example is shown in Fig. 4. As a first guess using the singular values, the method estimates n to be 4. The succeeding reconstruction of $|E_\theta|^2$ is shown in the top graph. The errors at the sampled points (indicated by the blue and green dots) are investigated and found to be too large for a confident reconstruction. The iterative process starts by incrementing n to $n = 5$. This process continues until the error at the sampled points is sufficiently small, which happens at $n = 9$ for this case, and is shown in the bottom graph.

Since the maximum number of terms is directly proportional to the number of samples available, there is a trade-off that occurs when deciding on the number of samples to use: if a small number of samples is chosen to reduce computation time, it might be that not enough terms are available to create an accurate reconstruction. However, a number of samples corresponding to a sampling rate significantly below the Nyquist limit should still be sufficient, as will be shown in the Results section. An attractive feature that is left as future work will be to find a procedure to determine the number of samples required for an accurate reconstruction automatically.

D. Filtering High Frequency Terms

A physical limitation exists on the rate of variation of the electric field over frequency in reflector antennas. This limitation is determined by the maximum distance as

$$\nu_{max} = \frac{2\pi D_{\text{ms}}}{c}, \tag{20}$$

where c is the speed of light. This means that terms returned by VEXPA with frequencies that are higher than this value should be discarded. In the case that one or more terms are discarded for this reason, new coefficients α_i are computed for the remaining exponential terms.

A summary of the algorithm is given in Algorithm 1.

Algorithm 1 Electric field reconstruction using VEXPA

Input: Field data $E_\theta(f, \Omega)$ and $E_\phi(f, \Omega)$, sampled at one or multiple directions Ω on discrete sphere S and at frequencies $f_{m\sigma} = f_0 + m\sigma\Delta$ for $m = 0, 1, ..., M_\sigma - 1$ and at frequencies $f_{m\sigma+\rho} = f_0 + (m\sigma + \rho)\Delta$ for $m = 0, 2, ..., 2(M_\rho - 1)$.

Output: Continuous model for $\hat{E}_\theta(f)$ and $\hat{E}_\phi(f)$ with n complex coefficients and frequencies, as in (7).

1: Set edge and centre error thresholds $\gamma_e = 2 \times 10^{-2}$ and $\gamma_c = 1 \times 10^{-2}$.
2: Set $n_{\text{max}} = \lfloor M_\sigma/2 \rfloor$.
3: **for** each direction Ω in S **do**
4: **if** $|E_\theta| \ll |E_\phi|$ for collected samples **then**
5: Set $\hat{E}_\theta$ equal to the mean of the samples for all interpolation frequencies.
6: **else**
7: Get a first estimate of the number of terms n by using the SVD and the threshold $p = 6$, defined in (12).
8: **repeat**
9: Use the Matrix Pencil method to compute the base terms $\Psi_i^\sigma = \exp(j\nu_i\sigma\Delta)$ for $i = 1, ..., n$.
10: Compute the coefficients α_i for $i = 1, ..., n$ by using the Vandermonde linear system in (10).
11: Compute the base terms $\Psi_i^\rho = \exp(j\nu_i\rho\Delta)$ for $i = 1, ..., n$ by using the Vandermonde linear system in (11).
12: Compute the de-aliased base terms $\Psi_i = \exp(j\nu_i\Delta)$ by finding the intersections of the sets $(\Psi_i^\sigma)^{\frac{1}{\sigma}}$ and $(\Psi_i^\rho)^{\frac{1}{\rho}}$ for $i = 1, ..., n$.
13: Compute frequency information $\nu_i = \frac{-j\log(\Psi)}{\Delta}$ for $i = 1, ..., n$.
14: **if** $\nu_i > \nu_{\text{max}}$ as defined in (20) for any i **then**
15: Repeat step 10 with high frequency terms discarded.
16: **end if**
17: Reconstruct E_θ as follows: $\hat{E}_\theta = \sum_{i=1}^{n} \alpha_i \exp(j\nu_i m\Delta)$ at desired interpolation points $m = 0, 1, ..., M - 1$.
18: Compare E_θ and $\hat{E}_\theta$ at the sampled points and find the error ϵ_e (defined in (18)) and ϵ_c (defined in (17)) for the edge and centre frequencies, respectively.
19: $n \leftarrow n + 1$
20: **until** ($\epsilon_e < \gamma_e$ and $\epsilon_c < \gamma_c$) or $n = n_{\text{max}}$
21: **if** $n = n_{\text{max}}$ **then**
22: Find n that minimises ϵ_e and ϵ_c.
23: Execute steps 9 to 17 with n set to the value found in step 22.
24: **end if**
25: **end if**
26: **if** $|E_\phi| \ll |E_\theta|$ for collected samples **then**
27: Set $\hat{E}_\phi$ equal to the mean of the samples for all interpolation frequencies.
28: **else**
29: Execute steps 7 to 24 for E_ϕ.
30: **end if**
31: **end for**

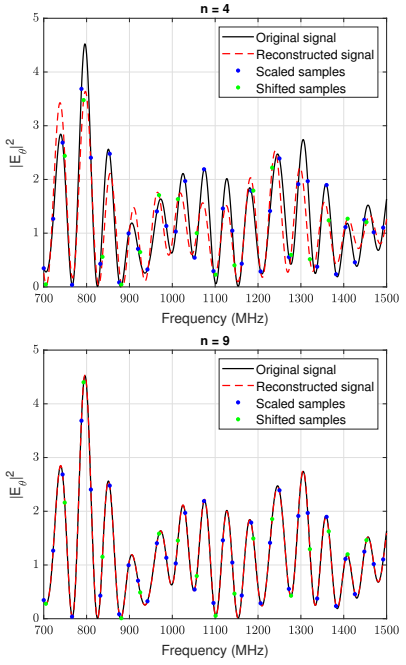

Fig. 4. At its first iteration, the method initially estimates $n = 4$, for which the reconstruction is shown in the top graph. An accurate reconstruction is achieved at $n = 9$, for which the reconstruction is shown in the bottom graph.

TABLE I
REFLECTOR DIMENSIONS: APERTURE EFFICIENCY EXAMPLE

D	D_{ms}	D_{m}	D_{s}	d_{c}	θ_{e}
13.5 m	16.8 m	15.7 m	4.2 m	0.5 m	48.9 deg

IV. EXPERIMENTAL SETUP

A. Aperture Efficiency

As an example, consider the offset dual reflector system as portrayed in Fig. 1. The dimensions are summarised in Table I. The antenna feed is a -10 dB edge taper Gaussian pattern feed polarised in the symmetry plane.

The reflector system is simulated using physical optics (PO) including physical theory of diffraction (PTD) methods with the software GRASP [15]. The interaction between the feed and reflector is ignored for this illustration, but can be added when using the method of moments (MoM) as simulation method. A full simulation is performed at 251 frequency points in the simulation bandwidth 500 MHz - 1000 MHz, translating to a sampling step of $\Delta = 2$ MHz. This provides us with a densely-sampled function that can later be used as validation data.

TABLE II
VEXPA PARAMETERS: APERTURE EFFICIENCY EXAMPLE

σ	ρ	M_σ	M_ρ
21	11	12	6

TABLE III
REFLECTOR DIMENSIONS: NOISE TEMPERATURE EXAMPLE

D	D_{ms}	D_{m}	D_{s}	d_{c}	θ_{e}
6 m	8.7 m	7.5 m	2 m	1 m	45 deg

Since the aperture efficiency calculation only uses the co-polarisation electric field evaluated at a single direction, VEXPA only needs to be applied to this direction ($\theta = 0°$, $\phi = 0°$). The parameters used by VEXPA is summarised in Table. II. The total number of samples is equal to $M_\sigma + M_\rho = 18$.

Using (6), the maximum Nyquist sampling limit is calculated to be $F_{S\max} = 8.9$ MHz. The maximum sub-sampled sampling step used by VEXPA is $F_S = \sigma\Delta = 42$ MHz. This is clearly well above the Nyquist limit, which emphasises the advantage of using VEXPA. From a different perspective, if the Nyquist sampling step was used instead of sub-sampling, a total of at least 58 samples would have to be used, which is significantly more than the 18 used by VEXPA. The results are shown in Fig. 5 and are discussed in an upcoming section.

B. Antenna Noise Temperature

A reflector system with parameters as in Table III and a Gaussian pattern with -10 dB edge taper is simulated. The tipping angle of the reflector is $\theta_p = 0°$. The simulation is performed at 801 frequency points in the range 700 MHz - 1500 MHz, sampled at a sampling step of $\Delta = 1$ MHz. These densely-sampled data are used as a validation set. In order to evaluate the integral in the numerator of (2), the field components are sampled on a spherical grid at a resolution of $1°$ for elevation angle θ and $2°$ for azimuthal angle ϕ. This totals to 32,761 directions, each requiring a reconstruction using VEXPA.

The parameters used by VEXPA are tabulated in Table IV. A total of $M_\sigma + M_\rho = 55$ samples are used. According to (6), the maximum sampling step that can be used to avoid aliasing is 17.2 MHz, but since the noise temperature ripple consists of contributing factors from ripples in all the electric fields on the grid, classical Fourier methods would need to be used on the noise temperature data rather than the electric field data. This would imply a sampling limit of $17.2/2 = 8.6$ MHz, or a total of 95 samples. By using 55 samples and a maximum sampling step of $F_S = \sigma\Delta = 22$ MHz, VEXPA introduces the advantage of fewer simulated frequency points through the use of sub-sampling. The results are shown in Fig. 8 and are discussed in an upcoming section.

TABLE IV
VEXPA PARAMETERS: NOISE TEMPERATURE EXAMPLE

σ	ρ	M_σ	M_ρ
22	5	37	18

V. RESULTS

A. Aperture Efficiency

The resulting reconstructed co-polarised electric field component is shown in Fig. 5. The solid black line portrays the full GRASP simulation at 251 frequency points, whereas the red dashed line portrays the reconstructed function as determined by VEXPA. The scaled and shifted samples as defined in (10) and (11) are displayed as blue and green markers, respectively. The reconstructed function clearly follows the original one closely, meaning that an accurate model was determined by VEXPA. Subsequently, the aperture efficiency is calculated from both the original and reconstructed field component, using (5), and compared in Fig. 6. In the top graph, the original and reconstructed function are portrayed, where it can be seen once again that the latter follows the former. Specifically, the shape of the frequency ripple is accurately captured by the reconstructed version. The percent error is shown in the bottom graph. The mean percent error is 0.024 %, whereas the maximum percent error is 0.17 %. It is clear that VEXPA is capable of characterising the ripple in the aperture efficiency.

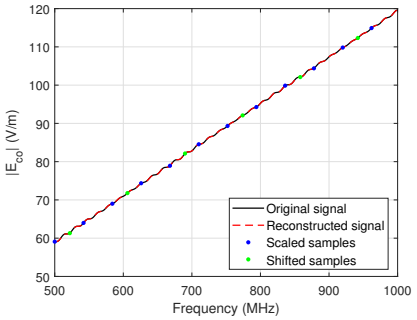

Fig. 5. The reconstruction of the co-polarised electric field component in the direction of the main beam, using VEXPA. The function from the full GRASP simulation is indicated by the black solid line, whereas the reconstructed function is indicated by the dashed red line. A total of 18 samples are used by VEXPA, which are indicated by the blue and green markers.

Next, the VEXPA-based method described in [6] is used to extract the frequency components from the reconstructed ripple. The method is used with one slight change: in [6] n is determined by use of cluster analysis, whereas we now use the same iterative method described in a previous section of this paper. The results are shown in Fig. 7. The horizontal axis displays the oscillation period. A peak located at a smaller period implies a faster varying ripple component [6]. Along

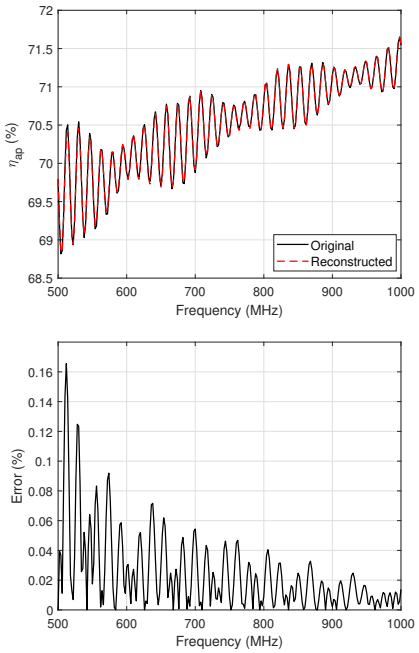

Fig. 6. The resulting aperture efficiency reconstructed by using the reconstructed co-polarised electric field component. In the top graph, the function from the full GRASP simulation is indicated by the black solid line, whereas the reconstructed function is indicated by the dashed red line. The bottom graph shows the percentage error of the efficiency reconstruction.

with the peaks determined by VEXPA, which are indicated by the purple stems, a Fourier spectrum is shown. The stems are normalised to the value of the maximum peak. An FFT is performed on the full simulation aperture efficiency function that has been detrended, which means that a trend line is subtracted from the original function. The FFT spectrum corroborates the results of VEXPA with some peaks not identified by VEXPA. Since VEXPA accurately reconstructs the function accurately without these components, as seen in Fig. 6, it can be concluded that these are superfluous peaks. It was also seen in [6] that the detrending of the data tends to introduce artificial ripple components. In a practical sense, VEXPA has the advantage that there is no need to preprocess the data through detrending, as well as the fact that no peak-picking technique is required, since actual components are returned rather than a spectrum [6].

B. Antenna Noise Temperature

VEXPA is used to find reconstructions for the electric field components of all directions on the specified integration grid, after which (2) is used to find a reconstructed noise

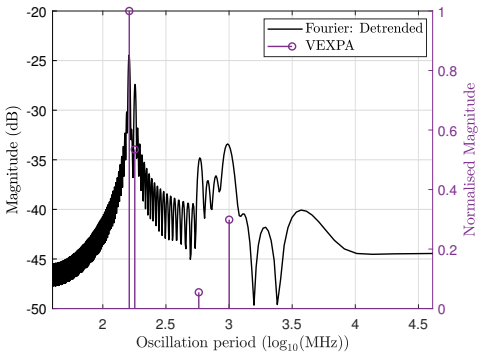

Fig. 7. Frequency contents delivered by VEXPA and the Fourier transform using the reconstructed aperture efficiency and full simulation, respectively. The results of both methods are in agreement, but VEXPA is the preferred method as no preprocessing of the data or peak-picking technique are required.

temperature. The resulting reconstruction can be seen in the top graph of Fig. 8, with the percent error in the bottom graph. The maximum and mean percent error are 0.18 % and 0.068 %, respectively, with the reconstructed function following the original closely. In Fig. 9, VEXPA is again used to identify the frequency components of the reconstructed noise temperature, which are indicated by purple stems. The Fourier spectrum of the noise temperature of the full simulation is presented in black. VEXPA accurately finds the correct frequency components, which is seen by the peaks of the spectrum aligning with the positions of the purple stems. Once again, there are some superfluous peaks in the Fourier transform.

VI. Conclusion

In this paper, we present a method to reconstruct electric field patterns of reflector antennas from sub-sampled data using exponential analysis. By sampling at a sub-Nyquist rate, the number of simulations can be reduced, which saves computational time. From the reconstructed electric fields, accurate representations of reflector properties such as the aperture efficiency and antenna noise temperature can be found, as well as its frequency contents.

Future work includes developing a technique to determine the number of required samples or sub-Nyquist sampling rate automatically.

Acknowledgment

This research has received funding from the European Union's Horizon 2020 research and innovation programme under the Marie Skłodowska-Curie grant agreement No 101008231 (EXPOWER). It is also based on research supported in part by the National Research Foundation of South Africa (Grant Number 75322).

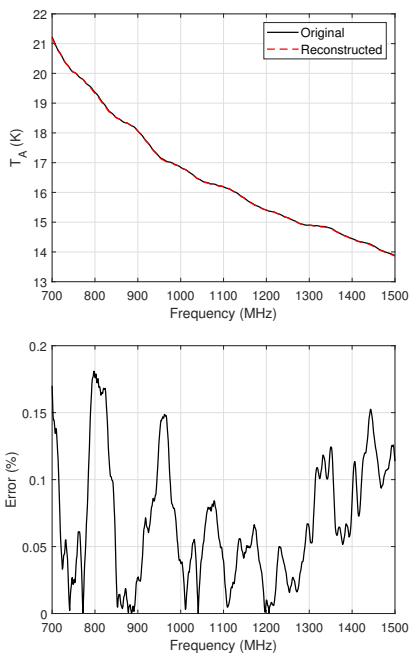

Fig. 8. The resulting antenna noise temperature obtained from the reconstructed electric field components on a grid. In the top graph, the function from the full GRASP simulation is indicated by the black solid line, whereas the reconstructed function is indicated by the dashed red line. The bottom graph shows the percentage error of the noise temperature reconstruction.

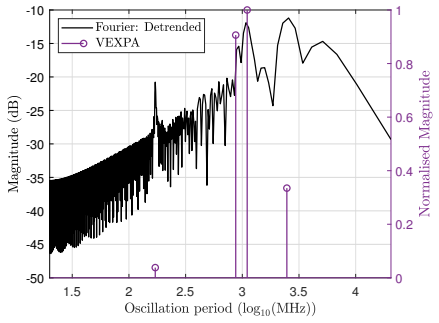

Fig. 9. Frequency contents delivered by VEXPA and the Fourier transform using the reconstructed antenna noise temperature and full simulation, respectively. The results of both methods are in agreement, but VEXPA is the preferred method as no preprocessing of the data or peak-picking technique are required.

REFERENCES

[1] D.I.L. de Villiers, "Prediction of Aperture Efficiency Ripple in Clear Aperture Offset Gregorian Antennas," in *IEEE Transactions on Antennas and Propagation*, vol. 61, no. 5, pp. 2457-2465, May 2013, doi: 10.1109/TAP.2013.2239953.

[2] W.J. Cerfonteyn, F.T.T. Mokhupuki and D.I.L. de Villiers, "Receiving Sensitivity Ripple in Electrically Small Offset Gregorian Reflector Antennas". *TechRxiv*, 18-Oct-2023, doi: 10.36227/techrxiv.24324838.v1.

[3] R. Padman, "Reduction of the baseline ripple on spectra recorded with the Parkes radio telescope," *Proceedings of the Astronomical Society of Australia*, vol. 3, pp. 111–113, Aug. 1977.

[4] D. Morris, "Chromatism in radio telescopes due to blocking and feed scattering," *Astronomy & Astrophysics*, vol. 67, pp. 221 – 228, 1978.

[5] P.F. Goldsmith and N.Z. Scoville, "Reduction of baseline ripple in millimeter radio spectra by quasi-optical phase modulation," *Astronomy & Astrophysics*, vol. 82, pp. 337–339, 1980.

[6] R. Weideman, A. Cuyt and D.I.L. De Villiers, "Characterising the Frequency Ripple in Antenna Noise Temperature Using Exponential Analysis," *International Conference on Electromagnetics in Advanced Applications (ICEAA)*, Venice, Italy, 2023, in press.

[7] D.I.L. de Villiers and R. Lehmensiek, "Rapid Calculation of Antenna Noise Temperature in Offset Gregorian Reflector Systems," in *IEEE Transactions on Antennas and Propagation*, vol. 63, no. 4, pp. 1564-1571, April 2015, doi: 10.1109/TAP.2015.2399933.

[8] G.C. Medellin, "Antenna noise temperature calculations," in *SKA Memo 95*, July 2007. [Online]. Available: https://cornell.academia.edu/GermanCortes

[9] W.J. Cerfonteyn, F.T.T. Mokhupuki and D.I.L. de Villiers, "Frequency Ripple in Antenna Noise Temperature of Small Offset Gregorian Reflector Systems," *International Conference on Electromagnetics in Advanced Applications (ICEAA)*, Cape Town, South Africa, 2022, pp. 207-211, doi: 10.1109/ICEAA49419.2022.9900010.

[10] Volakis, John Leonidas. *Antenna Engineering Handbook*. 4th ed. New York: McGraw-Hill, 2007.

[11] J. Yang, "Calculation of aperture efficiency of reflector antenna with the measured far-field function of its feed in Ludwig's third definition," in *15th European Conference on Antennas and Propagation (EuCAP)*, Dusseldorf, Germany, 2021, pp. 1–4.

[12] A. Ludwig, "The definition of cross polarization," *IEEE Transactions on Antennas and Propagation*, vol. 21, no. 1, pp. 116–119, 1973.

[13] M. Briani, A. Cuyt, F. Knaepkens, and W.-S Lee, "VEXPA: Validated EXPonential Analysis through regular sub-sampling," *Signal Processing*, vol. 177, p. 107722, 2020. [Online]. Available: https://www.sciencedirect.com/science/article/pii/S0165168420302656

[14] Y. Hua and T.K. Sarkar, "Matrix pencil method for estimating parameters of exponentially damped/undamped sinusoids in noise," in *IEEE Transactions on Acoustics, Speech, and Signal Processing*, vol. 38, no. 5, pp. 814-824, May 1990, doi: 10.1109/29.56027.

[15] TICRA Tools, GRASP, Version 23.0, Copenhagen, Denmark. [Online]. Available: http://www.ticra.com